COHERENT INTERACTIONS BETWEEN WHISTLER MODE WAVES AND
ENERGETIC ELECTRONS IN THE EARTH'S RADIATION BELTS

A DISSERTATION
SUBMITTED TO THE DEPARTMENT OF ELECTRICAL ENGINEERING
AND THE COMMITTEE ON GRADUATE STUDIES
OF STANFORD UNIVERSITY
IN PARTIAL FULFILLMENT OF THE REQUIREMENTS
FOR THE DEGREE OF
DOCTOR OF PHILOSOPHY

Vijay Harid
April 2015

I certify that I have read this dissertation and that, in my opinion, it is fully adequate in scope and quality as a dissertation for the degree of Doctor of Philosophy.

_____

(Umran. S. Inan)   Principal Adviser

I certify that I have read this dissertation and that, in my opinion, it is fully adequate in scope and quality as a dissertation for the degree of Doctor of Philosophy.

_____

(Marek Golkowski)

I certify that I have read this dissertation and that, in my opinion, it is fully adequate in scope and quality as a dissertation for the degree of Doctor of Philosophy.

_____

(Sigrid Close)

Approved for the Stanford University Committee on Graduate Studies

_____

iii

Abstract

Near-Earth space can be best described as a large electromagnetic system dominated by fundamental plasma physical interactions. Specifically, high energy electrons and protons sourced from the solar wind are trapped in the Earth's magnetic field and form the radiation belts. The interaction between energetic particles in the Earth's radiation belts and electromagnetic waves plays an important role in the dynamics of the near-Earth space environment. In this work, we can consider the nonlinear gyro-resonant (doppler shifted cyclotron resonant) interaction between "whistler-mode" electromagnetic waves and energetic electrons in the radiation belts. Specifically, we address the amplification of whistler mode waves externally injected into the radiation belts as well as the subsequent precipitation of energetic electrons interacting with such waves.

Modeling wave amplification due to gyro-resonant wave-particle interactions in the radiation belts requires the solution of the Vlasov-Maxwell system of equations in an inhomogeneous magneto-plasma. Previous works have employed Particle-In-Cell (PIC) methods or Eulerian solvers (such as the VHS code) to provide numerical solutions of this problem. In this report, we provide an alternative numerical approach by utilizing a first order finite difference upwind scheme. When coupled with the narrowband Maxwell's Equations, the model reproduces linear as well as nonlinear wave growth of coherent signals. Wave growth is nonlinear when the wave amplitude exceeds the minimum value for phase trapping of counter streaming resonant particles and is linear otherwise. The model also demonstrates free-running frequency variation for a case with a high linear growth rate. In addition, the model confirms the theoretical prediction of a stable "phase space hole" during the nonlinear growth process with higher resolution than that which was obtained in previously attempted simulations.

The interaction between coherent whistler mode waves and energetic radiation belt electrons can also result in pitch angle scattering of electrons into the bounce loss cone and their subsequent precipitation onto the natural atmosphere. In order to capture the nonlinear effects of large amplitude coherent waves, we utilize a Vlasov-Liouville (VL) model which computes the precipitated phase-space particle distribution function directly using a characteristic based solution of the Vlasov equation. Previous work has shown that in the case of large amplitude coherent waves, phase-trapping can significantly perturb resonant particles from their adiabatic paths. We evaluate the

importance of phase-trapping over a range of wave amplitudes (up to 200 pT); the percentage of particles that precipitate after being phase trapped is computed over a phase space grid in the loss cone. The results demonstrate that phase trapping contributes significantly to precipitation when a large amplitude wave (> 100 pT) is present. Additionally, linear theory can be valid over a broad range of amplitudes and the relative accuracy of linear theory in calculating the precipitated flux depends strongly on the initial particle distribution. We also demonstrate the ability of the VL model to calculate the time evolution of the precipitated flux due to short duration whistler mode pulses.

The physical parameters used in the modeling effort presented here are typical of those associated with the Siple Station wave injection experiment, carried out over a 15 year period (1973−1988), using a dedicated and specifically designed VLF transmitter located over the thick Antarctic ice sheet.

Acknowledgments

There are several individuals without whom this dissertation would not have been possible. First and foremost, I would like to thank my adviser, Professor Umran Inan for his support (both professionally and personally) and unmatched intuition for the physical sciences. Being part of Professor Inan's Very Low Frequency (VLF) group legacy is an opportunity not afforded to many, and I am forever grateful to have been able to work on one of the most fascinating physics problems I have ever encountered. Second, I would like to extend my deepest gratitude to Professor Marek Golkowski at UC Denver for being an exemplary academic mentor for me. The discussions we have had over the past six years have had an immeasurable impact on my understanding of space plasmas and have molded me into the scientist I am today. Third, I would like to thank Dr. Timothy Bell whose profound scientific insight has unquestionably shaped the collection of my work into a cohesive PhD thesis. I would also like to thank Dr. Maria Spasojevic for her support and guidance over the course of my degree. Without Maria, I would never have been introduced to the VLF group and would have not been exposed to this most intriguing branch of scientific inquiry. I am also very grateful for the many interactions I have had with Professor Don Carpenter, especially for the valuable historical context behind the work in this dissertation. I am also very thankful for Professor Morris Cohen for providing me the opportunity to have been part of the AWESOME team where I have gained invaluable exposure to the "political" side of the scientific community.

The fact that I have truly enjoyed the past six years in the VLF group and is largely because of my student colleagues. I owe thanks to Justin Li, Patrick Blaes, Rasoul Kabirzadeh, Fadi Zoghzoghy, Chris Young, Austin Sousa, Can Liang, Kevin Graf, Naoshin Haque, Forrest Foust, Dan Golden, and George Gin for making my experience at Stanford truly memorable. I also extend my gratitude to Shaolan Min and Helen Niu for taking all the administrative work out of my hands and making my life significantly easier.

Finally, and most importantly, I would like to thank my parents, Sudha and Shankar, and my fiancée, Erica, for their unwavering moral support. I can unquestionably say that I would not have succeeded this far in my academic career without your loving weight behind me.

Contents

List of Tables

List of Figures

Chapter 1

Introduction

The near-Earth space environment is home to a variety of complex plasma physics phenomena that has been studied extensively over the past century. Although much of the large scale dynamics of space weather are well understood, there still remains many unanswered physics questions that are subjects of current experimental and theoretical research. The focus of this dissertation is on the interactions between coherent Very Low Frequency ($3-30$ kHz) electromagnetic waves and energetic electrons in the Earth's Radiation Belts. Specifically, we address two aspects of these wave-particle interactions: wave amplification and electron precipitation. Both these phenomena play significant roles in the energetics and loss processes of the near-Earth space environment and advancing our understanding is thus crucial for a comprehensive and quantitative understanding of space weather. In this section, we provide the relevant background and motivation for the problem being studied by describing the Earth's Magnetosphere, and then present the primary scientific contributions of this dissertation.

1.1   The Magnetosphere

The magnetosphere is defined as the region of near-Earth space where physical processes are heavily influenced by the Earth's geomagnetic field. For the region up to approximately $5R_{\mathrm{E}}$ (Earth's Radius $= 1R_{\mathrm{E}} \simeq 6370$ km) from the center of the Earth, the geomagnetic field resembles a simple magnetic dipole, akin to that of a giant bar magnet. However, due to the impact of the solar wind, the shape of the geomagnetic field becomes compressed ahead of the Earth and at larger distances, causes 'tail' of the magnetosphere behind the Earth to extend out to $10-12$ R_{E}. The region of space where the geomagnetic field is approximately dipolar ($< 5R_{\mathrm{E}}$) is referred to as the "Inner Magnetosphere" and is the focus of this work.

In addition to the magnetic field, the magnetosphere is also comprised of various kinds of plasma. A plasma can simply be described as an "electronic gas", a gas that is hot enough such that the

electrons and ions of atoms no longer bond to their nuclei and can interact which each other through long range electromagnetic forces. More specifically, a plasma is an ionized gas that is quasi-neutral and exhibits collective behavior. The plasma in the magnetosphere can be classified into two distinct populations: the "cold" plasma and the "hot" plasma.

Most of the plasma falls under the cold category consisting of particles of relatively low energy $\sim$ 0.5 eV (5000° K) and densities in the range of $10-1000$ el/cm^3 [17]. One characteristic of this cold plasma distribution is a sudden drop-off in the electron density by a few orders of magnitude at a boundary known as the plasmapause [15]; the region of the magnetosphere inside the plasmapause is referred to as the plasmasphere. This plasmapause boundary is believed to be determined by the competition between the co-rotating electric field (induced by the Earth's rotation in its geomagnetic field) and cross-tail electric field driven by the solar wind. Typical locations of the plasmapause are between $2R_\mathrm{E}$ and $7R_\mathrm{E}$.

The second, hot plasma population, consists of much higher energy particles 100 keV-10 MeV but is relativity sparse with densities of less than 1 el/cm^3. These energetic particles gyrate around the Earth's magnetic field as they travel along the field lines as expected for an electron in a static magnetic field. However, due to the spatial variation of the geomagnetic field, the rate of electron gyration increases as it travels along the field lines towards regions of higher geomagnetic fields (i.e., closer to the planet) while the component of the particle velocity parallel to the geomagnetic field reduces. Eventually, this parallel velocity diminishes to zero and changes sign, causing the electron to "mirror" back to the hemisphere that it came from. Due to this constant back-and-forth mirroring in each hemisphere, the particles are confined in a magnetic trap and comprise what are known as the Earth's radiation belts [96].

In addition to the cold and hot plasma, the magnetosphere also supports the propagation of a large variety of electromagnetic waves. Specifically, the cold plasma essentially acts like a linear background material (quantified by an electric permitivity tensor) that governs the types of wave modes which can propagate in the system. The hot plasma, on the other hand, drives more complex phenomena such as wave amplification and the production of new waves via nonlinear interactions constituting the subject of active ongoing research [82, 96, 12, 93, 13, 54, 83, 64].

Of particular interest is the interaction of energetic electrons with so-called "whistler mode" waves. Such waves have been studied extensively over the past 50 years and are believed to be responsible for a variety of phenomenon including the production of naturally occurring waves known as "chorus" and the amplification of injected VLF signals from terrestrial sources. Whistler mode waves are circularly polarized electromagnetic signals that propagate in a magnetized plasma with frequencies below the electron cyclotron frequency but above the proton cyclotron frequency. A more rigorous mathematical description of the wave mode and the interaction process are discussed in later chapters.

The propagation of whistler mode waves through the magnetosphere can be rather complex due
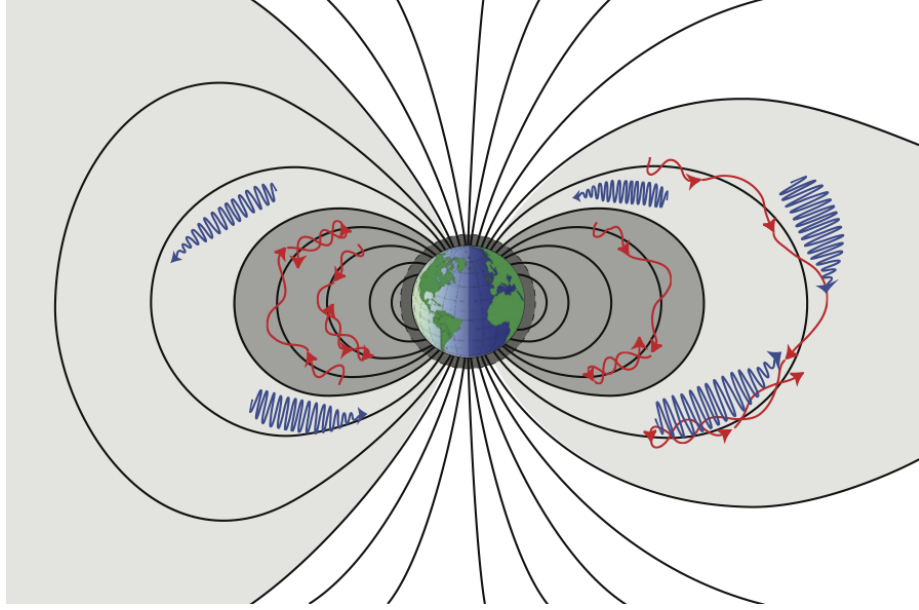
Figure 1.1: Depiction of the magnetosphere with radiation belt electrons (red) and electromagnetic waves (blue).

to the spatial variation and anisotropy of the medium even in the absence of the radiation belt electrons. Keeping track of the trajectory of an arbitrary wave packet generally requires the use of sophisticated ray tracing software that traces the angle between the wave normal vector and the geomagnetic field. In general, the trajectories are sensitive to initial conditions and can be difficult to predict; however, the magnetosphere often contains field-aligned density enhancements that can efficiently guide waves along the geomagnetic field lines. These density enhancements are knowns as "ducts" and their presence results in the contentment of the wave normal angle to values close to zero and hence largely parallel to the geomagnetic field line. Effectively, the ducts serve as waveguides (akin to optical fibers) for whistler mode waves allowing them to subsequently undergo prolonged wave-particle interactions with the radiation belt electron population [8, 35].

A useful parameter for describing position in the magnetosphere is the L-shell and is used to specify the surfaces along which particles trapped in the Earth's magnetic field move. The L-value of a given shell corresponds to the equatorial crossing, in Earth radii, of the equivalent drift shell in a tilted, off-centered dipole model of the Earth's magnetic field [28]. In rough terms, a particular L-value corresponds to the set of geomagnetic field lines which cross the magnetic equator at 'L' Earth radii from the center of the Earth. Two locations on the Earth's surface in opposite hemispheres but along the same geomagnetic field line, or L-shell, are referred to as magnetic conjugate points.
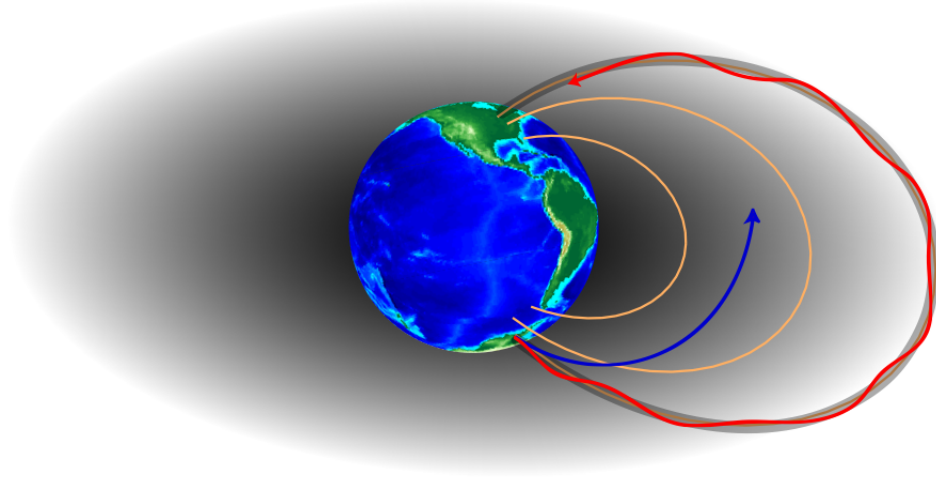
Figure 1.2: Ducted (red) versus non-ducted (blue) propagation in the magnetosphere. Adapted from [28].

1.1.1 Electron Precipitation

In the absence of any waves, the energetic radiation belt electrons remain trapped in the Earth's magnetic field constantly mirroring from hemisphere to hemisphere. Once whistler mode waves are introduced into the system, the same trapped particles can resonantly interact with them and be accelerated or decelerated depending on their initial energies and momenta. Specifically, VLF whistler-mode waves can perturb the trapped motions of the electrons, causing the mirror point to be lowered to denser regions of the Earth's atmosphere [96]. Collisions with neutral molecules in the atmosphere effectively removes the electron from its trapped motion and the electron is said to have been 'precipitated'. Wave induced electron precipitation, either by natural sources (lightning whistlers, magnetospheric chorus, hiss, etc.), or by man-made VLF transmitters, is one of the dominant loss processes in the radiation belts [1].

Previous work has evaluated several aspects of wave-induced electron precipitation. Since the growth of waves is often not considered in precipitation studies (low particle density assumption), test particle and statistical approaches have been used considerably over the past few decades [84, 4, 91, 65, 30, 63, 46, 27]. An extremely common method of evaluating particle scattering is through quasi-linear theory and the calculation of diffusion coefficients, and is a technique that has been used for over half a century [56, 1, 3, 90]. The diffusion model is useful and has been used to determine the lifetime of radiation belt electrons and protons in the presence of magnetospheric wave fields [64]. Additionally, this model has also been used to determine the source of the radiation belt slot region [65]. The diffusion model is primarily used to obtain the particle distribution over long time

scales where many interactions between waves and particles occur [4].

   The problem, however, is that the diffusion model is formally valid for small amplitude waves and in the realm of large amplitude, coherent waves, nonlinear effects dominate the wave-particle interactions and the diffusion model is not justifiable. Several authors have included these non-linear effects in modeling [50, 20, 49]; however, accurately estimating the particle distribution can be difficult without considerable computational resources. For this reason, accurate modeling of precipitation induced by large amplitude, coherent waves remains an unresolved problem.

1.2   Wave Injection Experiments

While waves in the magnetosphere scatter and precipitate electrons onto the natural atmosphere, the radiation belt electrons can in turn modify the incoming waves. Understanding this aspect of the wave-particle interaction is an equally important concern since the modified waves serve as one of the only means of remotely sensing and diagnosing the radiation belts. The existence of ducts facilitate controlled ground based experiments where waves injected from the ground travel along field-aligned ducts and are received at the conjugate hemisphere for observation. Such observations provide a means to study both the wave propagation through the cold plasma as well as the wave-particle interactions with radiation belts electrons. For instance, whistler mode waves generated by natural sources (such as atmospheric lightning) or VLF transmitters on the ground can be used to extract the cold plasma density along a ducted path [82, 19]. In such experiments, the radiation belts essentially serve as a giant plasma chamber that would be very difficult to construct in a laboratory.

1.2.1   Wave Amplification

An illustration of a wave-injection experiment concept is shown in Figure 1.3. As shown, whistler mode waves can couple into a magnetospheric duct and propagate along the magnetic field line. As the waves propagate through the radiation belts, they can interact with energetic electrons through a mechanism known as gyro-resonance (doppler shifted cyclotron resonance). The bulk of the interaction occurs close to the magnetic equator where the plasma parameters change slowly, so that the wave and electrons can undergo a cumulatively significant exchange of energy and momentum, resulting in the amplification of the injected waves. Once the wave is amplified, it continues to propagate down the field line to the northern hemisphere where it can be measured by a VLF receiver on the ground.

Siple Station

Since the equatorial gyrofrequency in the radiation belts is in the range of tens to hundreds of kHz, whistler-mode waves in this region of space are in the VLF range of frequencies. Generating waves at VLF frequencies for injection into the magnetosphere is a difficult task due to the inherently large
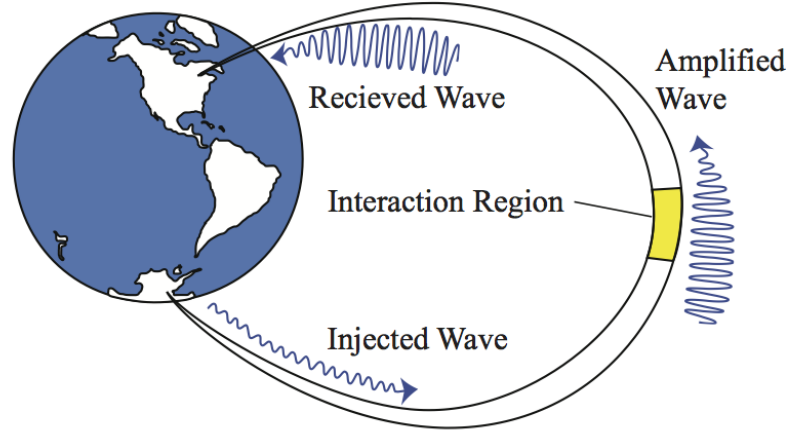
Figure 1.3: Setup for a wave injection experiment where an injected signal gets amplified by the radiation belt election population and is then received at the magnetic conjugate point.

wavelengths (tens of kilometers). Although there have been a handful of prominent experiments [38, 32], the longest and most notable magnetospheric wave injection experiment was operated by Stanford University at Siple Station, Antarctica from 1973 to 1988 [42].

The location of the facility (75.93º S, 84.25º W) was chosen because of the accessibility of its magnetic conjugate point (located in Quebec, Canada), its magnetic latitude offering access to the plasmapause, and because the site was historically known to be a good location for observations of naturally occurring magnetospheric emissions. The location of Siple Station was also chosen because of the presence of the thick ice-sheet therein (~ 2 km), thus facilitating efficient VLF radiation with a horizontal antenna. Over the fifteen year duration of the experiments, several modifications were made to the transmitting system; however, the basic design consisted of a long, horizontal dipole antenna. The placement of the antenna on top of the thick ice sheet elevated the antenna above the conducting ground plane below, thus allowing few percent radiation efficiency.

The original installation was a 80 kW transmitter and a 21.2 km antenna with resonant frequency of approximately 5 kHz [38]. This facility was later upgraded to a 150 kW transmitter and two 42 km long antennas arranged in a crossed dipole geometry leading to a resonant frequency of 2.5 kHz and an estimated radiated power of 1.5 kW [18, 40, 29]. Although the station itself was located at $L = 4.3$, the transmitter excited ducted magnetospheric wave amplification ranging from $L = 3$ to $L = 5$.

Due to the importance of frequency-time characteristics in VLF experiments, the data is often represented in the form of spectrograms. An example of the data observed from the Siple Station
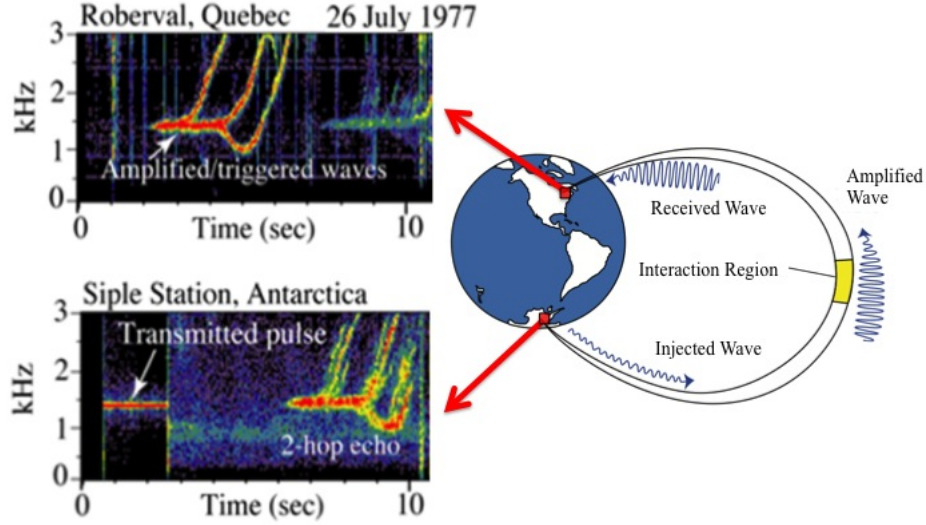
Figure 1.4: Spectrograms of signals transmitted from Siple Station (bottom) and received in Rober-val, Canada (top). Also shown is a strong two-hop echoes at the transmitter location and a weaker three-hop echo at the receiver station.

experiment can be seen in the spectrogram on Figure 1.4. The bottom spectrogram shows data observed at the transmitting station (Siple) while the top one displays the received data at the conjugate point in Roberval, Quebec. As shown, a 2 second long pulse at 1.4 kHz is initially transmitted at t=0.5 seconds. Approximately 1.5 seconds later, the signal is received in the northern hemisphere after propagation through the magnetosphere. Such a signal that has traversed through a single magnetospheric pass is referred to as a '1-hop echo'. After the first pass through the interaction region, the signal may partially reflect back into the magnetosphere and may go through a second pass. The signal is then received back at the transmitting station and is then referred to as a '2-hop echo'. Through each pass, the signals are typically amplified by several orders of magnitude and also produce free running emissions at frequencies extending well away from that of the original transmission. Although the triggering of free-running emissions is an important physical process that is not yet quantitatively understood, the amplification of these signals near their transmitted frequency is the primary topic and focus of this dissertation.

The Siple Station experiment resulted in several years of data on whistler mode wave-particle in-teractions which continue to drive current experimental and theoretical efforts in the field. However, due to the high cost of the maintenance, the station was closed in 1988 and the site was abandoned. The remnants of Siple Station are now buried under tens of meters of snow. Fortunately, the data originally recorded on analog magnetic tapes has been digitized [60] and continue to yield scientific discoveries [59, 28].

The growth of whistler mode waves due to the interaction with radiation belt electrons has been
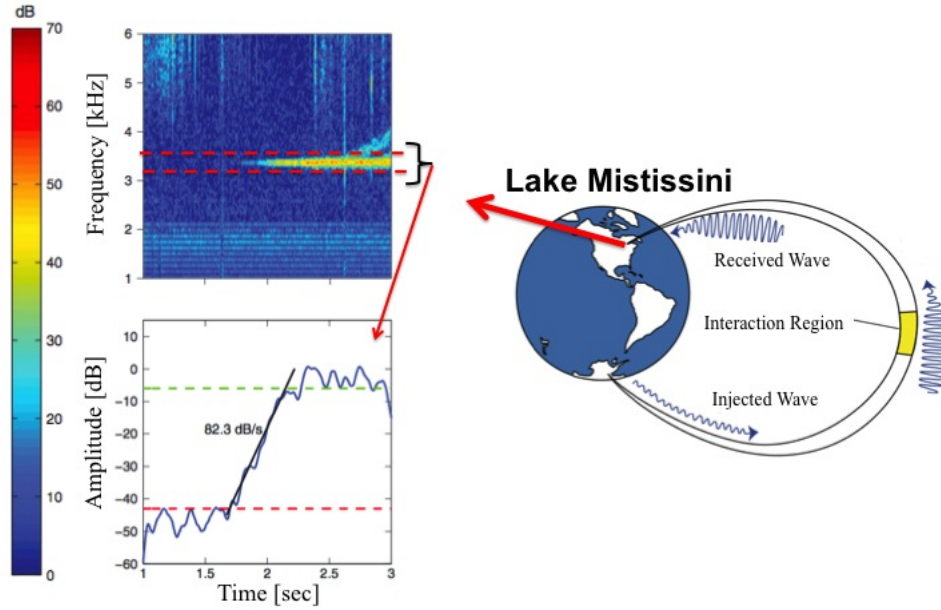
Figure 1.5: Amplified signal received at Lake Mistissini after interacting with the radiation belt electrons.

observed for more than half a century. The phenomenon is often referred to as the "VLF triggered emissions" or the "coherent wave instability" due to the inherent preference of the system to strongly amplify coherent waves as opposed to incoherent, broadband signals. The most repeatable aspects of this instability includes the exponential temporal growth of the signal from an initial low level to a saturation amplitude as measured by a receiver on the ground as well as the continuous, dynamic change in the wave frequency upon saturation (referred to as triggered emissions). Although various aspects of the phenomenon have been addressed and explained by previous scientists, the exact physical mechanisms behind the triggered emission and growth process remains an open subject of active research. A representative spectrogram of a received signal in Canada (Lake Mistissini) along with the signal amplitude at the transmitted frequency is shown in Figure 1.5. As shown, the signal amplitude is observed to undergo almost 50 dB of temporal growth at a growth rate of 82.3 dB/sec. Since the signal amplitude is shown on a dB-scale, the growth is in fact exponential in time, which is indicative of a nonlinear underlying physical process.

Much of the difficulty in investigating whistler-mode nonlinear amplification arises because the system is not analytically tractable without extremely restrictive assumptions. The most general solution to the problem requires keeping track of any electromagnetic waves in the system (with Maxwell's Equations) along with a distribution of electrons that evolves in time according to the Lorentz force. Additionally, the inhomogeneity of the background geomagnetic field adds further complexity to the problem [10, 89, 81, 41, 78].

Since the 1970s, computing resources have allowed for the use of increasingly sophisticated numerical models to tackle the coherent wave instability. Useful insight have been provided by test particle methods where the wave fields are specified (such as in [50]); however, the general problem requires the use of models that involve self consistent calculations of the fields.

Several models have been employed over the years to address various aspects of coherent wave amplification [41, 68, 81, 89, 22, 29, 76] but few have been unambiguously verified with data or simulations. One of the first self-consistent models for tackling wave amplification along with keeping track of distribution of particles used the Vlasov Hybrid Simulation (VHS) code [69]. Although this model generated results consistent with observations, it required the use of artificial filtering for algorithm stability [69, 70] making it difficult to isolate non-physical results. More recently, Particle-In-Cell (PIC) models have been used more extensively because of the availability of fast-parallel computing capabilities [45, 43, 77, 53]. Although some PIC models have been able to reproduce growth as well as rising triggered emissions; particle methods tend to be noisy since millions to billions of particles are still required to eliminate numerical noise which can sometimes render accurate predictions difficult. Additionally, these simulations often need unrealistic or exaggerated conditions to generate results that match experimental observations. Even with the existing state of the art computer simulations, there still remains several unanswered questions in regards to the coherent wave instability and additional modeling effort are necessary for advancement.

1.3 Thesis Organization

The work presented in this dissertation is organized into 5 chapters.

Chapter 1, the current chapter, describes the relevant background and motivation for examining wave-particle interactions in the Earth's radiation belts.

Chapter 2 explains the theoretical foundation of wave-particle interactions using concepts from fundamental plasma physics and electrodynamics. Specifically we discuss the Vlasov-Maxwell system of equations and the phase-trapping of cyclotron-resonant electrons by coherent whistler mode waves.

In Chapter 3 we present a "Vlasov-Liouville" (VL) numerical model of wave-induced electron precipitation that uses backward trajectory integration of the electron's equations of motion to construct the precipitated particle distribution ("Vlasov-Liouville" model).

Chapter 4 presents a self-consistent model of coherent wave amplification that keeps track of wave growth along with a phase-space electron distribution by solving the Vlasov-Maxwell system of equations using a finite difference upwind scheme.

Chapter 5 summarizes the content of this dissertation and provides suggestions for future work.

1.4   Scientific Contributions

The scientific contributions put forth in this thesis are as follows:

1. Development of a Vlasov-Liouville (VL) backward scattering model of wave induced electron precipitation which:

   (a) models the effect of coherent parallel propagating whistler mode waves on the magnetospheric electron distribution without susceptibility to under-sampling errors found in forward scattering models;

   (b) demonstrates that the validity of linear scattering theory depends not only on the wave amplitude but also strongly on the initial hot plasma distribution;

   (c) reveals that the precipitated flux is dominated by phase-trapped resonant electrons as the wave amplitude increases.

   (d) describes the time signature of the precipitated electron flux due to short duration VLF wave pulses.

2. Developed a self consistent finite difference model of nonlinear wave amplification which:

   (a) reproduces wave growth at low input amplitudes and low hot plasma densities that agrees with linear plasma theory;

   (b) demonstrates a clear transition from linear to nonlinear wave growth in agreement with theory of phase trapping of resonant electrons and in agreement with observations;

   (c) reveals the presence of a stable phase-space trap, a key feature of nonlinear theory, with higher resolution than previously attempted computer simulations.

Chapter 2

Theoretical Background

In this chapter, we consider the relevant theoretical background necessary to describe and analyze coherent wave-particle interactions in Earth's radiation belts. The most general model for the system involves tracking a distribution of hot plasma radiation belt electrons as well as the cold plasma electrons as well as any electromagnetic waves that may be present or generated. Since the problem is quite complex, we begin with a discussion of whistler-mode electromagnetic waves supported by the magnetosphere, after which the motion of electrons within these wave fields is described in detail. Once the motion of single particles is described, we use theoretical plasma physics concepts to quantify the collective effect of the radiation belt electrons.

2.1 Electromagnetic Waves

Since the focus of this thesis is the interaction between waves and particles in the radiation belts, describing the mathematical principles behind whistler-mode electromagnetic waves is a necessary task. In general, electromagnetic waves are characterized by electric and magnetic fields that are represented by $\mathbf{E}$ and $\mathbf{B}$ respectively. These electromagnetic fields must satisfy a set of partial differential equations known as Maxwell's Equations, shown below.

$$\nabla \times \mathbf{E} = -\frac{\partial \mathbf{B}}{\partial t} \tag{2.1}$$

$$\nabla \times \mathbf{B} = \mu_0 \mathbf{J} + \mu_0 \epsilon_0 \frac{\partial \mathbf{E}}{\partial t} \tag{2.2}$$

$$\nabla \cdot \mathbf{B} = 0 \tag{2.3}$$

$$\nabla \cdot \mathbf{E} = \frac{\rho}{\epsilon_0} \tag{2.4}$$

Here, the quantities ρ and $\mathbf{J}$ represent the electric charge and current densities respectively. The quantities μ_0 and ϵ_0 are the permeability and permittivity of free space and are essentially numerical constants. In the absence of any charges or currents, the solutions to Maxwell's Equations in free space are of the form $\mathbf{E}(t, \mathbf{r}) = \mathbf{E}(\mathbf{r} \pm ct)$. That is, the electromagnetic fields in vacuum propagate at speed c, the speed of light. The analysis can be taken further by considering sinusoidal frequency components. Specifically, if the fields are assumed to vary in time as $\mathbf{E} \sim e^{i\omega t}$, Maxwell's Equations require that the space-time solution is of the form $\mathbf{E} \sim e^{i(\omega t + \mathbf{k} \cdot \mathbf{r})}$. Here the quantities ω and $\mathbf{k}$ are the wave frequency and wave vector respectively. The defining feature that characterizes the wave solution is known as the dispersion relation, which is an equation that describes the relationship between the ω and $\mathbf{k}$. In the case of electromagnetic waves in vacuum, the dispersion relation is given by

$$\omega^2 - c^2 k^2 = 0 \tag{2.5}$$

Here, k is the magnitude of the wave vector, $\mathbf{k}$, and is referred to as the wave-number. Since the wave velocity (technically phase velocity) is given by $v_{\mathrm{p}} = \omega/k$, the dispersion relation in Equation (2.5) ensures that each frequency component propagates at the speed of light. In the case of the magnetosphere; however, the background medium is not free space but is instead a cold plasma. This fact adds a layer of complexity to the problem and introduces new types of wave solutions.

2.1.1 Whistler Mode Waves

As discussed in Chapter 1, the magnetosphere hosts a plasma population that is relatively cold with energies less than 1 eV. That is, the electron temperature is considered to be low enough that any waves propagating in the system have dynamics faster than the motion of electrons. Additionally, it is assumed that the ion masses are so heavy and slow that their motion can essentially be neglected; therefore, the ions simply act as a neutralizing positive charge background. Without loss of generality, the background magnetic field is considered to be in the z-direction, $\mathbf{B}_0 = B_0 \hat{\mathbf{z}}$. Once again, harmonic solutions are assumed and since we consider ducted propagation, the waves are enforced to travel along the direction of the geomagnetic field lines $\mathbf{k} = k\hat{\mathbf{z}}$. Furthermore, for such waves $\mathbf{k} \cdot \mathbf{E} = 0$ so that there is no space charge $\rho(z)$ and thus electrostatic effects are not present. Under these assumptions, it can be shown [see (A.8)] that Maxwell's Equations in absence of current sources simplify to the following system of equations:

$$\left[(k^2 - \frac{\omega^2}{c^2})\hat{\mathbf{I}} - \mu_0 \frac{\omega_{\mathrm{p}}^2 \epsilon_0}{\omega_{\mathrm{c}}^2 - \omega^2} \begin{pmatrix} \omega^2 & -i\omega\omega_{\mathrm{c}} \\ i\omega\omega_{\mathrm{c}} & \omega^2 \end{pmatrix} \right] \mathbf{E} = 0 \tag{2.6}$$

where $\hat{\mathbf{I}}$ is the identity matrix. The quantities ω_c and ω_p are known as the electron gyrofrequency and plasma frequency respectively. Specifically, $\omega_p = \sqrt{\dfrac{N_c q^2}{m\epsilon_0}}$ depends only on the cold electron density, N_c, in addition to physical constants. A more detailed explanation of the gyrofrequency will be provided in the next section. For the signals of interest, the wave frequencies are typically less than the ω_c and ω_p [88] (typical values range from tens to hundreds of kHz). By setting the determinant of the matrix in (2.6) to zero, the dispersion relation along with the allowed electric field polarization can be obtained. Specifically, the dispersion relation is given by:

$$\omega^2 - c^2 k^2 + \frac{\omega \omega_p^2}{\omega_c \pm \omega} = 0$$

As is apparent from the above equation, there are two solutions as indicated by the $\pm$ symbol. However, noting that for whistler-mode waves the frequency must be less than the gyrofrequency ($\omega < \omega_c$), only one of the solutions yields a non-imaginary wavenumber. By retaining the one solution, we end up with the dispersion relation for whistler-mode waves:

$$\omega^2 - c^2 k^2 + \frac{\omega \omega_p^2}{\omega_c - \omega} = 0 \tag{2.7}$$

From Equation (2.7), it can be seen that the first two terms are identical to that of the dispersion relation in free space (2.5). The third term in (2.7) is where the effect of the cold plasma manifests itself. If the plasma density were zero (i.e no plasma), ω_p is equal to zero and the dispersion relation for the vacuum case is retrieved. In the cold plasma case, v_p is no longer constant as in free space resulting in different frequencies propagating at different speeds. Typical whistler-mode wave velocities in the radiation belts are only about a tenth of the speed of light in vacuum.

By plugging this dispersion relation back into Equation (2.6), the electric (and magnetic) field polarization can also be obtained:

$$\mathbf{E} = E\cos(wt - kz)\hat{\mathbf{x}} + E\sin(\omega t - kz)\hat{\mathbf{y}} \tag{2.8}$$

where E is the magnitude of the electric field. Equation (2.8) shows that the electric field (and magnetic field) is right-hand circularly polarized. That is, as the wave travels along the $+z$-direction, the electric and magnetic field vectors trace out a counter-clockwise circle in the (x, y) plane. In three dimensions, the wave field vectors are observed to trace out a helix as it propagates down the field lines as shown in Figure 2.1.

In the case of a realistic inhomogeneous magnetosphere the plasma frequency and gyro frequency are functions of position along the field line. Noting that the inhomogeneity is assumed to vary over scales that are much larger than a wavelength, a slowly varying WKB approximation has been used by several authors [50, 66, 28]. The modified wave solution in the presence of a spatially varying geomagnetic field then becomes
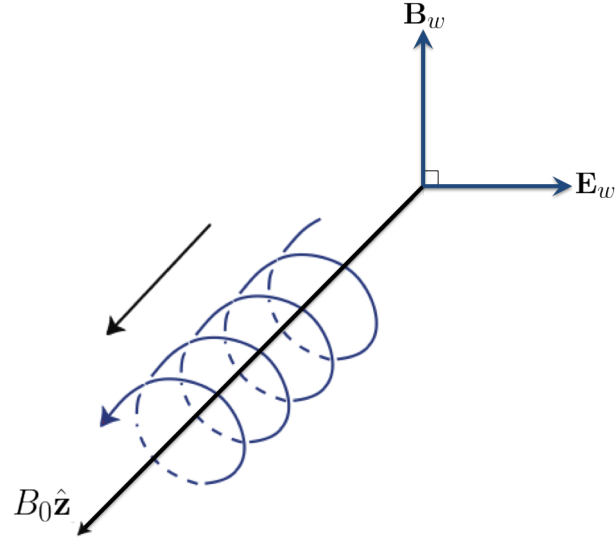
Figure 2.1: (a) The helical path traced out by a whistler mode wave as it travels down the field line.

$$\mathbf{E} = E\cos(wt - \int k\,\mathrm{d}z)\hat{\mathbf{x}} + E\sin(\omega t - \int k\,\mathrm{d}z)\hat{\mathbf{y}} \qquad (2.9)$$

which essentially replaces the term kz in (2.8) with $\int k\mathrm{d}z$. Apart from this change, the rest of the discussion on whistler mode waves remains the same as in the homogenous system.

In this Section, we considered solutions to Maxwell's Equations in a cold plasma and introduced whistler mode waves, which are the primary waves considered in this thesis. Since the overall objective is to describe interactions between waves and particles, we next discuss the single particle motion of radiation belt electrons.

2.2   Single Particle Motion

As described previously, quantifying the effect of radiation belt electrons on whistler-mode waves requires the evaluation of the collective effects of this energetic plasma. Before collective effects can be discussed, however, evaluating the trajectories of single particles can illustrate some of the complex motion that are encountered in the plasma.

2.2.1   Adiabatic Motion of Particles

The most fundamental aspect of radiation belt physics is the trajectory of an electron in the presence of the Earth's geomagnetic field. The motion of a negatively charged particle (specifically electron)
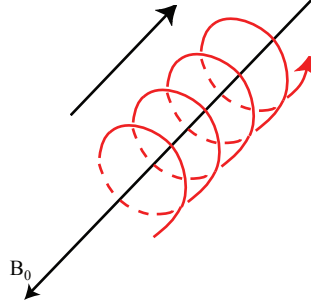
Figure 2.2: The helical path traced out by a radiation belt electron in the presence of the Earth's geomagnetic field.

in an electromagnetic field is governed by the Lorentz force. The equations of motion are given by,

$$m\frac{d\mathbf{v}}{dt} = -q(\mathbf{E} + \mathbf{v} \times \mathbf{B}) \tag{2.10}$$

Here, $\mathbf{v}$ is the electron velocity, m is the electron mass, q is the magnitude of the electronic charge while $\mathbf{E}$ and $\mathbf{B}$ are the electric and magnetic fields respectively. In the absence of waves, which is the case we consider first, the electric field is identically zero and the magnetic field is only that of the geomagnetic field. In this case, the Lorentz force is modified to

$$\frac{d\mathbf{v}}{dt} = -\frac{q}{m}(\mathbf{v} \times \mathbf{B}_0) \tag{2.11}$$

where $\mathbf{B}_0$ represents the geomagnetic field. In the simplified case of a constant magnetic field, $\mathbf{B}_0 = B_0\hat{\mathbf{z}}$, and the initial velocity has no component in the direction of $\mathbf{B}_0$ (i.e., $v_z = 0$) the Lorentz force equation has an analytical solution. In this case, assuming $|\mathbf{v}(0)| = v_0$, the trajectory is given by $\mathbf{v}(t) = v_0 \cos(w_c t)\hat{\mathbf{x}} - v_0 \sin(w_c t)\hat{\mathbf{y}}$. In other words, the electron velocity will trace out circles in the plane transverse to the magnetic field and traverses the circle at an angular frequency given by $\omega_c = qB_0/m$. The term ω_c is referred to as the gyro-frequency, or cyclotron frequency, and is a fundamental parameter of magnetodynamics. The electron position also traces out a circle with a radius given by $r_c = m|v|/qB_0$, referred to as the "gyro-radius". An interesting point to note is that the energy of an electron moving in a magnetic field remains constant because the force is always perpendicular to the direction of motion. However, the momentum of the particle is altered in such motion. This fact also means that if v_z was nonzero, this component of the velocity is not affected by the fields and remains unchanged. The resulting trajectory with a nonzero v_z traces out a helix instead of just a circle. Figure 2.2 demonstrates the helical motion of an electron in a static magnetic field.

For the purpose of this work, the geomagnetic field is assumed to be static but is not homogenous and changes as a function of position along the field in accordance with a dipole model. In this case, the geomagnetic field strength changes as a function of position. The inhomogeneity introduces new physical effects which are very important in radiation belt dynamics. The changing magnetic field in turn results in a spatially varying gyrofrequency as the electron travels along its orbit. In general, the three dimensional motion of the electron should be considered as it is influenced by the geomagnetic field. However, certain physical assumptions can be taken into account to simplify the equations of motion. First, it is assumed that any spatial changes in the geomagnetic field occur on a spatial scale that is much less than the gyroradius. Additionally, it is assumed that any changes to the geomagnetic field along the field line is greater than changes across field lines [28]. This assumption is particularly useful since it essentially reduces the problem to be spatially one-dimensional, that is, the position coordinate is simply taken to be along the field line. With these simplifications, the general equations of motion are reduced to:

$$\frac{dv_\parallel}{dz} = -\frac{v_\perp^2}{2\omega_c v_\parallel}\frac{\partial\omega_c}{\partial z} \tag{2.12}$$

$$\frac{dv_\perp}{dz} = \frac{v_\perp}{2\omega_c}\frac{\partial\omega_c}{\partial z} \tag{2.13}$$

Here, $v_\parallel$ is the component of the electron velocity in the direction of the geomagnetic field while $v_\perp$ is the magnitude of the velocity-component that is perpendicular to it. The variable z is the coordinate position along the field line. These equations describe the motion of an electron in a 1D inhomogeneous magnetic field. Integrating these equations numerically is relatively straightforward; however, there is fortunately also an analytical solution to these equations. The solution can be obtained by first considering constants of motion. As with most problems in physics, if constants of motion can be found, the trajectories can be obtained relatively easily. It can be shown that the constants of motion for Equations (2.12) and (2.13) are:

$$K = \frac{1}{2}m(v_\parallel^2 + v_\perp^2) \tag{2.14}$$

$$\mu = \frac{mv_\perp^2}{2B_0} \tag{2.15}$$

Here, K is the electron kinetic energy which is expected to be a constant of motion for a charged particle in a static magnetic field. The second constant of motion, μ is the magnetic moment of the electron and is also referred to as the "first adiabatic invariant". Thus, if the kinetic energy and the magnetic moment are known at any one particular point on the field line, the evolution of other quantities, such as $(v_\parallel, v_\perp)$, at any other point on the field line can be easily determined. It is worth noting that effects such as curvature drift are not captured by these equations and the first adiabatic invariant will be violated over longer time scales.
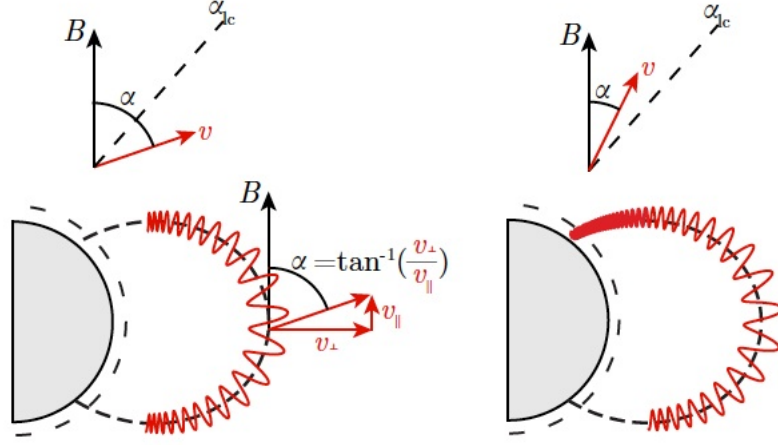
Figure 2.3: The left hand diagram shows the motion of a stably geomagnetically trapped electron in a magnetic mirror geometry when the electron pitch angle is outside the loss cone. The right hand diagram shows the case where the electron pitch angle is within the loss cone and subsequently precipitates. Adopted from [26].

Bounce Loss Cone

An important phenomena that is a result of Equations $(2.12)-(2.13)$ is that of bounce motion, or "magnetic mirroring". In order to explain this concept, a variable known as the "pitch angle" must first be introduced. The pitch angle of a particle is defined as the angle between the particle velocity vector and the local magnetic field vector. More specifically, the pitch angle can be expressed as:

$$\alpha = \arctan\left(\frac{v_\perp}{v_\parallel}\right) \tag{2.16}$$

With the substitution of this variable, the quantities K and μ can be manipulated and combined with the fact that they are constants of motion. The net result is the following:

$$\frac{\sin^2\alpha(z_{\text{eq}})}{B_0(z_{\text{eq}})} = \frac{\sin^2\alpha(z)}{B_0(z)} \tag{2.17}$$

In Equation (2.17) the term $\alpha(z_{\text{eq}})$ corresponds to the equatorial pitch angle and is the most commonly used reference point for the electron's state. That is, if the equatorial pitch angle is known (left hand side of Equation (2.17)), then the pitch angle at any other position (right hand side of equation (2.17)) can be determined. If Equation (2.17) is rearranged, the result is

$$\sin\alpha(z) = \left[\frac{B_0(z)}{B_0(z_{\text{eq}})}\right]^{\frac{1}{2}} \sin\alpha(z_{\text{eq}}) \tag{2.18}$$

Typical profiles of the Earth's magnetic field have a minimum at the magnetic equator and

increase away from the equator. Since the quantity $B_0(z)/B_0$ is always greater than one, this implies that $\alpha(z) \geq \alpha(z_{\mathrm{eq}})$. That is, the pitch angle will continue to increase as the electron travels away from the equator. Eventually, however, the pitch angle becomes large enough that it reaches 90°. This means that the component of the electron velocity in the direction of the magnetic field is identically zero when the pitch angle reaches 90°. Due to the inhomogeneity in the transverse direction, the particle does not simply stop moving but the component of the velocity in the direction of the magnetic field instead changes sign and the electron travels back in the direction it came from. This phenomenon is known as "magnetic mirroring" and the point on the field line where the electron turns around is referred to as the "mirror point", z_m, of the electron trajectory. More specifically, z_m can be obtained by explicitly setting $\alpha(z_m)$ to ninety degrees in Equation (2.17). An interesting concern, however, is if the mirror point is at low enough altitudes along the field line that the electron collides with the Earth's neutral atmosphere. Such interaction of the electron with the increasingly dense atmosphere does indeed occur and is a phenomenon known as "electron precipitation", and will be covered in much greater detail in Chapter 3. Since the equatorial pitch angle is the only feature of the electron that determines the mirror point, it is convenient to define the loss cone boundary as α_{LC}. That is, if the electron equatorial pitch angle is less than than the loss cone angle, i.e if $\alpha(z_{\mathrm{eq}}) \leq \alpha_{\mathrm{LC}}$, then the electron collides with the atmosphere before it can mirror and is consequently lost from the radiation belts. In Figure 2.3, the motion of an electron in the magnetic mirror geometry is shown along with the precipitation of an electron that is within the loss cone (angles less than α_{LC}).

In this subsection, we described the adiabatic motion of single electrons in Earth's geomagnetic field. In general, however, the presence of whistler mode waves adds significant complexity to the problem as discussed in the following subsection.

2.2.2 Electron Motion in a Whistler Mode Wave

The complete interaction between particles and waves must include every relevant plasma wave mode and any arbitrary direction of propagation. However, for simplicity, we consider only parallel propagating whistler mode signals. As mentioned previously, this assumption is quite reasonable for signals that are guided by field aligned density irregularities, known as 'ducts'. In such cases, waves generally propagate nearly parallel to the background geomagnetic field [35, 8]. Since one of our objectives is to determine precipitation induced by signals injected from the ground, the parallel propagation assumption is particularly useful. This assumption is also used in numerical modeling that is discussed in further detail in Chapters 3 and 4.

As already discussed, the motion of particles in an electromagnetic field is given by the Lorentz force, Equation (2.10). Before diving into the mathematical details of wave-particle interactions, we first present a more intuitive discussion to motivate some of the physical concepts. In the previous section, we demonstrated that both electrons as well as whistler-mode waves propagate in a helical
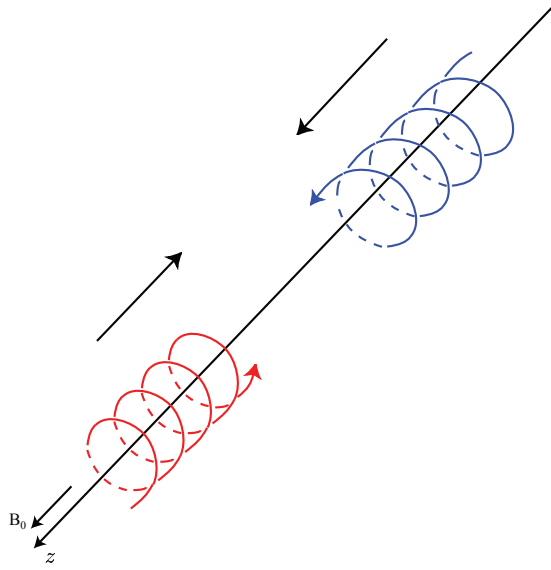
Figure 2.4: Whistler mode waves (blue) encountering counter-streaming electrons (red) at the resonance velocity, v_{res}, will force the electrons to experience an approximately stationary wave field and subsequently undergo significant energy exchange.

fashion as they travel down the field lines. This picture naturally leads to the phenomenon of "cyclotron resonance" which is depicted in Figure 2.4. Electrons streaming in the direction counter to wave propagation can experience an approximately stationary wave field as long as they moving close to the resonance velocity given by $v_{\mathrm{res}} = (\omega_{\mathrm{c}} - \omega)/k$. The expression for the resonance velocity is essentially a statement of Doppler shifting. That is, for an electron traveling at velocity $v_{\parallel}$, it sees the whistler mode wave frequency to be Doppler shifted, specifically the Doppler shifted frequency is given by $\omega_{\mathrm{Dop}} = \omega + kv_{\parallel} - \omega_{\mathrm{c}}$. The first term is the wave frequency observed in the absence of any electron velocity while the second term is due to the motion of the particle through the wave field. The third term ω_{c} takes into account that the electron is gyrating (just like the wave) and accordingly subtracts off the relative circular motion. The resonance velocity is then defined to be the velocity that satisfies $\omega_{\mathrm{Dop}} = 0$, which specifically indicates that the electron 'sees' the wave to be stationary (i.e., not rotating). Since the electron essentially experiences a constant field when in resonance, it can undergo significant energy and momentum exchange in the process and is believed to be the driving mechanism behind wave-particle interactions. Note that in order to keep v_{res} positive, it is assumed that the waves propagate in the $-z$ direction such that they are counter streaming to the electron motion.

Since ω_{c} and k change as a function of position along the field line, the resonance velocity, v_{res} will also have a functional dependence on position. Figure 2.5 shows the resonance velocity profile as

a function of position along with a "typical" test electron trajectory in the $(v_\|, z)$ plane for the case of a constant wave amplitude with constant frequency. As shown, the electron trajectory (shown in red) intersects the resonance velocity curve at exactly two points, which are also the locations where the largest degree of scattering occurs. That is, the electron trajectory is essentially adiabatic until it encounters resonance at which point the velocity will change from adiabatic but will then continue adiabatically once the particle is far enough from resonance. This type of trajectory is typical in the case of low amplitude waves or if resonance takes place far from the equator.

On the other hand, if the wave amplitude is large enough or if the resonant interactions takes place closer to the equator, a very different type of trajectory emerges and is shown in Figure 2.6. As shown, the electron trajectory (shown in red) intersects the resonance curve at around $z = -3000$km and is then forced to stay in resonance for a significant distance along the field line before being let go in the opposite hemisphere. This electron it said to have been "phase-trapped" by the wave and this process is a key feature of nonlinear interactions.

We now discuss the theoretical basis behind the phase-trapping process. By applying the Lorentz force to an electron in whistler mode wave field, Newton's Equations of motion (with relativistic corrections included) become

$$\frac{dz}{dt} = v_\| \tag{2.19}$$

$$\frac{dp_\|}{dt} = \frac{q}{m\gamma} B_{\rm w} p_\perp \sin\phi - \frac{p_\perp^2}{2\gamma\omega_{\rm c} m} \frac{\partial\omega_{\rm c}}{\partial z} \tag{2.20}$$

$$\frac{dp_\perp}{dt} = -q\sin\phi(B_{\rm w} v_\| + E_{\rm w}) + \frac{p_\perp p_\|}{2\gamma\omega_{\rm c} m} \frac{\partial\omega_{\rm c}}{\partial z} \tag{2.21}$$

$$\frac{d\phi}{dt} = -k(v_{\rm res} - v_\|) - \frac{q\cos\phi}{p_\perp}(B_{\rm w} v_\| + E_{\rm w}) \tag{2.22}$$

The quantities $p_\perp$ and $p_\|$ are the components of the electron's momentum perpendicular and parallel to the background geomagnetic field. The gyrophase angle, ϕ, is the angle between $\mathbf{p}_\perp$ and $-\mathbf{B}_{\rm w}$ (antiparallel to wave magnetic field). The terms $\omega_{\rm c}$ and $v_{\rm res}$ represent the gyrofrequency and resonance velocity respectively. The term $\gamma = \sqrt{(1 + \frac{|p|^2}{m^2 c^2})}$, is known as the Lorentz factor and is included to take relativistic corrections into account. Note that these equations show the evolution of momentum instead of velocity since it is easier to incorporate relativistic effects in this manner. In the absence of any waves, $B_{\rm w} = 0$ and $E_{\rm w} = 0$, Equations (2.20)$-$(2.21) come back to Equations (2.12) and (2.13), as long as relativistic effects are ignored (i.e $\gamma = 1$). In words, in the absence of a wave field, the mirror force (geomagnetic field) dictates the motion of particles and the trajectories are adiabatic. For a given equatorial value of $(v_\|, \alpha)$, the adiabatic particle trajectory can intersect the gyro-resonance curve $v_{\rm res}(z)$ at only two points on the field line for a dipole background magnetic field and diffusive equilibrium cold plasma density model [50] as shown in Figure 2.5.

Nonlinear scattering by coherent waves has been investigated by numerous authors using (2.19)$-$
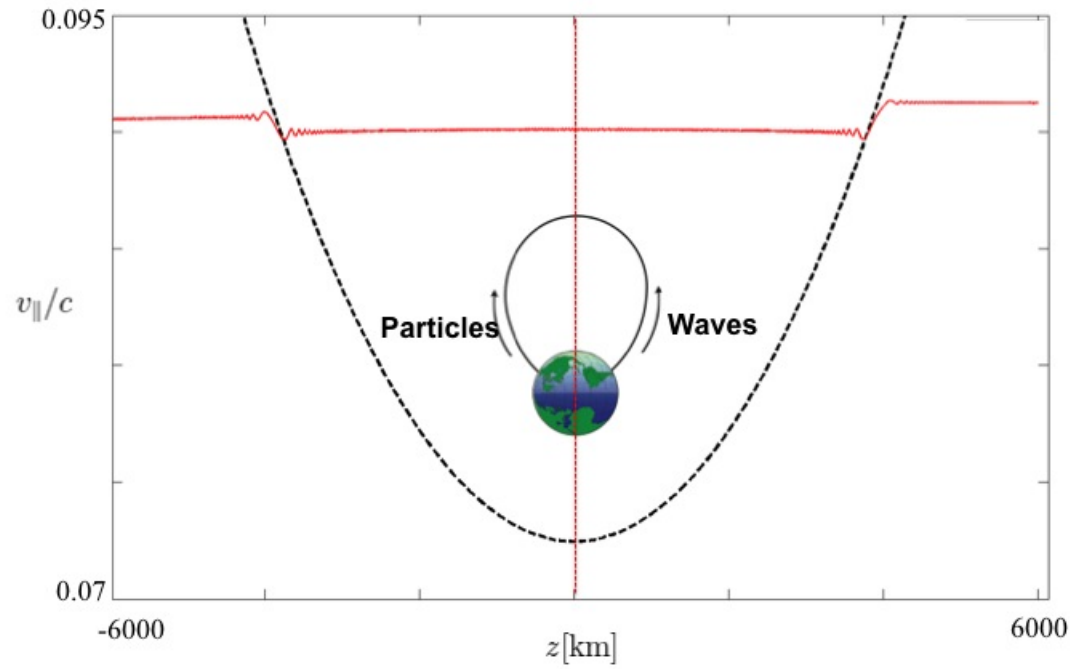
Figure 2.5: Electron in a low amplitude, monochromatic wave field that travels adiabatically until it encounters resonance at which point abrupt scattering or change in velocity takes place. The electron trajectory is shown in red along with the resonance velocity curve (in black) Typical trajectories will intersect the resonance curve at exactly two points where majority of the scattering occurs.
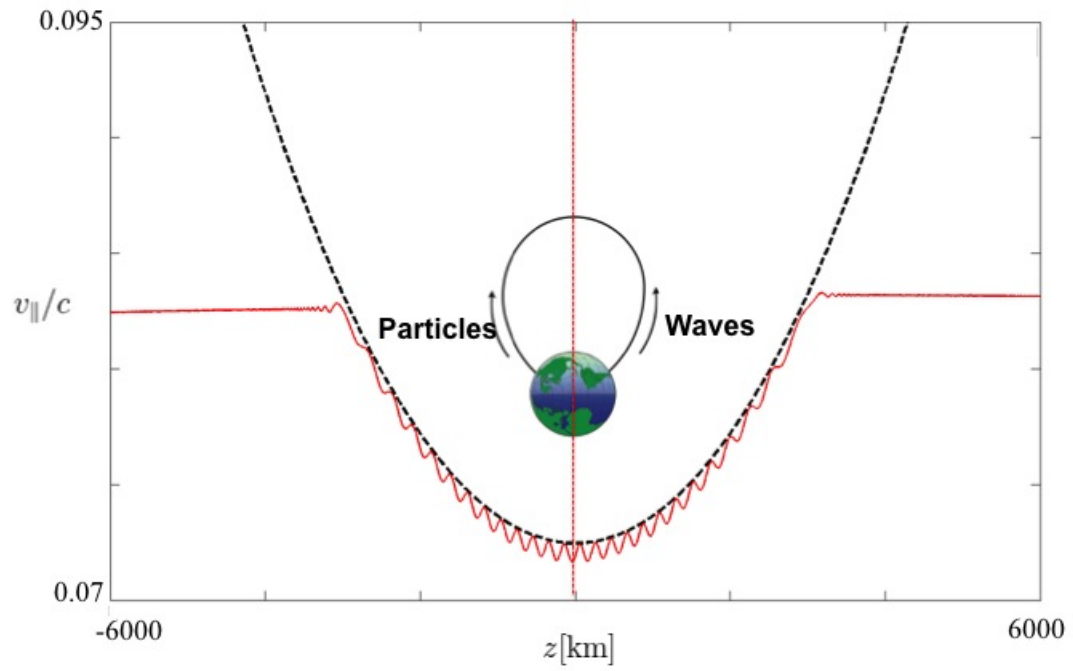
Figure 2.6: Electron in a large amplitude wave travels adiabatically until encountering resonance at which point it is forced to stay in resonance for a significant portion along the field line before being let go on the other side of the equator.
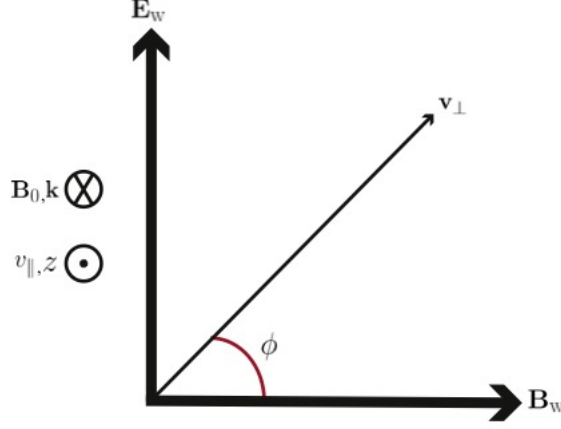
Figure 2.7: The coordinate system showing the relevant wave and particle quantities. The wave-normal vector $\mathbf{k}$ of the whistler mode wave is parallel to the background field; the wave field components, $\mathbf{B}_\mathrm{w}$ and $\mathbf{E}_\mathrm{w}$, are perpendicular to the direction of propagation. The quantities $\mathbf{v}_\parallel$ and $\mathbf{v}_\perp$ are the components of the velocity vector parallel and perpendicular to the ambient magnetic field. The gyrophase angle ϕ is the angle between $\mathbf{v}_\perp$ and $\mathbf{B}_\mathrm{w}$.

(2.22) either in their current form or by using their non-relativistic approximations [22, 81, 50, 66, 9]. These equations describe the interaction between relativistic electrons and whistler mode waves immersed in a background inhomogeneous magnetic field. The inhomogeneity of the background field is taken into account as a gradient term in (2.20) and (2.21) and is responsible for the mirroring effect as discussed in the previous section. The problem geometry is shown in Figure 2.7.

In general when the doppler-shifted wave frequency experienced by the particle equals a multiple of the gyrofrequency $(n\dfrac{\omega_\mathrm{c}}{\gamma} = \omega + kv_\parallel)$, the particle can resonate with the wave and subsequently undergo a large degree of scattering. Under the approximation of parallel propagating whistler mode waves, the $n = 1$ condition is most important and the resonance velocity is defined by,

$$v_\mathrm{res} = \frac{\dfrac{\omega_\mathrm{c}}{\gamma} - \omega}{k} \tag{2.23}$$

which is the same expression for the resonance velocity as discussed earlier except for the γ term that accounts for relativistic effects.

Phase-Space Trap

An important consequence of Equations (2.19)−(2.22) is phase trapping and the formation of a separatrix in phase-space. This concept has been studied by several authors and continues to be a topic of active research [22, 68, 50, 66, 80, 5, 29, 77, 91]. To describe the dynamics of resonant electrons,

we follow the procedure described in [77]. For simplicity, particles of non-relativistic energies are considered; however, the same framework applies for the relativistic regime. If only particles that are close to resonance are examined and the small contribution of centripetal acceleration due to the wave is neglected, Equations (2.20) and (2.22) can be simplified to (2.24) and (2.25),

$$\frac{d\phi}{dt} = k(v_\parallel - v_{\mathrm{res}}) \tag{2.24}$$

$$\frac{d^2\phi}{dt^2} - \omega_{\mathrm{tr}}^2(\sin\zeta - S) = 0 \tag{2.25}$$

where ω_{tr} is the trapping frequency and is given by $\sqrt{\frac{q}{m}B_{\mathrm{w}}kv_\perp}$. The quantity S is the "collective inhomogeneity factor" [78] and is given by,

$$S = \frac{1}{\omega_{\mathrm{tr}}^2}[\frac{kv_\perp^2}{2\omega_{\mathrm{c}}} + \frac{3v_{\mathrm{res}}}{2}]\frac{\partial\omega_{\mathrm{c}}}{\partial z} \tag{2.26}$$

The expression for S given in (2.26) assumes a constant and single wave frequency (monochromatic) and a constant plasma frequency (i.e., homogenous plasma density) . The term ω_{tr} is referred to as the trapping frequency and is given by $\omega_{\mathrm{tr}} = (\frac{qkv_\perp B_{\mathrm{w}}}{m})^{\frac{1}{2}}$. Note that the S parameter in this work is opposite in sign to the one used in [78, 77], since our waves propagate in the -z direction and not +z as in the those works. For the simplifying case of $S = 0$ (homogenous case), Equation (2.25) is identical to the well known pendulum equation. That is, the motion of the electron's $\mathbf{v}_\perp$ about the wave magnetic field, $\mathbf{B}_{\mathrm{w}}$, is analogous to the motion of a classical pendulum in a constant gravitational field. That is, for a constant gravitational field $\mathbf{g}$, the angle (ϕ) between the pendulum and the field also follows this equation. Specifically, the "trajectory" of a pendulum can be examined in the $(\frac{d\phi}{dt}, \phi)$-space, which is also referred to as "phase-space". The concept of phase-space is discussed in greater detail later in this chapter. Figure 2.8 shows the phase-space trajectory of a simple pendulum. As shown, the trajectory forms an eye-like shape; the trajectories are separated into two regions by the red dashed curve referred to as the "separatrix". Inside the separatrix, the trajectories forms closed curves, corresponding to oscillatory motion of the pendulum, that is, the pendulum never completes a full circle and simply swings back and forth. Outside the separatrix, the pendulum swings all the way around and therefore follows open trajectories in phase-space.

To illustrate the formation of the separatrix in the context of wave-particle interactions, particle trajectories must be examined in the $(v_\parallel, \phi)$ coordinate space or equivalently in the (θ, ϕ) coordinates where $\theta = \frac{k(v_{\mathrm{res}} - v_\parallel)}{\omega_{\mathrm{tr}}\sqrt{2}}$ and represents a normalized change from the resonance velocity. Figure 2.9 shows the instantaneous phase-space trajectories based on (2.24) and (2.25) assuming a monochromatic, constant amplitude signal. Figure 2.9, demonstrates the formation of a separatrix (shown by the closed red curves). Again, the separatrix divides the trajectories into two regions,
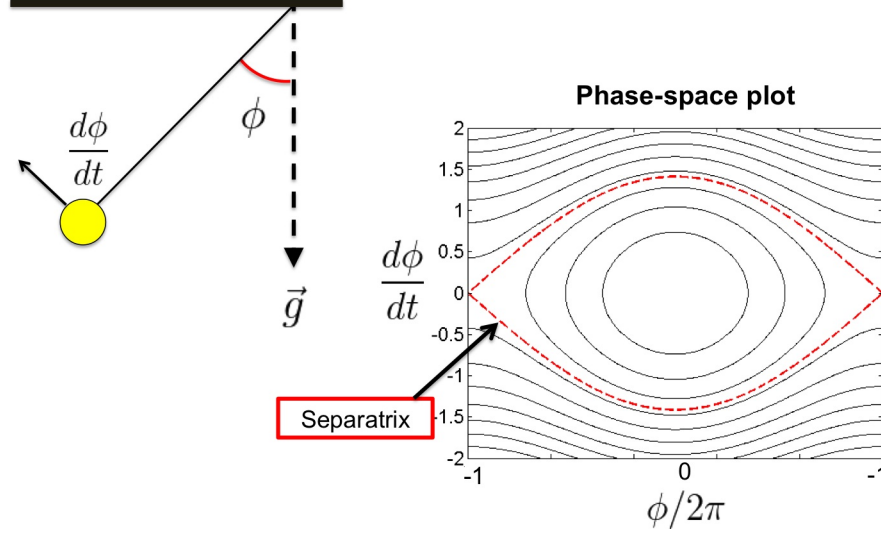
Figure 2.8: Phase-space plot corresponding to a ball on a string in gravitational field (pendulum equation). The red dashed curve represents the separatrix which divides the trajectories into closed and open contours.

trapped and untrapped. Trapped particle trajectories (interior) form closed curves while the un-trapped particle trajectories swing around the separatrix. The formation of this trap is a crucial aspect of coherent wave-particle interactions; the motion of particles in, out, and around the trap describes the nonlinear interaction. To be perfectly clear, note that in the current context trapped and untrapped particles refer to phase trapped and phase untrapped particles respectively and not to particles trapped in the geomagnetic-mirror geometry.

Note that the simplifying case of $S = 0$ only corresponds to the phase-space trajectories exactly at the equator. The inclusion of the inhomogeneity term in (2.26) ensures that S is nonzero as the electron moves away from the equator. The concept of phase trapping still carries over to the inhomogeneous problem. However, the shape of the trap changes as a function of position along the field line. At the equator, the trajectories are identical to the homogenous case. However, away from the equator, the trap shrinks and the stable phase location changes (center of trap). Far enough from the equator the trap disappears altogether. Formally, the separatrix can only exist when $-1 < S < 1$. If the background plasma were homogenous ($S = 0$), then the initially trapped particles stay trapped and untrapped particles stay untrapped. However, for a spatially dependent S, this is not necessarily the case. Particles can either swing around the trap or be trapped for many trapping periods before being detrapped. The exact dynamics are strongly dependent on the initial phase angle, energy and pitch angle of the particle [50]. This can simplify numerical modeling since the bulk of the nonlinear interaction occurs only in a narrow spatial extent around
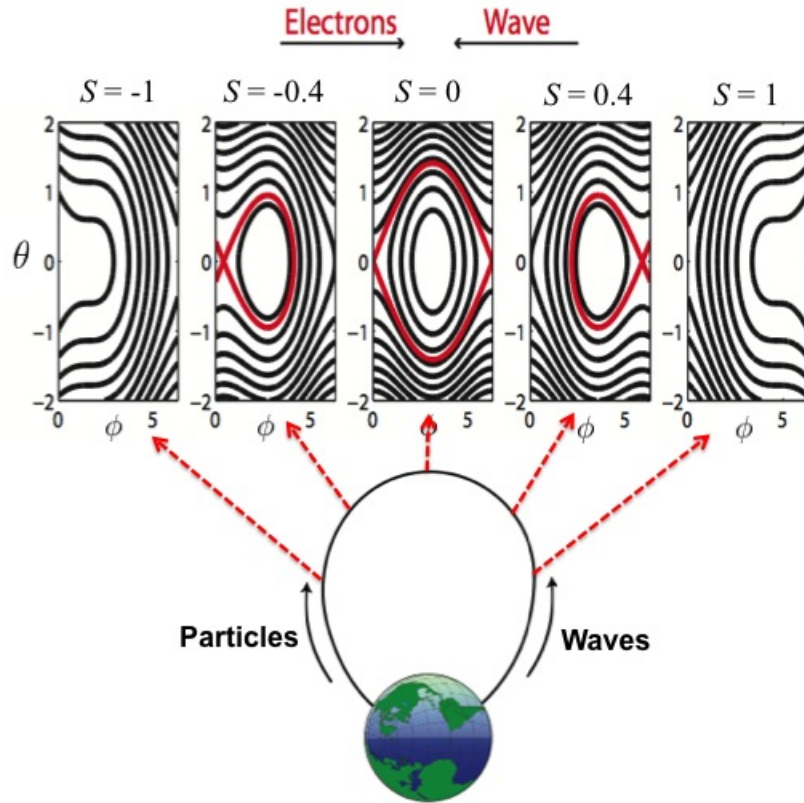
Figure 2.9: Instantaneous single particle trajectories in (θ, ϕ) coordinates for an inhomogeneous background field and monochromatic wave. The formation of a separatrix and phase-space trap is clearly visible within the region delineated by the red curves. The phase-space trap is a function of position along the field line. At the equator, the phase-space trajectories correspond to the homogenous case; however, away from the equator the trap decrease in size and the stable phase (center of trap) drifts as well. Far enough from the equator, no trap exists at all and the nonlinear wave effects become negligible. The trajectories shown correspond to $-1 < S < 1$.
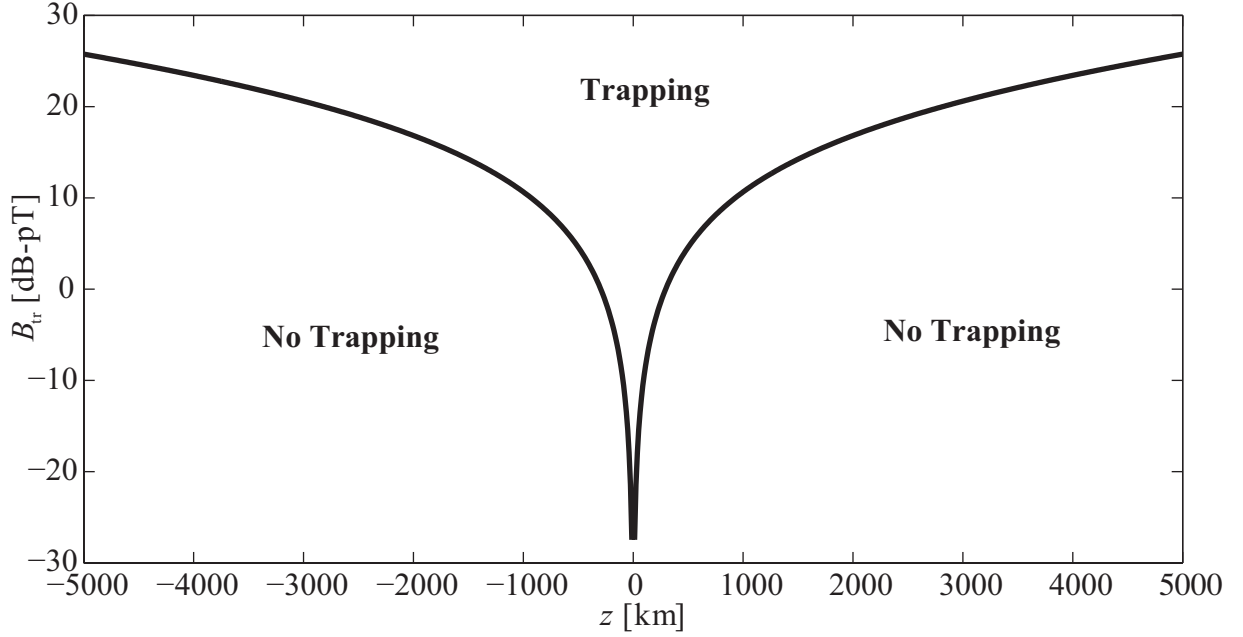
Figure 2.10: The minimum amplitude required for phase trapping resonant electrons.

the equator (where $-1 < S(z) < 1$); however, the size of the interaction region grows with the wave amplitude. This can be understood by considering the minimum amplitude required for trapping at any point along the field line. That is, for phase-trapping to occur $|S|$ must be less than unity, therefore, the minimum amplitude required to start trapping particles is that wave amplitude value for which $|S| = 1$ is enforced at a given location. Therefore, by setting $|S| = 1$ in Equation (2.26), the minimum amplitude required for trapping, B_{tr} can be solved for as follows:

$$B_{tr} = \frac{m}{qkv_\perp} \left[\frac{kv_\perp^2}{2\omega_c} + \frac{3v_{res}}{2} \right] \left| \frac{\partial \omega_c}{\partial z} \right| \tag{2.27}$$

From (2.27) it can be seen that exactly at the equator, $\dfrac{\partial \omega_c}{\partial z}$ is identically zero and there is no minimum amplitude required for trapping, i.e., any particle at resonance is inside the trap. However, moving away from the equator, the inhomogeneity increases causing B_{tr} to be higher as well.

A plot of B_{tr} (on a log scale) as a function of position is shown in Figure 2.10. As shown, for wave amplitudes below B_{tr} trapping cannot occur while for amplitudes above the threshold, trapping occurs. This concept of the trapping threshold is addressed again in Chapter 4.

So far, the theoretical concepts of trapping were demonstrated using the simplified Equations (2.24) and (2.25). Figures 2.11 and 2.12 show how trapping takes place in the context of the complete equations of motion. Figure 2.11 (b) shows the trajectories of twelve particles (uniformly distributed

in gyrophase) that have the same $v_\parallel$ and α_{eq} at the exit of the interaction region (right hand side). Figure 2.11 (b) identifies the untrapped electrons (green) and the phase trapped electrons (black). As shown, the instantaneous trajectories of trapped particles significantly deviate from the adiabatic paths and are forced to follow the local resonance velocity curve for multiple trapping periods. Although there is a large change in $v_\parallel$ on one side of the equator, there is an opposite change on the other side leading to a smaller net effect.

The change in energy and pitch angle for trapped particles has been demonstrated by several authors and the focus has often been on the interaction in only one hemisphere leading to a less symmetric change [92, 11, 25, 50]. For waves generated at the equator and propagating away from there, the interaction occurs only in one hemisphere. In the case of a ground based wave injection experiment (such as those conducted from Siple Station) the electrons will interact with the wave on both sides of the field line and result in more symmetric phase trapped trajectories as shown in Figure 2.11 (at least once the wave fills the simulation space). The corresponding change in pitch angle can be seen in Figure 2.12. As shown, the pitch angle of a trapped electron will increase (decrease) when the parallel velocity decreases (increases). The reason for this behavior is that the 'slow' nature of the whistler-mode wave enforces a higher relative change in pitch angle compared to energy [47]. The result is a change in pitch angle opposite in sign to the change in parallel velocity. Again, it is important to note that these trajectories are in the presence of a constant amplitude wave and that the trajectories would change when wave growth is introduced.

In this section, we discussed the motion of single electrons when interacting with a whistler mode wave field. In general, however, the collective response of a large number of electrons can be different from that of a single particle. Describing these collective effects requires an understanding of plasma theory, which is the focus of the next section.

2.3   Plasma Theory

Even though the motion of individual particles is interesting and instructive in its own right, it is more realistic to consider what happens to an ensemble of electrons especially if wave amplification is to be quantified. So far, it was demonstrated that motion of individual electrons can be analyzed by applying the Lorentz force to Newton's equation of motion. More specifically, Newton's Equations describe how a particle's position and velocity vary with time. In the context of such equations, the position and velocity together $(\mathbf{r}, \mathbf{v})$ define the "state" of a particle. Therefore, in order to quantify the effect of an ensemble of particles, we must examine how they evolve over the state-space, or equivalently "phase-space". That is, $(\mathbf{r}, \mathbf{v})$ can be thought of as a continuous high-dimensional space (6 dimensions in the most general case) where individual points in the space represent the state of a particle therein. In general, in order to take into account a distribution of particles, the quantity that must be tracked is a density, $f(t, \mathbf{r}, \mathbf{v})$, over phase-space. Here, $f(t, \mathbf{r}, \mathbf{v})$, represents the number
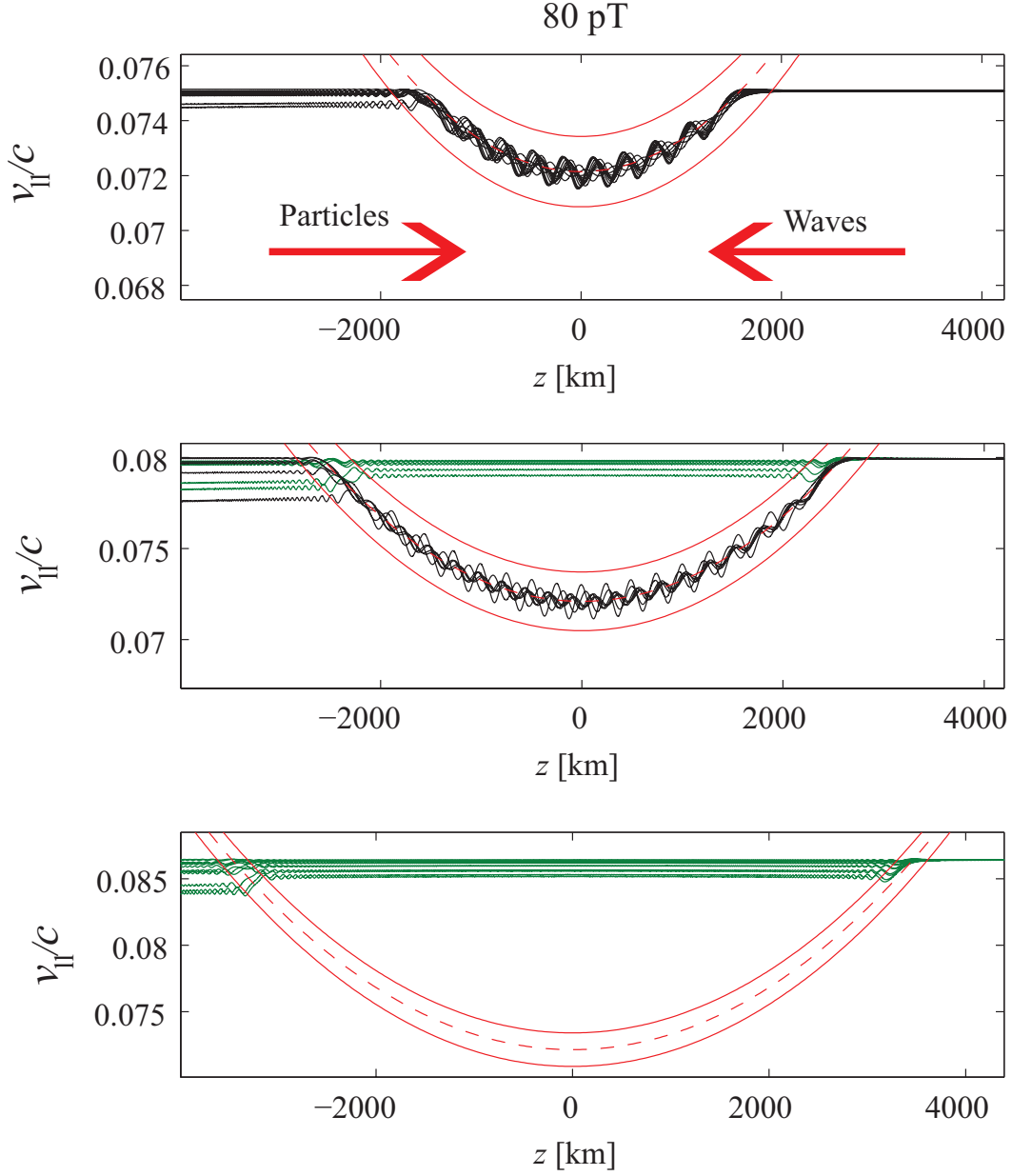
Figure 2.11: Particle trajectories for 12 particles uniformly distributed in gyrophase. Trapped particles are shown in black while untrapped particles are shown in green. The red dashed curve corresponds to the local resonance velocity while the solid red curves represent bounds of $\pm 1 v_{\mathrm{tr}}$ (size of the trap). Panel (a) shows a case where the particles' $v_\parallel$ equals the resonance velocity near the equator and are all trapped. Panel (b) demonstrates a smaller percentage of trapped particles since the resonance velocity is encountered further up the field line. Panel (c) shows only untrapped particles with no particles being phase trapped; this is because the particles' come into resonance much further up the field line (where $|S| > 1$).
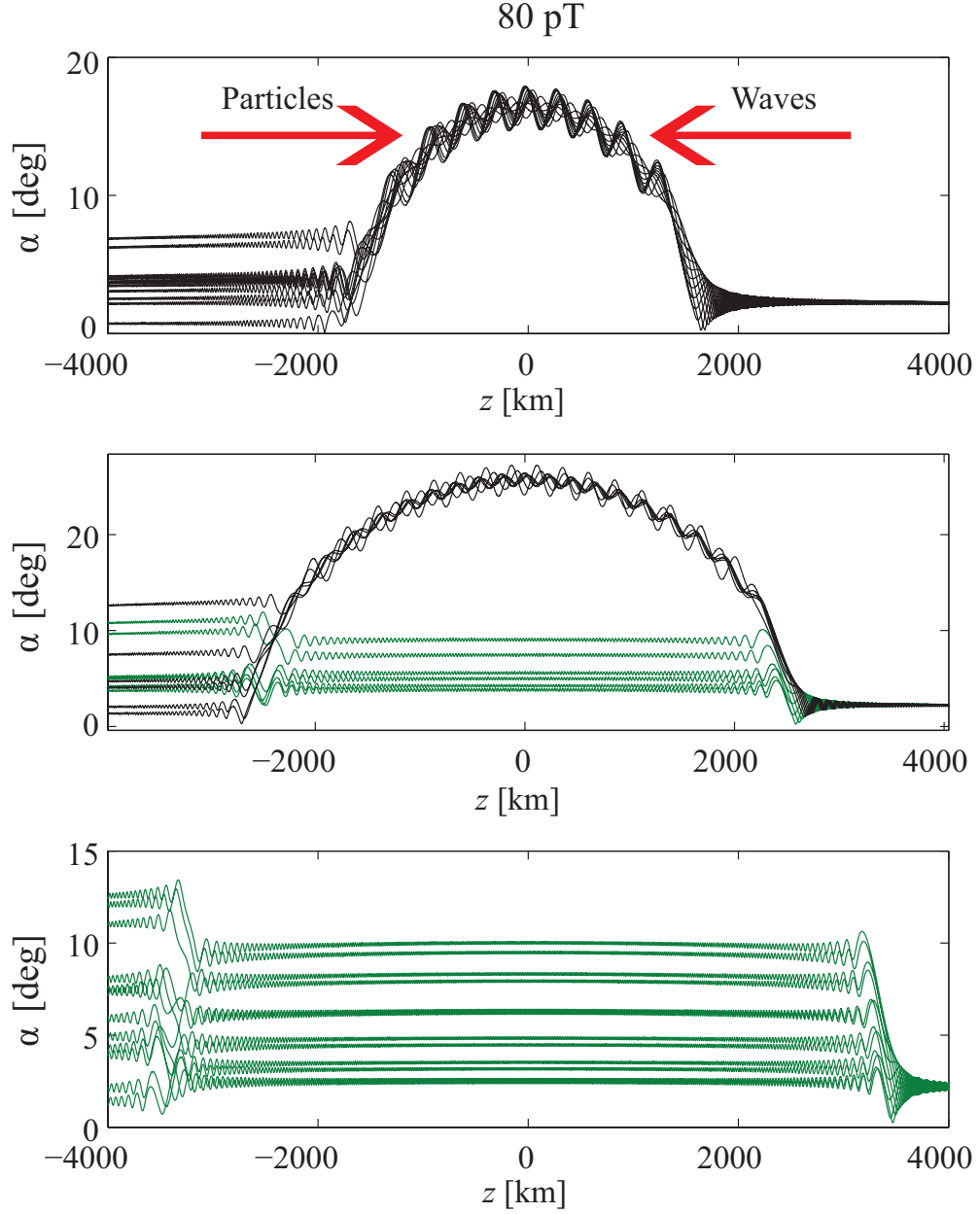
Figure 2.12: Panels (a) (b) and (c) correspond to the instantaneous pitch angle trajectories for the same particles as Figure 2.11. Trapped particles are shown in black while untrapped particles are shown in green. Note that the peak pitch angle change is very large for trapped particles; however, the net pitch angle change is still similar to that of untrapped particles.

of particles per unit phase-space volume $d\mathbf{r}d\mathbf{v}$. Note that such a representation is quite general, since even a finite collection of point particles can be described in this formalism by representing each point as a Dirac delta function in phase-space. The quantity f is referred to as the "distribution function" and our goal is to quantify its evolution as a function of time. This quantification requires the use of what is known as Liouville's theorem of Hamiltonian mechanics and is the topic of the next section.

2.3.1 Liouville's Theorem

As mentioned already, Newton's Equations along with the Lorentz force can be used to described the motion of electrons in an electromagnetic wave field. However, the equations of motions can be reformulated by using Hamiltonian mechanics. Although $\mathbf{r}$ and $\mathbf{v}$ identify the state of a particle, they can be replaced by what are known "canonical coordinates" which are represented by $\mathbf{q}$ and $\mathbf{P}$. The quantities $\mathbf{q}$ and $\mathbf{P}$ represent the canonical position and momentum respectively and are essentially any set of coordinates that can describe the particle state. With this description, the particle motion is governed by Hamilton's Equations:

$$\dot{\mathbf{P}} = -\frac{\partial H}{\partial \mathbf{q}} \tag{2.28}$$

$$\dot{\mathbf{q}} = \frac{\partial H}{\partial \mathbf{P}} \tag{2.29}$$

In these equations, $\dot{\mathbf{q}}$ and $\dot{\mathbf{P}}$ are the time derivatives of the canonical position and momentum while the quantity $H(\mathbf{q}, \mathbf{P})$ is known as the Hamiltonian of the system. For instance, the Hamiltonian for a charged particle in an electromagnetic field is given by $H = (\mathbf{P} - q\mathbf{A})^2/2m + q\Psi$ where $\mathbf{A}$ and Ψ are the magnetic vector potential and electrostatic potential, respectively. If this Hamiltonian is inserted into Equations (2.28) and (2.29), Newton's Equations with the Lorentz force are retrieved. Now that the Hamiltonian formulation of particle motion has been discussed, the connection to the phase-space distribution function, f, can be made. First we consider particles in a small phase-space hypercube. As long as collisions are neglected, which is a very accurate assumption in the radiation belts where the collision frequency is low, the particles can only leave the hypercube by passing through the faces of the cube. That is, in order to get from one point in phase-space to another, the particle takes a continuous path through phase-space and does not merely disappear at one location and reappear at another. This concept can be expressed mathematically as a continuity equation in phase-space. If we define the quantity $\mathbf{L} = (\dot{\mathbf{q}}, \dot{\mathbf{p}})f$ which represents a "current", or equivalently a flow of particles in phase-space, the continuity equation can be stated as:

$$\frac{\partial f}{\partial t} + \nabla_{qp} \cdot \mathbf{L} = 0 \tag{2.30}$$

Here the divergence operator represents a phase-space divergence $\nabla_{qp} = \left(\dfrac{\partial}{\partial \mathbf{q}}, \dfrac{\partial}{\partial \mathbf{P}} \right)$. More explicitly, the divergence of $\mathbf{L}$ is given by $\nabla_{qp} \cdot \mathbf{L} = (\dot{\mathbf{q}}, \dot{\mathbf{P}}) \cdot \nabla_{qp} f + f \nabla_{qp} \cdot (\dot{\mathbf{q}}, \dot{\mathbf{P}})$. The importance of Hamilton's Equations becomes apparent when considering the second term which includes the divergence of $(\dot{\mathbf{q}}, \dot{\mathbf{P}})$. Specifically, by applying applying $\dfrac{\partial}{\partial \dot{\mathbf{q}}}$ to (2.28) and $\dfrac{\partial}{\partial \dot{\mathbf{P}}}$ to (2.29), it is easy to show that $\nabla_{qp} \cdot (\dot{\mathbf{q}}, \dot{\mathbf{P}}) = 0$. Therefore, Equation (2.30) becomes

$$\frac{\partial f}{\partial t} + (\dot{\mathbf{q}}, \dot{\mathbf{P}}) \cdot \nabla_{qp} f = 0 \tag{2.31}$$

Equation (2.31) is known as "Liouville's theorem" and is a mathematical statement that the distribution function is conserved along single particle trajectories. To see thisresult clearly, it is useful to define the quantity $\mathbf{x} = (\dot{\mathbf{q}}, \dot{\mathbf{P}})$. With this abstraction, Liouville's theorem can be written as:

$$\frac{\partial f}{\partial t} + \sum_{i=1}^{n} \frac{dx_i}{dt} \frac{\partial f}{\partial x_i} = 0 \tag{2.32}$$

The quantity x_i represents the i-th component of the vector $\mathbf{x}$. Furthermore, it is apparent that Equation (2.32) is simply the definition of the total derivative along the particle trajectories. That is,

$$\frac{df}{dt}[t, \mathbf{x}(t)] = 0 \tag{2.33}$$

is identical to (2.32). The physical interpretation of this result is that the individual particles "see" an unchanging distribution in their own reference frames and the distribution function is essentially dragged along with the single particle trajectories. In summary, as long as individual particle motion can be described by a Hamiltonian, Liouville's theorem is satisfied.

2.3.2   Vlasov equation

As discussed previously, electron motion in an electromagnetic field can in fact be described by a Hamiltonian. Thus when applying Liouville's theorem for the electromagnetic Hamiltonian, the result is:

$$\frac{\partial f}{\partial t} + \mathbf{v} \cdot \frac{\partial f}{\partial \mathbf{r}} - q(\mathbf{E} + \mathbf{v} \times \mathbf{B}) \cdot \frac{\partial f}{\partial \mathbf{p}} = 0 \tag{2.34}$$

The quantities $\mathbf{r}$ and $\mathbf{v}$ in (2.34) correspond to the electron position and velocity. The electron momentum is $\mathbf{p}$ and is given by $\mathbf{p} = \gamma m \mathbf{v}$. Equation (2.34) is known as the Vlasov equation and describes the evolution of a collision-free electron phase-space distribution f, under the influence of electromagnetic fields. This can be seen more clearly by considering the terms that multiply $\dfrac{\partial f}{\partial \mathbf{r}}$ and $\dfrac{\partial f}{\partial \mathbf{p}}$, specifically, $\mathbf{v}$ and $-q(\mathbf{E} + \mathbf{v} \times \mathbf{B})$ respectively. These terms correspond precisely to the

Lorentz force, i.e., $\dfrac{d\mathbf{r}}{dt} = \mathbf{v}$ and $\dfrac{d\mathbf{p}}{dt} = q(\mathbf{E} + \mathbf{v} \times \mathbf{B})$ which makes sense in the context of Liouville's theorem.

We have thus made the connection between single particle motion and the evolution of a particle distribution by introducing the Vlasov equation. Since the Vlasov equations describes the evolution of an electron distribution under the influence of electromagnetic fields, the next step is to consider how the distribution in turn influences the fields. The energetic electron distribution will generate electric and magnetic fields via the electrical current $\mathbf{J}(\mathbf{r})$ and charge density $\rho(\mathbf{r})$ which must be computed and plugged into Maxwells Equations $(2.1)-(2.4)$. The current and charge density can be computed by performing the appropriate integrals over velocity-space, and are specifically given by:

$$\rho(\mathbf{r}) = -q \int \int \int f \, d\mathbf{v}^3 \tag{2.35}$$

$$\mathbf{J}(\mathbf{r}) = -q \int \int \int \mathbf{v} f \, d\mathbf{v}^3 \tag{2.36}$$

Equation (2.36) can be thought of as simply adding up the contribution of all the particle velocities, $\mathbf{v}$, to obtain the total electrical current density. Equation (2.36) shows that the charge density is computed by essentially adding up all the charges at each velocity. With these expressions for the current and charge densities, (4.9) and $(2.1)-(2.4)$ form a complete set of equations referred to as the Vlasov-Maxwell system. These equations describe the evolution of a collision-free phase-space electron distribution along with the self-consistently created electromagnetic fields. It is worth noting that in many applications, it assumed that the velocity distribution at any point in space is not far from equilibrium (Maxwellian) and the Vlasov equation can be integrated over velocity-space to obtain fluid equations [51]. However, in the context of wave-particle interactions, particles with velocities close to resonance dominate the plasma behavior and ensure that the distribution is far from equilibrium. For this reason, the Vlasov equation must be solved directly to accurately model the physics.

2.3.3   Linear Theory of Wave Growth

As discussed in the section on single particle motion, the dynamics of an electron in a wave field can be rather complicated. Since, by Liouville's theorem, the distribution function is dragged along single particle trajectories, the time-evolution of f can be difficult to obtain. Additionally, since we are interested in simultaneously quantifying the amplification of injected waves, searching for an analytical solution to the Vlasov-Maxwell system is not feasible.

Although a general analytical solution to the system is not attainable, certain approximations can be used to provide an analytical estimate of wave growth. The most common approximation is the small-signal assumption, which is generally referred to as "linear theory". Specifically, it is assumed

that any changes from the initial conditions are very "small". Specifically, we enforce $f = f_0 + f_w$ and $\mathbf{B} = \mathbf{B}_0 + \mathbf{B}_{\mathrm{w}}$ where f_0 and $\mathbf{B}_0$ correspond to the initial distribution and background magnetic field while f_w and $\mathbf{B}_{\mathrm{w}}$ correspond to the wave induced perturbations. The small signal criterion comes in by assuming $f_w \ll f_0$ and $\mathbf{B}_{\mathrm{w}} \ll \mathbf{B}_0$ and all terms higher than first order are neglected. After these assumptions, the linearized Vlasov equation becomes

$$\frac{\partial f_w}{\partial t} + \mathbf{v} \cdot \frac{\partial f_w}{\partial \mathbf{r}} - q(\mathbf{v} \times \mathbf{B}_0) \cdot \frac{\partial f_w}{\partial \mathbf{p}} - q(\mathbf{E}_{\mathrm{w}} + \mathbf{v} \times \mathbf{B}_{\mathrm{w}}) \cdot \frac{\partial f_0}{\partial \mathbf{p}} = 0 \qquad (2.37)$$

$$(\mathbf{v} \times \mathbf{B}_0) \cdot \frac{\partial f_0}{\partial \mathbf{p}} = 0 \qquad (2.38)$$

Since (2.37) and (2.38) are now linear in f_w, $\mathbf{E}_{\mathrm{w}}$ and $\mathbf{B}_{\mathrm{w}}$ we assume complex exponential solutions $\sim e^{i(\omega t - kz)}$ where we explicitly enforce propagation along the z-direction (geo-magnetic field direction), to model ducted propagation. At this point, for the sake of simplicity in analysis, it assumed that relativistic effects can be ignored and $\mathbf{p} \approx m\mathbf{v}$. Note that since this is an unstable plasma, the quantities ω and k may have imaginary components to account for wave growth. As mentioned in Section 2.1.1, wave modes are effectively characterized by a dispersion relation, i.e. the relationship between frequency and wavenumber. In this spirit, equations (2.37) and (2.38) can then be solved simultaneously with Maxwell's Equations, to give an analytical expression for the dispersion relation in a magnetized plasma [34]:

$$1 - \frac{c^2 k^2}{\omega^2} - \frac{\pi \omega_{\mathrm{p}}^2}{\omega^2 N_{\mathrm{c}}} \int \int \frac{(v_{\mathrm{p}} + v_{\parallel}) \dfrac{\partial f_0}{\partial v_{\perp}} - v_{\perp} \dfrac{\partial f_0}{\partial v_{\parallel}}}{v_{\parallel} - v_{\mathrm{res}}} v_{\perp}^2 \, dv_{\perp} \, dv_{\parallel} = 0 \qquad (2.39)$$

where N_{c} is the cold electron density and the momentum derivatives are now replaced by velocity derivatives. If there were no distribution (i.e $f_0 = 0$) then the term inside the integral vanishes and the dispersion relation in free space is retrieved. Nowhere in this discussion has the functional form of the distribution been imposed, so the analysis is quite general. However, in the case of the magnetosphere, there are two electron populations, the cold dense background plasma and the hot rarified radiation belt plasma. Therefore, the initial distribution can be separated into $f_0 = f_c + f_h$. Although the hot distribution may not be known, the cold plasma distribution is defined by

$$f_c = \frac{N_{\mathrm{c}}}{2\pi v_{\perp}} \delta(v_{\perp}) \delta(v_{\perp}) \qquad (2.40)$$

where δ represents the Dirac delta function. This is simply the mathematical statement that every particle has exactly zero velocity which means no thermal motion and the plasma is thus "cold". Furthermore, the integral in (2.39) has a root at $v_{\parallel} = v_{\mathrm{res}}$, which essentially states that the integral is dominated by the cyclotron resonant interaction. The root, however, makes the integral difficult to compute and requires contour integration in the complex plane [56]. After performing the contour

integration and including the cold plasma distribution, the dispersion relation becomes

$$1 - \frac{c^2 k^2}{\omega^2} + \frac{\omega_p^2}{\omega(\omega_c - \omega)} - i\frac{\pi^2 \omega_p^2}{\omega^2 N_c} \int \left[(v_p + v_\parallel)\frac{\partial f_h}{\partial v_\perp} - v_\perp \frac{\partial f_h}{\partial v_\parallel} \right] v_\perp^2 dv_\perp \Bigg|_{v_\parallel = v_{res}} = 0 \qquad (2.41)$$

where the real part of (2.41) corresponds to whistler mode cold plasma dispersion while the imaginary part is the additional contribution of the hot plasma. If the hot plasma distribution was not there, i.e $f_h = 0$, then the cold plasma dispersion relation is retrieved. Therefore, the Equation (2.41) demonstrates the whistler mode dispersion relation in the presence of the radiation belt plasma.

Since the hot plasma density is much smaller than the cold plasma density $(N_h \ll N_c)$, it can be assumed that the propagation characteristics of the wave are not affected by the hot plasma and are governed by the cold plasma dispersion relation. Equivalently, it is assumed that the hot plasma density is much smaller than the cold plasma and is thus only responsible for growth or damping and not propagation. Furthermore, to account for growth, it is assumed that the wave number is complex while the wave frequency is kept real, i.e., $k \to k + i\gamma_L$ where γ_L is known as the linear growth rate. With these assumptions, the analytical expression for the linear growth rate is given by [24]

$$\gamma_L = \pi \frac{\omega_c}{N_c}(1 - \frac{\omega}{\omega_c})^2 \frac{v_{res}}{v_g} \left[A - \frac{\omega}{\omega_c - \omega} \right] \eta \qquad (2.42)$$

where v_g is wave group velocity while A and η correspond to the particle anisotropy and flux respectively. Specifically, η and A are given by (3.5) and (2.44) shown below,

$$\eta = \int 2\pi f_h v_\perp dv_\perp \Bigg|_{v_\parallel = v_{res}} \qquad (2.43)$$

$$A = \frac{\int \frac{\partial f_h}{\partial \alpha} \tan \alpha \, v_\perp dv_\perp}{\eta} \Bigg|_{v_\parallel = v_{res}} \qquad (2.44)$$

The flux, η is a rather straightforward quantity and simply computes the number of particles at resonance and as such is always a positive number. The term A on other hand is the only term in the linear growth rate (2.42) that influences the sign of γ_L. Specifically, wave growth (and not damping) can only take place if the condition $\omega < \frac{A}{A+1}\omega_c$ is satisfied. Looking at (2.44), it is apparent why A captures the anisotropy in the distribution. The pitch angle α effectively contains information about the direction of the electron velocity. That is, A can only be zero if the term $\frac{\partial f_h}{\partial \alpha}$ vanishes implying that f_h does not depend on pitch angle and hence does not depend on direction, which makes it isotropic. If $\frac{\partial f_h}{\partial \alpha}$ is nonzero then A will be nonzero and contribute to growth if it is sufficiently large.
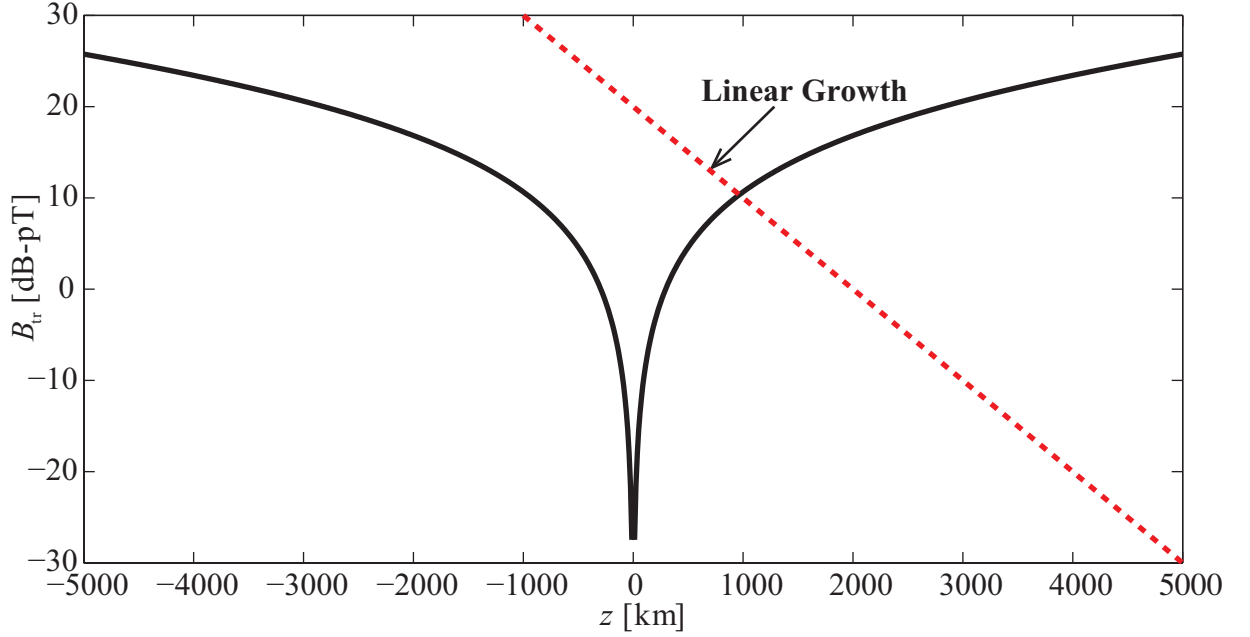
Figure 2.13: The minimum trapping amplitude along with a representative amplified wave amplitude profile based on linear theory. The wave propagates in the $-z$ direction.

We have thus shown that once the Vlasov-Maxwell system is linearized, the solutions predict exponential wave growth as long as the initial particle distribution is sufficiently anisotropic. This concept provides physical intuition behind why waves can grow. The waves essentially see the anisotropy as a source of free energy and get amplified in the process.

Although linear theory provides a reasonable physical explanation for wave amplification, it does not account for the nonlinear effects described in Section 2.2. That is, individual particles can become phase-trapped when the wave amplitude crosses a threshold B_{tr}, which is an important phenomena that is not within the scope of linear theory. In Figure 2.13, the minimum amplitude required for trapping is shown (black) with a prediction from linear theory (given an arbitrary linear growth rate) in red. As shown, for a wave propagating in the $-z$ direction, the wave will first grow according to linear theory but will eventually reach amplitudes that are above B_{tr} and the linearization assumption is no longer valid. Note that the linear theory prediction is a line in Figure 2.13 because the wave goes as $\sim e^{-\gamma_L z}$ (the minus sign is because the wave is going in the $-z$ direction) and the plot is shown on a log scale.

Since wave solutions to the Vlasov-Maxwell system will in general grow to amplitudes that can cross the trapping threshold, nonlinear effects must be taken into account. As mentioned before, this is analytically intractable and accurate computer simulations of the problem is the only available approach.

In Chapter 3, we utilize a novel backward trajectory integration method to evaluate electron precipitation induced by known wave fields. In Chapter 4, we then approach the full self-consistent problem by presenting a new numerical method for simulating wave amplification in the radiation belts using a finite difference scheme.

Chapter 3

Vlasov-Liouville Precipitation Model

In the previous chapter, we discussed the theoretical aspects behind wave-particle interactions. We showed that individual particle motion can be quite nonlinear and that accurate computer simulations are necessary to properly model the physics. In this chapter, we will present a numerical model that calculates electron precipitation induced by coherent whistler mode waves.

In modeling wave-particle interactions, two general classes of waves are usually considered, incoherent sources and coherent sources. Coherent signals have a well defined instantaneous amplitude, frequency and phase in contrast to incoherent signals which are better quantified by a power spectral density. A common incoherent whistler-mode signal is magnetospheric hiss. For precipitation studies, magnetospheric chorus is often treated as an incoherent source as well even though discrete chorus elements can be considered as coherent waves [77]. Coherent waves are usually encountered when studying scattering due to signals from VLF communication transmitters or other wave injection sources (such as Siple Station or HAARP)[40, 33, 32, 31]. Regardless of the wave structure, the full physical description of the wave-particle interaction requires correctly modeling wave amplification while self-consistently capturing the evolution of the particle distribution. As discussed in Chapter 2, the full treatment of amplification and scattering is a difficult problem that requires solving the Vlasov-Maxwell system of equations. Several authors have used Vlasov-Maxwell solvers to model wave growth [79, 29, 54, 44]. However, measuring particle precipitation in the same numerical model can be difficult to do accurately. This is because wave growth models require solving the Vlasov equation everywhere along the field line and wave growth is dominated by electrons with high pitch angles. On the other hand, precipitation is due to low pitch angle particles falling into the loss cone at the exit of the interaction region.

To quantify particle scattering, many authors consider simplified models where the wave generation mechanism is neglected. That is, waves are assumed to be generated by transmitters or by some unidentified mechanism [63]. If the density of energetic particles is small, wave growth is negligible and this assumption of 'no feedback' is valid. The wave propagation characteristics are governed by the background cold, magnetized plasma while the hot plasma (radiation belt electrons) is simply scattered by the incoming waves.

A common method of evaluating particle scattering is through quasi-linear theory and the calculation of diffusion coefficients [56, 50, 1, 3, 90]. Quasi-linear theory involves a perturbative expansion of the Vlasov equation along with averaging the (generally assumed to be incoherent) wave fields [55]. With these approximations, the Vlasov equation is transformed into a Fokker-Planck diffusion equation in pitch angle, energy and momentum. This method has been used by numerous authors to model wave-particle interactions by coherent as well as turbulent sources [65, 87, 3, 6, 30]. For instance, this diffusion model has been successfully used to explain the emptying of the slot region during periods of quiet geomagnetic activity [65]. Pitch-angle diffusion due to plasmaspheric hiss has also been used in several numerical models [90].

The primary advantage of quasi-linear theory is that the diffusion coefficients can be calculated numerically (or in some cases analytically) [63, 2, 84, 91], for a given wave power spectral density. The primary disadvantage is that it is formally valid only for small amplitude, incoherent signals. Despite this limitation, quasi-linear theory has been used to model scattering by coherent sources as well [48, 4]. In the case of coherent, large amplitude waves, the diffusive treatment is harder to justify [50]. Albert [4] showed that under certain limits, scattering by monochromatic waves can be diffusive and that quasi-linear theory is valid in this regime. However, the general treatment of nonlinear scattering (and precipitation) by large amplitude coherent waves may not be correctly handled by quasi-linear theory in which case the solution to the Vlasov equation should be computed directly. Inan et al. [50] computed precipitated fluxes due to monochromatic waves by using a semi-Vlasov solver. Although their model solved the nonlinear equations of motion to calculate pitch angle change, gyrophase dependence was neglected when reconstructing the energetic particle distribution function. For large amplitude waves, phase bunching and phase trapping are important aspects of the nonlinear process [22, 66, 9, 29, 68, 7], and it is therefore more appropriate to use a model that retains the gyrophase dependence of the particle distribution function to correctly model the physics.

Recent observations of chorus amplitudes on THEMIS [61] show values of up to 300 pT indicating the need to understand the effects of very large amplitude waves especially since chorus waves are capable of precipitating energetic electrons [62]. Although current VLF transmitters do not routinely inject such large amplitude waves into the magnetosphere, a thorough theoretical understanding would benefit any future projects on controlled precipitation.

In this chapter, we address three main points in regards to precipitation by coherent waves.

First, we discuss numerical modeling of precipitation using a characteristic based solution to the Vlasov equation (Vlasov-Liouville model). Second, we evaluate the net effect of phase-trapping on precipitation, which is a phenomenon that has often been neglected in previous models. Third, we compute the dependence of precipitated flux on wave amplitude (up to 200 pT) and compare it to linear scattering theory for different hot plasma distribution functions. We also discuss the uses of the Vlasov-Liouville model in simulating the time evolution of the precipitated flux induced by short duration whistler mode pulses (0.5 seconds in this study).

3.1   Model Description

In this section, we present numerical modeling of particle precipitation by coherent waves using the Vlasov-Liouville model. We first describe the general parameter space before proceeding to describe the numerical method employed. All simulations are performed using a centered dipole geomagnetic field model, at $L = 4$. We use the cold density model from [16] to determine the equatorial cold plasma parameters under quiet geomagnetic conditions. The cold plasma density along the field line is then determined using a diffusive equilibrium (DE-1) model [57]. At $L = 4$, the equatorial gyrofrequency is $f_c = 13.6$ kHz; the simulations use an input wave frequency of $f_0 = f_c/3 = 4.5$ kHz and a cold plasma density of $N_{\mathrm{cold}} = 400$ el/cm^3.

In addition, we assume field aligned propagation (ducted waves) in the whistler mode. Two families of particle distributions are considered for the energetic electrons. The first is a loss cone bi-Maxwellian distribution that takes the following functional form at the equator,

$$f(p_\parallel, p_\perp) = C_b e^{-\frac{p_\parallel^2}{2p_{\mathrm{th}\parallel}^2}} \left[e^{-\frac{p_\perp^2}{2p_{\mathrm{th}\perp}^2}} - e^{-\frac{p_\perp^2}{2\beta p_{\mathrm{th}\perp}^2}} \right] \tag{3.1}$$

The term β is a configurable parameter ($0 < \beta < 1$) such that larger values of β give a more depleted loss cone while $\beta = 0$ is a pure bi-Maxwellian [24]. The quantities $p_\perp$ and $p_\parallel$ are the particle momenta perpendicular and parallel to the geomagnetic field respectively. Additionally, $C_b = \dfrac{N_{\mathrm{h}}}{(1-\beta)p_{\mathrm{th}\parallel}p_{\mathrm{th}\perp}^2(\sqrt{2\pi})^3}$, N_{h} is the hot plasma density and $p_{\mathrm{th}\parallel}$ and $p_{\mathrm{th}\perp}$ represent the average momenta (of the hot plasma) parallel and perpendicular to the geomagnetic field. All simulations use $v_{\mathrm{th}\perp} = .4c$ and $v_{\mathrm{th}\parallel} = .17c$ where c is the speed of light in free space. These values are selected since they provide an anisotropy that is conducive to wave growth if the hot plasma density is high enough. The second distribution is a sin-alpha distribution and is given by,

$$f(\alpha, p) = C_s \frac{(\sin\alpha)^{\gamma_s}}{p^m} \tag{3.2}$$

where C_s is a normalization constant. The quantities γ_s and m are configurable parameters that define the distribution. Regardless of the distribution, the model explicitly enforces $f(\alpha < \alpha_{\mathrm{LC}}) = 0$

to ensure an initially empty loss cone. This also ensures zero precipitated flux for zero wave field.

The wave fields are taken into account by illuminating the entrance of the interaction region with an input signal and using this as a boundary condition for the wave equations. Since all the waves in this study exist over a small range of frequencies, the narrowband approximation of Maxwell's Equations is used to minimize computational effort. The narrowband wave equation is,

$$\frac{\partial B_\mathrm{w}}{\partial t} - v_\mathrm{g}\frac{\partial B_\mathrm{w}}{\partial z} = 0 \tag{3.3}$$

and describes the advection of a wave packet in $-z$ direction with velocity $v_\mathrm{g}(z)$. Modified versions of this equation have also been derived by several authors to model coherent wave particle interactions (generally including a source term) [68, 79, 28, 29]. Note that Equation (3.3) is used only to save on computational effort; it can be replaced by Maxwell's Equations for general (not narrowband) wave fields.

A fourth order Runge-Kutta (RK4) time stepping scheme is used to evolve the single particle equations of motion $(2.19)-(2.22)$. The wave equation, on the other hand, is time stepped using a semi-lagrangian scheme with cubic spline interpolation. That is, the wave amplitude at every particular grid location is assumed to move forward at the local group velocity at each time step which will move the wave fronts away from the grid points. The wave amplitude is then updated at the grid points by using a cubic spline interpolation.

3.1.1   Vlasov-Liouville (VL) Model

The Vlasov-Liouville numerical model essentially solves the Vlasov equation for given a wave field at a particular location along the field line. The Vlasov equation governs the evolution of collisionless plasma in phase-space $(\mathbf{r}, \mathbf{p})$ and is shown below; the terms in parenthesis correspond to Equations $(2.19)-(2.22)$.

$$\frac{\partial f}{\partial t} + \left(\frac{dz}{dt}\right)\frac{\partial f}{\partial z} + \left(\frac{dp_\parallel}{dt}\right)\frac{\partial f}{\partial p_\parallel} + \left(\frac{dp_\perp}{dt}\right)\frac{\partial f}{\partial p_\perp} + \left(\frac{d\phi}{dt}\right)\frac{\partial f}{\partial \phi} = 0 \tag{3.4}$$

Since we are only interested in whether or not particles at the exit of the interaction region fall into the loss cone, it is unnecessary to commit computational resources to solve for the distribution function everywhere along the field line. However, since the Vlasov equation is an advective type PDE, information propagates around phase-space in a complicated manner. That is, the distribution function at the exit of the interaction region depends on the distribution at many other locations in phase-space at previous times.

An accurate method of computing the distribution is by using the method of characteristics, which in the context of the Vlasov equation, is equivalent to Liouville's theorem. This is done by considering characteristic curves, which are curves along which the distribution function is advected and are equivalent to single particle trajectories. This turns the PDE into a set of ODEs. In the

case of the Vlasov equation, the characteristic curves are found by solving $(2.19)-(2.22)$. This means the value of the distribution function at any particular point can be determined by tracing the characteristic curves back until time zero. As long as characteristics do not intersect (which is the case for the Vlasov equation), this method works very well. In this method, a grid is generated over $(\phi, v_\parallel, \alpha)$ in the loss cone at the exit of the interaction region. The characteristics are traced backwards (formally $dt \to -dt$ for the equations of motion and narrowband wave equations) until time zero or until they reach the "entrance" of the interaction region. Similar procedures have been used by previous authors in modeling particle dynamics [72, 86]. This method essentially solves the Vlasov equation using the backward integration of test particle trajectories.

It is assumed that the numerical interaction region is large enough that outside this region the distribution function is essentially unperturbed since only one pass through the interaction region is considered. This allows the simulation to stop before reaching time zero, hence saving on computational time. Therefore, for a sampled set of times, the loss cone distribution function can be obtained. To evaluate precipitation, an integral is computed over the loss cone to obtain a precipitated flux. Since the VL model directly computes the phase-space distribution function, characterizing precipitation requires computing the appropriate integral. To quantify precipitation, two different measures are utilized, the precipitated flux F_p in el/m^{2}s and the precipitated energy flux E_p in J/m^{2}s. Equations $(3.5)-(3.6)$ explicitly show the integrals in the $(\alpha, \phi, p_\parallel)$ coordinate system.

$$F_p = \int_{-\infty}^{\infty} \int_{0}^{\alpha_{\mathrm{LC}}} \int_{0}^{2\pi} v_\parallel f(\alpha, \phi, p_\parallel) p_\parallel^2 \frac{\sin(\alpha)}{\cos(\alpha)^3} d\phi d\alpha dp_\parallel \tag{3.5}$$

$$E_p = \int_{-\infty}^{\infty} \int_{0}^{\alpha_{\mathrm{LC}}} \int_{0}^{2\pi} v_\parallel (m\gamma c^2 - mc^2) f(\alpha, \phi, p_\parallel) p_\parallel^2 \frac{\sin(\alpha)}{\cos(\alpha)^3} d\phi d\alpha dp_\parallel \tag{3.6}$$

Figure 3.1 shows sample trajectories that demonstrate how the loss cone is being filled at the exit of the interaction region. The actual particle trajectories flow from left to right. However, in the Vlasov-Liouville method, the scattering is performed backwards in time and the trajectories are computed from right to left. As can be seen in Figure 3.1, particles that end up in the loss cone (on the right) start with various initial pitch angles and can be scattered in complicated ways. The local loss cone is shown in red, and is calculated by providing an initial equatorial loss cone pitch angle value and constructing the rest of the curve according to adiabatic motion. All trajectories that start from inside the loss cone (on the left) and end up in the loss cone (on the right) do not contribute to precipitation (at least for an initially empty loss cone). Only particles that start outside the loss cone (on the left) and end up inside the loss cone (on the right) will contribute to precipitation (for an initially empty loss cone).

The VL model requires a grid in phase space and the range of initial $v_\parallel$ and α must be chosen correctly. The simulations use an interaction region that is approximately $\pm$ 6000 km around the
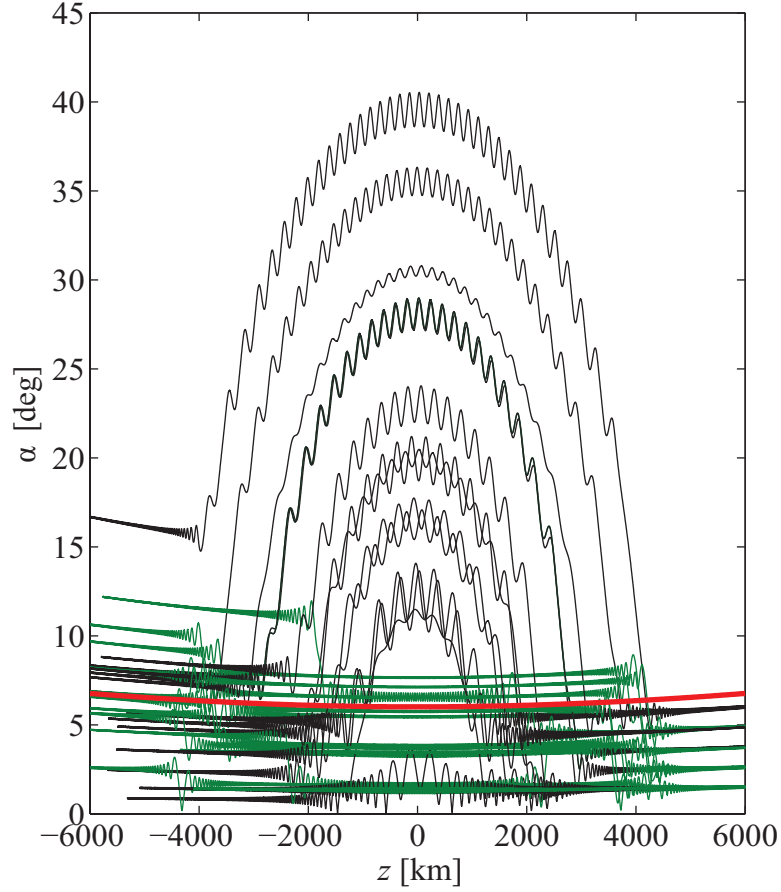
Figure 3.1: Thirty randomly selected pitch angle trajectories from the Vlasov-Liouville model (B_w = 80 pT). The particles' initial conditions sample the loss cone at the "exit" of the interaction region (right), the trajectories are then tracked backwards in time until they reach the "entrance" of the interaction region (left). Only trajectories that are above the local loss cone angle at the left side of the interaction region contribute to a non-zero precipitated density (for an initially empty loss cone). Trapped particles are shown in black, and untrapped particles are shown in green. The local loss cone is represented by the solid red curve.

geomagnetic equator and the spatial grid resolution is kept fine enough to resolve the wave amplitude equation 3.3. The phase space grid has $N_{v_\parallel} \times N_\alpha \times N_\phi = 200 \times 50 \times 32 = 320{,}000$ grid points. Since only the precipitated distribution function is of interest, the phase space grid consists of $0 < \alpha < \alpha_{\mathrm{LC}}$.

3.1.2 Comparison to Monte Carlo simulation

The VL model was chosen to analyze precipitation because the loss cone is very well defined. This way, the phase space grid is created precisely over the loss cone at the exit of the interaction region and the trajectories are traced backwards in time until reaching the entrance (or time zero). In this manner, only the trajectories that fall into the loss cone are kept track of, a feature which saves significant computational effort.

In contrast, a more brute force approach would use a Monte Carlo type simulation. A Monte Carlo model first starts by treating the particle distribution as a probability distribution and sampling it with a number of test particles. Then, the particles are essentially "let go" and are subjected to follow the equations of motion. A genuine concern with this model is ambiguity as to whether the distribution has been sampled with enough particles to capture the nonlinear effects. This is similar to the concern faced by PIC (Particle in Cell) simulations. Only a fraction of particles fall into the loss cone per time step which means a very large number of particles are necessary to extract the precipitated particle distribution (much higher than the VL model). In PIC simulations of wave-particle interactions, it is not uncommon to use 10^8 super-particles [44]. Thus, when considering precipitation, the VL model saves on computation by only tracking the relevant trajectories. The VL model has the added advantage of being easily parallelizable. Each particle can be scattered independently and the time sample when precipitation is measured can be computed in parallel. The VL method is limited by how well the grid is sampled in phase space. However, convergence can easily be determined by simply increasing the number of grid points and verifying that the results are no longer changing (within some tolerance).

3.2 Simulation Results

In the following subsections, we describe the use of the developed model to address two primary aspects of precipitation induced by coherent waves: (1) the effect of phase trapping on precipitation, (2) comparison of simulated precipitated flux to linear scattering theory for different initial particle distributions (over $0 < B_{\mathrm{w}} < 200$ pT). In the last subsection we demonstrate the ability of the VL model to compute the precipitated particle flux as a function of time for short duration input pulses.

3.2.1 Effect of Phase Trapping

As discussed in Chapter 2, resonant particles with certain gyrophase angles can be phase trapped by the wave for multiple trapping periods. The VL model is used to quantify the probability of trapping and the net scattering of phase trapped particles. A grid is created in phase space $(v_\parallel, \alpha, \phi)$ at the exit of the interaction region and the characteristics are then traced backwards in time. The trajectories of the resonant particles are then categorized as either phase trapped or untrapped. As a search criterion, a trajectory is considered trapped based on the number of crossings of $v_\parallel$ through resonance. That is, untrapped electrons will intersect the resonance curve exactly twice while trapped particles will cross resonance more than twice. Particles with $v_\parallel$ close to $v_{\mathrm{res}}(z_{\mathrm{eq}})$ will come into resonance close to the equator; since $S(z)$ is smallest near the equator, the likelihood of being phase trapped is high for these particles. Particles with $v_\parallel > v_{\mathrm{res}}(z_{\mathrm{eq}})$, will come into resonance away from the equator and the likelihood of trapping decreases (since $S(z)$ is larger). Figure 2.11 illustrates this concept. Figure 2.11 (a) shows twelve particles at a lower $v_\parallel$ such that they come into resonance close to the equator (± 1800 km). As shown, all the particles are phase trapped. Figure 2.11 (b) shows particles that come into resonance further down the field line (± 2500 km); as shown, about half the particles are phase trapped and half untrapped. Figure 2.11 (c) shows particles that come into resonance even further down from the equator (± 3200 km); in this case, none of the particles are phase trapped and all are untrapped. This clearly illustrates the dependence of the likelihood of trapping on final $(v_\parallel, \alpha)$. From Figure 2.11, it is expected to see a high percentage of trapped particles for velocities close to $v_{\mathrm{res}}(z_{\mathrm{eq}})$ and a decrease at higher values of $v_\parallel$. Figure 2.12 shows instantaneous pitch angle trajectories of the same particles as Figure 2.11.

Using the trapping criterion described, the percent of particles that become trapped (in gyrophase) can be computed as a function of $(v_\parallel, \alpha)$. Figure 3.2 shows the percent of particles trapped as a function of $(v_\parallel, \alpha_{\mathrm{eq}})$ for three different wave amplitudes (60 pT, 140 pT and 200 pT) . As shown, the percentage of trapped particles is higher for $v_\parallel$ close to $v_{\mathrm{res}}(z_{\mathrm{eq}})$ and falls off at larger parallel velocities for all three wave amplitudes. For the 60 pT case, very few particles are trapped in a small range of parallel velocities around $v_{\mathrm{res}}(z_{\mathrm{eq}})$. For the 140 pT case, a larger percentage of the particle population is trapped with 100 percent being trapped around $v_{\mathrm{res}}(z_{\mathrm{eq}})$. For 200 pT, an even larger number of particles are trapped with a one hundred percent likelihood of trapping over a significant portion of phase space. Figure 3.2 demonstrates how very large amplitude waves can trap a larger number of phase space trajectories; however, the more practical question is how much of the total precipitation is due to trapped particles and how much is due to untrapped particles. Since the trajectories of precipitated particles have been computed over a large number of initial (or rather final) conditions, a probability distribution over equatorial pitch angle change, $p(\Delta\alpha_{\mathrm{eq}})$ can also be computed using kernel density estimation. That is, if the variables $(v_\parallel, \phi)$ are not considered and only the pitch angle change is measured, the quantity $\Delta\alpha_{\mathrm{eq}}$ can be treated as a random variable. Here, the quantity $\Delta\alpha_{\mathrm{eq}}$ is computed by subtracting the equatorial pitch angle at the entrance from

the equatorial pitch angle at the exit.

The quantity $p(\Delta\alpha_{eq})$ can be compared to the distributions for trapped and untrapped particles ($p(\Delta\alpha_{eq} \cap trapped)$ and $p(\Delta\alpha_{eq} \cap untrapped)$) to see which particle population dominates. Since the untrapped and trapped particle populations are mutually exclusive, $p(\Delta\alpha_{eq}) = p(\Delta\alpha_{eq} \cap trapped)$ $+ p(\Delta\alpha_{eq} \cap untrapped)$.

Figure 3.3 shows a comparison of the different probabilities for three different wave amplitudes (60 pT, 140 pT and 200 pT). As shown, for the 60 pT case, $p(\Delta\alpha_{eq} \cap untrapped)$ and $p(\Delta\alpha_{eq})$ are almost identical indicating that the net scattered population is dominated by the untrapped trajectories. At 140 pT, $p(\Delta\alpha_{eq} \cap trapped)$ becomes more important and at 200 pT, there is a comparable contribution from both the trapped and untrapped population since scattering due to trapping is no longer negligible at such large amplitudes. The results suggest that for large wave amplitudes (greater than 100 pT), phase trapping is an important effect when considering precipitation. Note that all particles in the probability distributions are in the loss cone at the exit of the interaction region. The positive values of $\Delta\alpha_{eq}$ then correspond to trajectories that were already in the loss cone and simply got pushed to a higher pitch angle that is still in the loss cone. These trajectories will not contribute to the precipitated flux for an initial distribution with an empty loss cone.

3.2.2 Comparison to linear theory

For a constant amplitude wave filling the simulation space (CW wave), the precipitated energy flux can be computed. The VL model only requires the computation of one pass through the interaction region for a constant wave field. That is, the particles begin at the exit of the interaction region and are scattered backwards in time until they reach the entrance. Due to the spatial symmetry of a constant wave field, the scattering only needs to be computed once; every pass through the interaction region (with initial conditions over a phase-space grid) will result in the same particle trajectories. The distribution function is assumed to be unperturbed at the entrance and Liouville's theorem is used to determine the precipitated distribution at the exit. The fixed entrance boundary condition is a simplifying assumption used in this model but can be improved upon in future work.

By computing the precipitated flux as a function of amplitude, the results of the model can be compared to linear scattering theory. Linear theory is a perturbative model of the wave particle interaction phenomenon and is derived under the assumption of "small" wave amplitude. The derivation of expressions for the precipitated flux due to linear theory is presented in the appendix. Since the precipitated flux depends on the particle distribution, we compute the precipitated flux as a function of wave amplitude for different initial distributions (described in Section 3.1). Figure 3.4 shows the precipitated flux for three different bi-Maxwellian parameters ($\beta = 0$, $\beta = .45$, $\beta = .95$). Additionally, the precipitated flux due to linear scattering theory is shown for comparison in each panel. As shown, linear theory is valid for low amplitudes and then deviates from the VL model at large amplitudes as expected. An interesting finding is the degree which linear theory matches
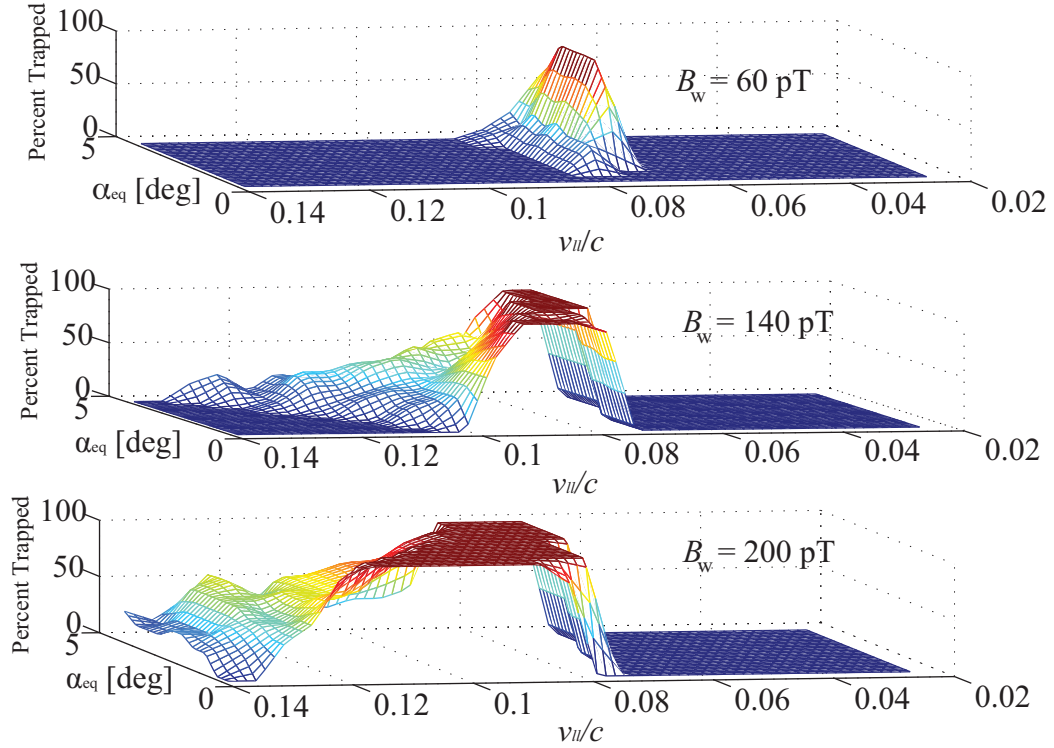
Figure 3.2: Percent of particles trapped (in gyrophase) as a function of final $(v_\parallel, \alpha_{eq})$ coordinates for three different wave amplitudes (60 pT,140 pT and 200 pT). As shown the percentage of particles trapped increases with wave amplitude. As shown the percentage of particles trapped is high for $v_\parallel$ close to $v_{res}(z_{eq})$ and falls off at higher value of $v_\parallel$; the larger amplitudes allow trapping over a larger portion of phase space. This is precisely because $S(z)$ is small close to the equator and the size of the trap is large; therefore, particles that come into resonance close to the equator have a higher probability of being trapped.
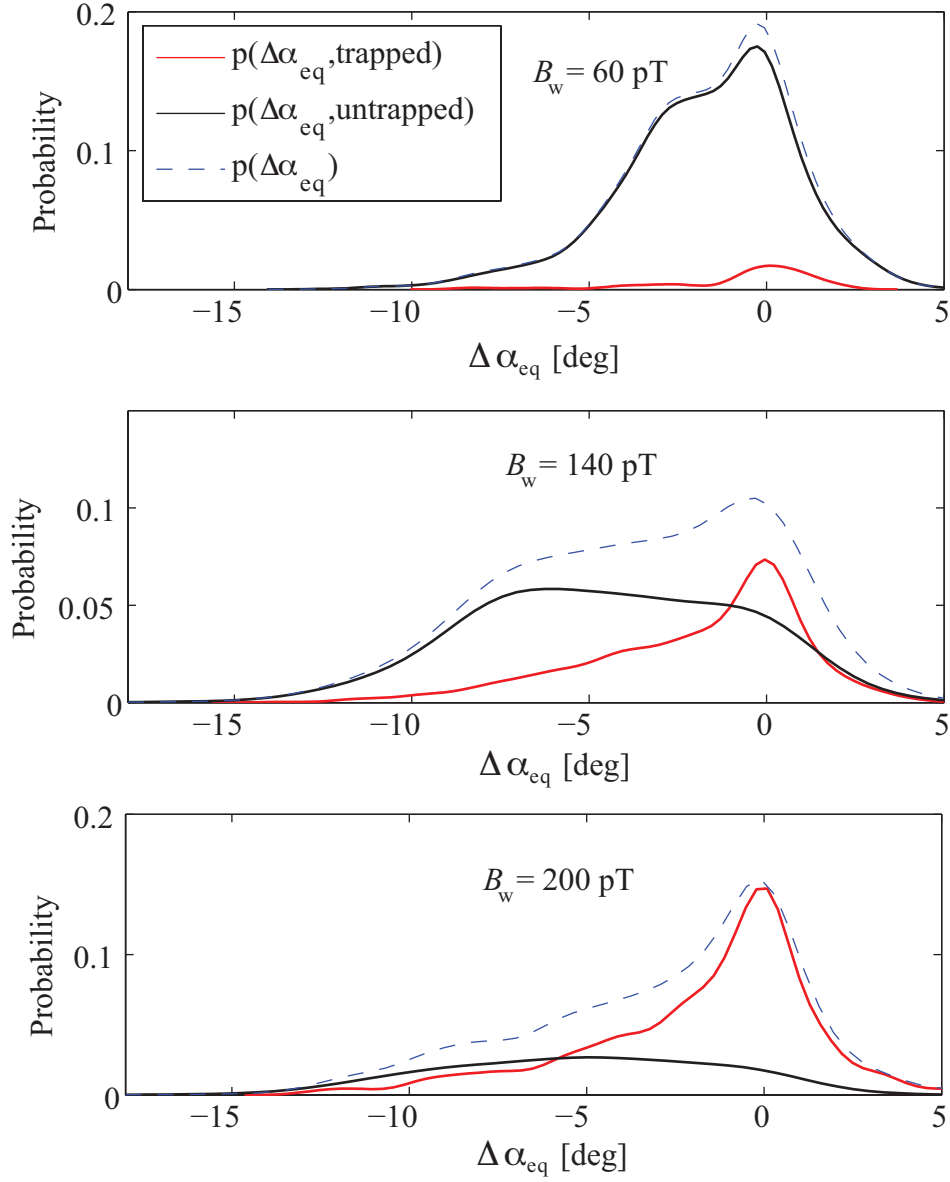
Figure 3.3: The probability distributions over $\Delta\alpha_{eq}$ for three wave amplitudes. At 60 pT, precipitation is completely dominated by untrapped particles. At 140 pT and 200 pT, there is a visible contribution due to the trapped population. As shown, the effect of phase trapping becomes increasingly important as the wave amplitude is increased and can no longer be considered negligible for evaluating precipitation.

the nonlinear model depends on the initial particle distribution function (value of β). That is, the error due to the linear theory approximation can be mitigated depending on the shape of the initial distribution function. The same comparison can be done for the sin-alpha distribution, this is shown in Figure 3.5. In this particular case, we use $m = 2$ and vary γ_s ($\gamma_s = 1$, $\gamma_s = 3$, $\gamma_s = 10$). As shown in Figure 3.5, linear theory matches the VL model for low amplitudes just as with the bi-Maxwellian distribution. Additionally, the range of validity of linear theory once again depends on the initial distribution function (value of γ_s). A general behavior across all the initial distributions is that starting at low amplitudes, the precipitated flux increases with amplitude until a local maximum is reached around $130-140$ pT. The flux subsequently decreases for larger amplitudes. Since phase trapping becomes more important at these large amplitudes (as described in the previous section), the decrease in precipitated flux is likely due to the nonlinear contribution of phase trapped particles.

The strength of the VL model is that only the characteristics are tracked, therefore, the initial particle distribution can be arbitrarily specified after the simulation is run. That is, the VL model creates a database of mappings from the exit phase-space grid to the initial phase-space coordinates. The precipitated flux due to different particle distributions is computed a posteriori. As the results show, the precipitated flux depends strongly on the initial particle distribution.

3.2.3   Time Evolution of Precipitated Flux

Another aspect of coherent wave particle interactions that has to date received little attention is the precipitated flux induced by short pulses. As mentioned previously, [49] and [20] used a semi-Vlasov model to compute the precipitated fluxes for short pulses. However, their method saved on computational effort by assuming a perturbed distribution function that is uniformly distributed in gyrophase. The VL model used in the present study solves the Vlasov equation and retains the gyrophase dependence.

In the previous sections, only the case of a constant wave amplitude filling the space (CW signal) was discussed. The VL model can also be used to calculate the precipitated flux as a function of time due to short pulses. Specifically, one side of the interaction region is illuminated with the input signal (boundary condition), and the wave then propagates through the interaction region. For each time step, the VL model can be used to trace the system back to time zero and subsequently evaluate the precipitated flux. As mentioned in Section 3.1, the "entrance" of the interaction region is specified with a fixed boundary condition for the phase space particle distribution. This basically assumes that fresh particles continuously stream into the interaction region. This assumption is valid over time scales for which the initial distribution function is not perturbed significantly. Future iterations of the model can include a time varying boundary condition to capture the long term evolution of the particle distribution function, however, that is beyond the scope of the present study. The VL model can accurately be used to model precipitation due to short pulses since the aforementioned assumptions will be valid.
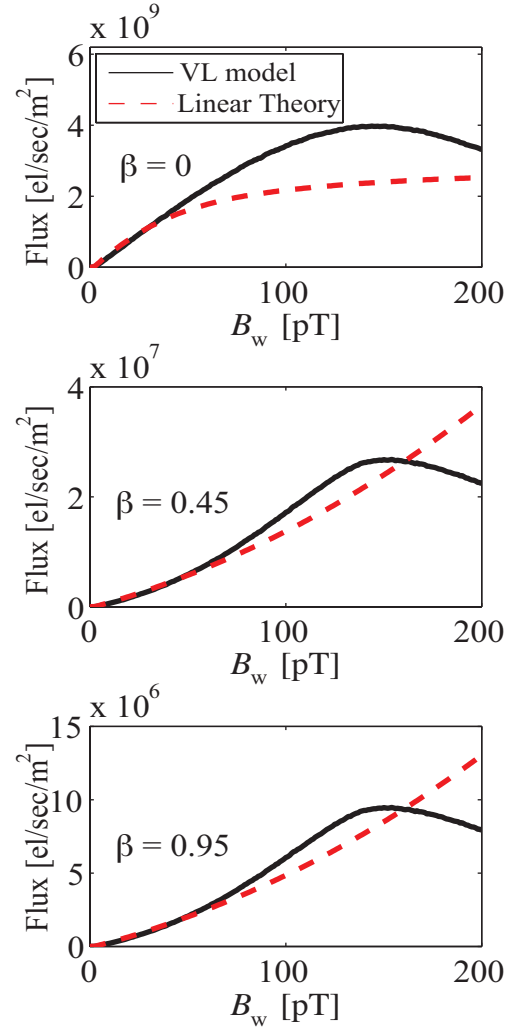
Figure 3.4: The dependence of precipitated flux on wave amplitude for three different values of β (bi-Maxwellian loss cone parameter). The comparison to linear scattering theory is shown as dashed red curves. As shown, the fluxes due to linear theory and the VL model are similar for small amplitudes; however, as the wave amplitude is increased, the fluxes due linear theory deviate from the full nonlinear model. As shown, the amplitude at which this deviation occurs depends on the initial particle distribution function (parameterized by β).
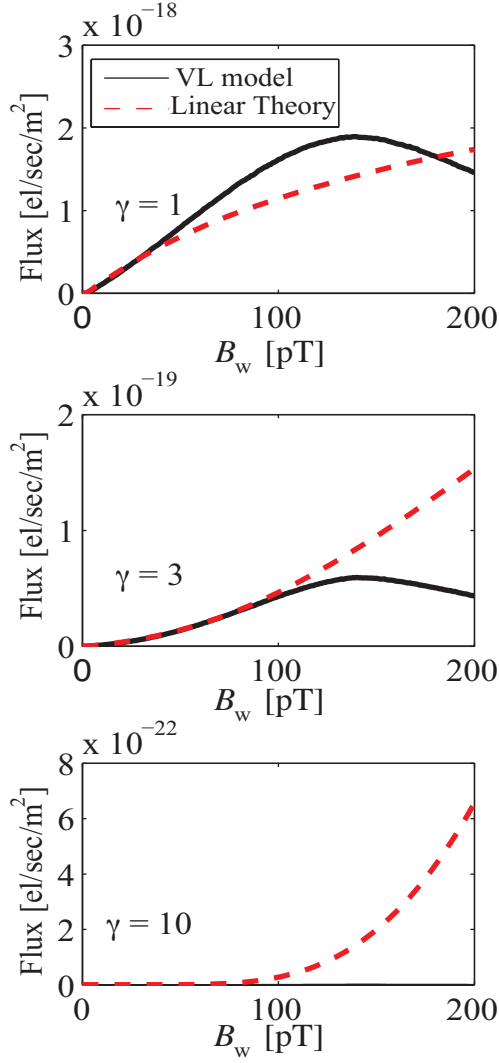
Figure 3.5: The dependence of precipitated flux on wave amplitude for three different values of γ_s (sin-alpha distribution parameter). The parameter m for the sin-alpha distribution is set to $m = 2$. The comparison to linear scattering theory is shown as dashed red curves. As with the bi-Maxwellian distributions, the fluxes due to linear theory and the VL model are similar for small amplitudes. Once again, the accuracy of linear theory in calculating the precipitated flux depends on the shape of the initial particle distribution (parameterized by γ_s).

To demonstrate the ability of the VL model to compute the time dependent precipitated flux, we consider 0.5 second input wave pulses. Additionally, different frequency-time sweep rates (fallers and risers) are considered to resemble signal formats used during the Siple Station wave injection experiment [40]. Rising and falling tones can also closely resemble free running triggered emissions and discrete chorus elements. The precipitated flux due to short pulses can be complicated since the finite sized wave packet fills only part of the interaction region. Therefore the range of resonant velocities available to interact with the wave changes as a function of time. Figure 3.6 shows the spatial profile of the wave at three different times as well as the range of resonance velocities available for interaction (shown in red). As shown, at $t = 0.399$ sec, the wave has partially filled the interaction region, however, since the resonance velocity curve is much steeper away from the equator, a significant range of velocities are resonant with the wave. At $t = 0.799$ sec, the entire wave packet is within the interaction region and is located near the equator. Close to the equator the resonance velocity curve is flatter since the inhomogeneity of the background geomagnetic field is small. Consequently, a much smaller range of velocities are available for interaction near the equator. At $t = 1.0667$ sec, the wave starts to leave the simulation space and once again has a larger range of resonant velocities available for interaction.

This pattern of a large range of available resonance velocities followed by a small range and then large again is reflected in Figure 3.7. Figure 3.7 (b) shows the normalized input wave signal as a function of time (0.5 second pulse). Figure 3.7 (a) shows the precipitated energy flux as a function of time due to the pulse for five different wave amplitudes. As shown there are two peaks in the precipitate energy flux profile (the first at around 0.5 seconds and the second at approximately 1.4 seconds). This is due to the different ranges of resonance velocities available for interaction at different times, as discussed earlier. Additionally, the precipitated flux responds for approximately 1.8 seconds even though the wave pulse was only 0.5 seconds long. After the particle interacts with the wave, there is a finite time delay before the particle reaches the exit of the simulation space (where precipitation is measured). For instance a particle in resonance velocity curve at high values of v_{res} inherently has a higher $v_{\parallel}$ than a particle that intersects the resonance velocity curve close to the equator. As shown in Figure 3.6, the maximum and minimum resonance velocities in the simulation space differ by a factor of two. Thus the two different particles will the reach the exit of the interaction region at different times. This adds to the extended response time of the precipitated flux and illustrates the added complexity of the problem.

Figures 3.6 and 3.7 have only considered a relatively high cold plasma density (400 el/cm^3). At high cold plasma densities, the wave group velocity is small which makes the length of the wave packet much smaller, thus the wave never completely fills the simulation space. At lower cold plasma densities the group velocity is higher and the wave packet will simultaneously fill a larger physical region for the same 0.5 second duration input pulse. This is demonstrated in Figure 3.8. In this lower cold plasma density case (50 el/cm^3), the group velocity is higher and the wave packet can fill
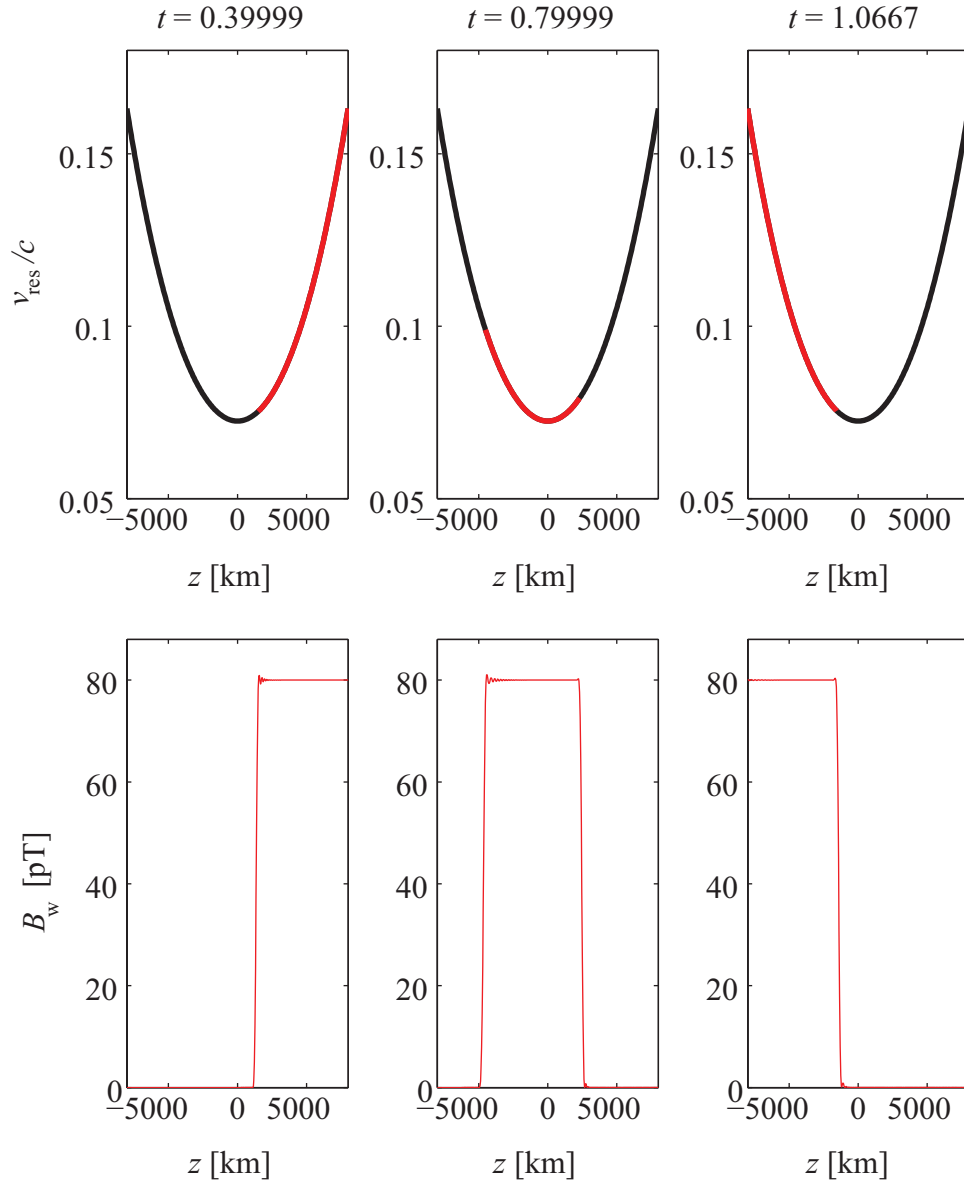
Figure 3.6: Range of resonance velocities interacting with the wave for $N_c = 400$ el/cm^3 as well as the spatial profile of the wave packet at three different times. Away from the equator, the wave packet can interact with a large range of resonance velocities while only a small range of resonance velocities are available for interaction near the equator. As shown, this effect is due to the shape of the resonance curve.
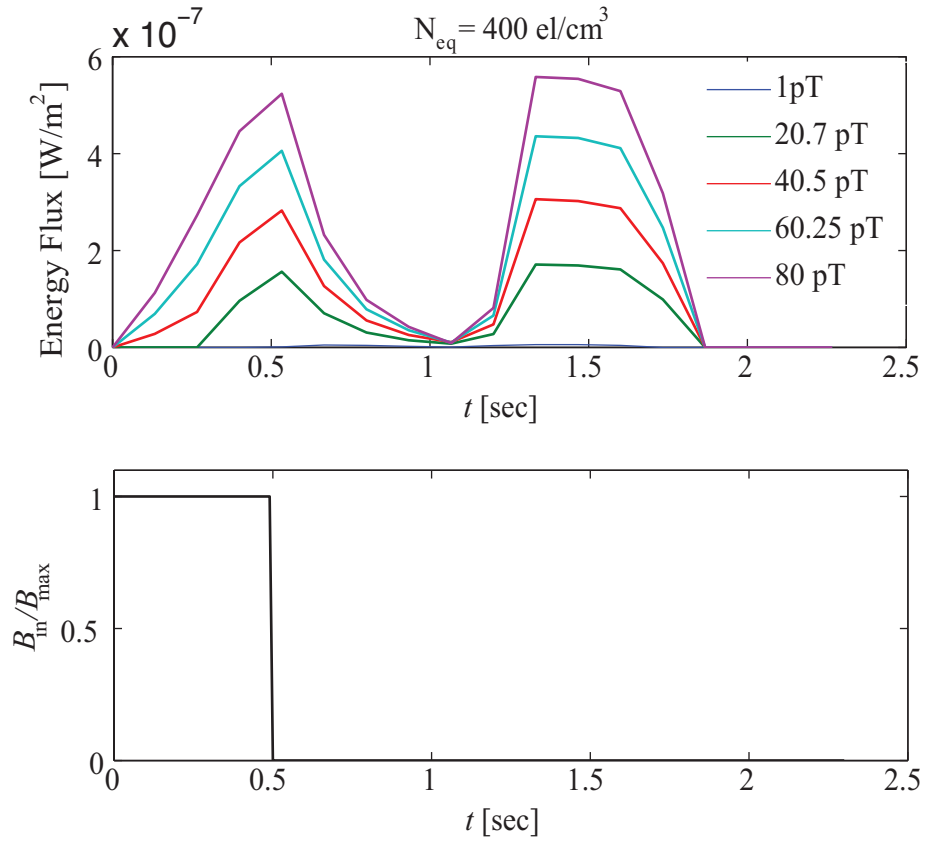
Figure 3.7: Precipitated energy flux as a function of time due to a 0.5 second pulse for $N_{eq} = 400$ el/cm^3 (over a range of wave amplitudes). Although the input wave pulse lasts 0.5 seconds, the response of the precipitated energy flux lasts approximately 1.8 seconds. This extended response time is due to the spread of velocities that can interact with the wave as well as the size of the wave packet within the interaction region (which depends on the input pulse length and group velocity).

the entire simulation space ($t = 0.4$ sec). Unlike the high density case, the largest range of resonance velocities are available for interaction once the wave has filled the entire simulation space.

In the low density case, two peaks in the precipitated energy flux as a function of time are not expected and only one maximum should occur when the wave fills the space. This is evident in Figure 3.9. Figure 3.9 (a) shows the precipitated energy flux as a function of time due to the 0.5 second input pulse for five different wave amplitudes ($N_{eq} = 50$ el/cm^3). As expected, there is only one maximum in the precipitated energy flux profile which occurs at around $t = 0.55$ seconds. Additionally, the flux response lasts for approximately 1.05 seconds. This is less than the high density case for multiple reasons. Since the wave frequency was kept the same as the high density case, the resonance velocities are much higher for the low cold plasma density case as shown in Figure 3.8. Thus the particles cross the interaction region much faster than in the high density case which decreases the time delay. The higher group velocity means that the wave will cross the interaction region much faster which also decreases the response time of the precipitated flux.

These results demonstrate the complex nature of the problem when considering precipitation induced by short pulses and is relevant to active experiments with short pulses [52]. As shown, the VL model is well suited to simulate the physics of wave-particle interactions and can be extended to input pulses with a time varying frequency (specifically rising and falling tones). That is, we consider signals with format $f(t) = f_0 + a_r t$ where f_0 is the initial wave frequency and a_r is the frequency sweep rate in Hz/sec (angular acceleration). All simulations use $f_0 = 4.5$ kHz while a_r varies from -2 to $+2$ kHz/sec. Figure 3.10 (a) shows the precipitated energy flux for falling tones (-2 kHz/sec). Figure 3.10 (b) shows monochromatic pulses while Figure 3.10 (c) shows the energy flux for rising tones ($+2$ kHz/sec). All three cases use $N_c = 400$ el/cm^3. As shown, the qualitative temporal profiles are similar for all three cases. The value of the precipitated energy flux is highest for the falling frequency case since the falling tone is composed of the lowest frequencies and consequently interacts with higher resonant energies. The purpose of Figure 3.10 is to demonstrate the ability of the VL model to simulate precipitation induced by coherent waves of changing frequency. Note that an additional equation apart from Equation (3.3) is required to propagate the changing frequency signal. For the present study, we used the following approximate wave equation:

$$\frac{\partial \omega}{\partial t} - v_g \frac{\partial \omega}{\partial z} = 0 \tag{3.7}$$

Equation (3.7) has only been used for computational simplicity and can be replaced by Maxwell's Equations if necessary.

3.3   Summary and Discussion

In this report we have addressed multiple questions regarding precipitation by coherent signals using a novel Vlasov-Liouville numerical model. We considered the effect of phase trapping on
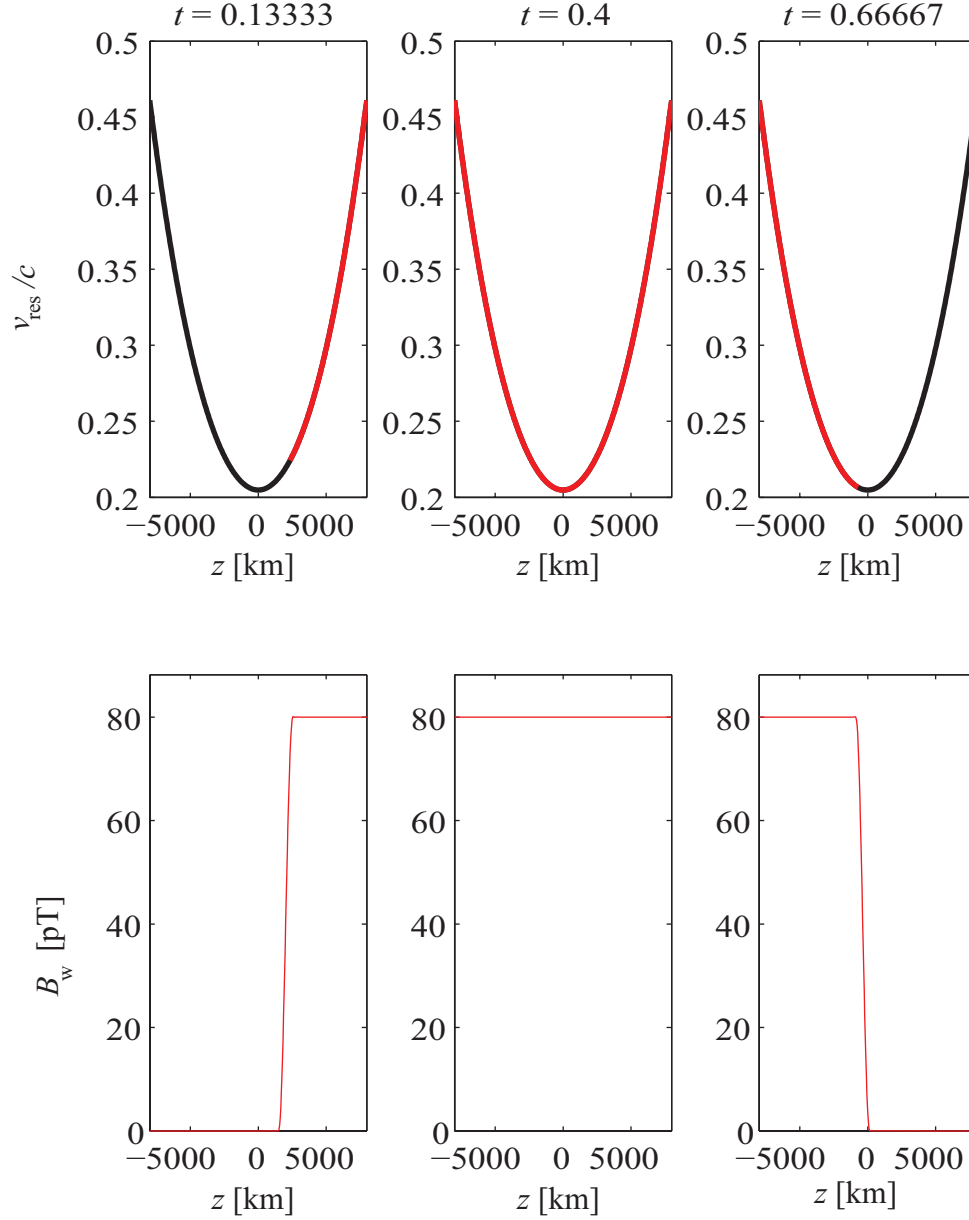
Figure 3.8: Range of resonance velocities interacting with the wave for $N_c = 50$ el/cm^3 as well as the spatial profile of the wave packet at three different times. At this cold plasma density, the group velocity is large enough that the wave packet can fill the entire simulation space ($t = 0.4$ sec) unlike the case of the higher plasma density.
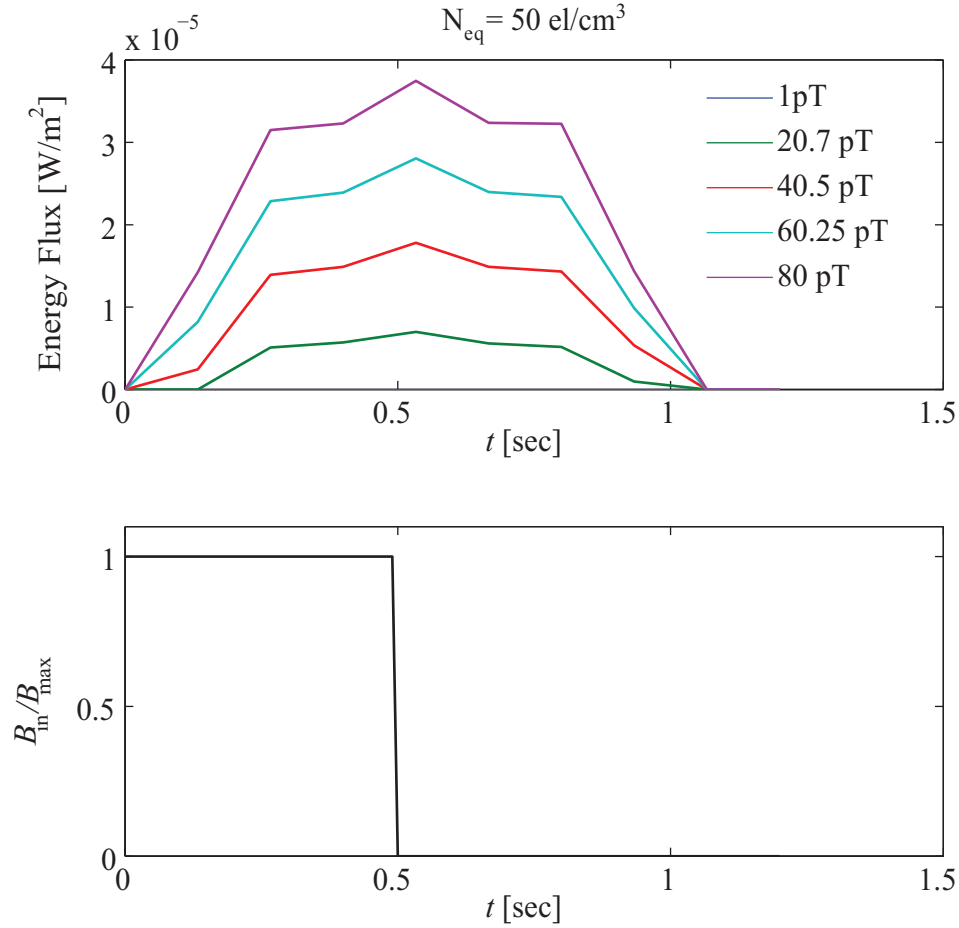
Figure 3.9: Precipitated energy flux as a function of time due to a 0.5 second pulse for $N_{eq} = 50$ el/cm^3 (over a range of wave amplitudes). Although the input wave pulse lasts 0.5 seconds, the response of the precipitated energy flux lasts approximately 1.05 seconds. This extended response time is due to the spread of velocities that can interact with the wave as well as the size of the wave packet within the interaction region (which depends on the input pulse length and group velocity).
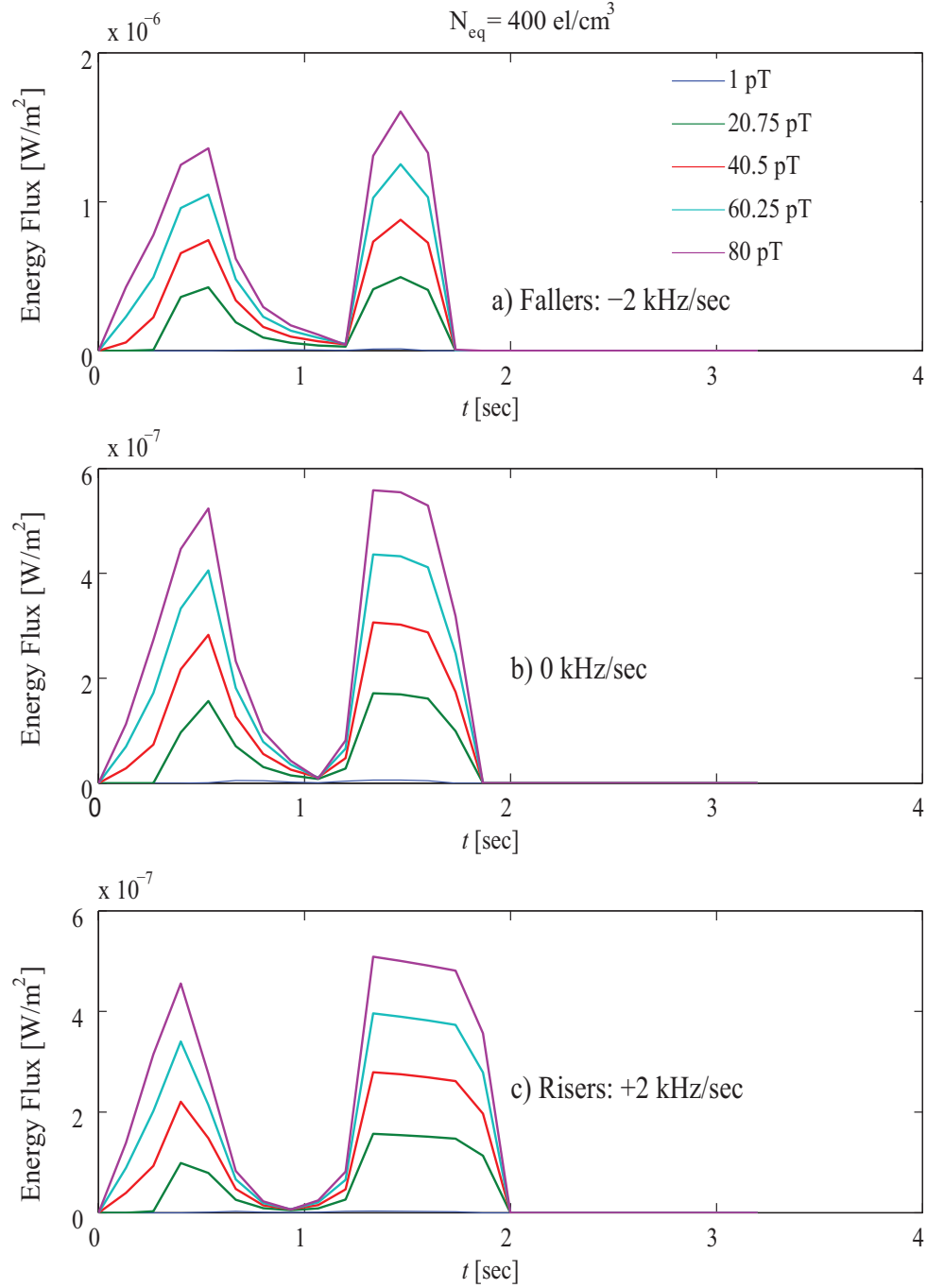
Figure 3.10: Precipitated energy flux as a function of time due to a 0.5 second pulses with different frequency sweep rates ($N_{eq} = 400$ el/cm^3). The temporal profiles of all three cases are qualitatively similar. As shown, the falling tone induces the highest precipitated energy flux since the lower frequency components interact with higher resonant energies.

precipitation. Using the VL model, we computed the probability distribution over pitch angle change for precipitated particles. The results show that phase trapping becomes an important effect as the wave amplitude is increased to large values ($>$ 100 pT). The precipitated flux predicted by linear scattering theory was compared to the VL model as a function of wave amplitude (for various hot plasma distributions). Linear scattering theory was shown to be valid for small wave amplitudes ($<$ 40-60 pT), however, the point of deviation of linear theory from the nonlinear model (when computing the precipitated flux) depends strongly on the initial hot plasma distribution function.

Finally, the ability of the VL model to simulate precipitation induced by 0.5 second pulses with changing frequency was demonstrated. The complicated temporal response of the precipitated flux suggests that maximizing precipitation may require a nontrivial input wave format. Formally, finding the ideal input wave format would require a solution to a PDE constrained optimization problem. That is, the problem would be to maximize the integrated precipitated flux subject to the Vlasov equation, wave equations, and any other practical constraints (such as amplitude limit, sweep rate limit, etc.). The optimum wave format can be selected by using the appropriate optimization methods. For known cold plasma parameters and a known background field, the general optimization problem is difficult but is potentially solvable with modern computational tools. The theoretical and numerical analysis presented in this report can be used as a stepping stone towards optimizing controlled particle precipitation and analyzing nonlinear wave particle interactions.

Chapter 4

Wave Growth Modeling

In the previous chapter, we utilized a numerical model that calculates the precipitated electron flux induced by coherent whistler mode waves. Although the model is quite useful at evaluating precipitation, it requires specifying the wave fields a priori. The precipitation model was thus not able to reproduce the effect of the particles on the wave amplitude and phase. As discussed previously, quantifying self-consistent wave amplification in the nonlinear regime is not feasible with analytical techniques making accurate numerical modeling indispensable. In this chapter, we present a novel numerical scheme for modeling wave amplification in the Earth's radiation belts.

4.1 Wave Growth Models

Analytical and numerical modeling of coherent particle interactions with coherent waves has been addressed by several authors [10, 56, 68, 44, 7, 36]. We first discuss selected models used by previous authors to describe nonlinear wave amplification in the Earth's radiation belts before presenting the numerical scheme that is employed in this report.

Consistent-Wave Model

One of the earliest theories on triggered emissions is the so-called "consistent-wave" model proposed by Helliwell [37]. In this model it was assumed that the Doppler-shifted wave frequency and the spatial variation of the gyrofrequency should be matched during the triggered emission process. More specifically, the resonance condition, $v_\parallel = \dfrac{\omega_c - \omega}{k}$, is assumed to be satisfied to yield the following condition for the wave frequency $\omega = \omega_c \dfrac{v_p}{v_p + v_\parallel}$. Here v_p and $v_\parallel$ are the wave phase velocity and particle parallel velocity, respectively. The quantity $v_\parallel$ is assumed to vary according to adiabatic motion. In other words, the wave frequency will change such that the adiabatic trajectory is tangent to the resonant velocity curve. Under these assumptions, the frequency as a function of time can

then be determined. The wave amplitude is then estimated by assuming all relevant particles will bunch while in resonance and the bunching time, $T_b = T_{\text{tr}}/2$ (where T_{tr} is the trapping period), is set equal to the resonance time $\dfrac{L_{\text{IR}}}{v_{\parallel}}$ where L_{IR} is the length of the interaction region. The model was able to predict the variety of frequency-time structures seen in the data (risers, fallers, hooks, etc.), however, the theory was still phenomenological and had no rigorous basis in plasma physics. Concepts such as phase-trapping and linear growth were essentially neglected in constructing the model and is hence not considered a robust theory of triggered emissions. Nevertheless, Helliwell's "consistent-wave" theory paved the way for several more sophisticated numerical models of wave amplification in the Earth's radiation belts.

Sheet Current Model

The model developed by Helliwell and Crystal [41] is referred to as the "sheet current" model or equivalently the "end-fire antenna" model. In this model, the interaction is assumed to take place in a small region around the equator. Several transverse current "sheets" are then spaced equally along the field line where each sheet consists of twelve sub-sheets. That is, when the simulation is initialized, each current sheet is initialized with twelve particles that are uniformly spaced in gyro-phase such that the total current is initially zero. The sheets (or particles) are mono-energetic and are initialized to the same pitch angle of 30 degrees. It is assumed that the particles' perpendicular velocities and pitch angles do not change during the interaction and the gryophase angle is the only quantity that is tracked in time. When the simulations begins, each particle is moved forward according to Equation (2.25), however, since the interaction region is assumed to be localized around the equator and the inhomogeneity is thus neglected (S = 0) in the equation of motion. As the gyro-phases advance in time and the particles moves along the field line, the total transverse current is calculated by summing the currents from each sub-sheet (particle). Once the current is calculated, the stimulated fields are then determined by treating the current as an end-fire antenna source. The total wave field is then updated by adding the stimulated fields the input fields at each time step. The model was able to reproduce nonlinear growth and saturation that was consistent with observations. The model was later updated by [14] to include the inhomogeneity in the equations of motion and to improve the resolution of the simulations. Once again, nonlinear growth and saturation took place, however, a linearly increasing frequency in time was also observed at the output and was suggested to be a product of the inhomogeneity. The primary limitation of this model is that although the wave fields can be determine easily, examining the evolution of the particle distribution function itself can be difficult to do.

Resonant Current Model

The resonant current model was first presented in [68]. In this model, it is assumed that trapped resonant electrons dominate the resonant current integral. The resonant current integral is simplified

under the assumption of a smoothly-varying particle distribution function to depend only on the
kinetic energy change of resonant electrons. Several particles are initialized with parallel velocities in
a sliver centered around the resonance velocity and gyro phases distributed uniformly. The particle
trajectories are integrated backwards to determine the energy change and subsequently update the
current integral. This model is similar in many ways to the sheet current model, however, the
wave amplitude update equations are derived more rigorously from Maxwell's Equations (along
with a narrowband assumption) by treating the background cold plasma as a fluid. The model was
able to demonstrate nonlinear growth and even triggered rising emissions, but with some difficulty.
The primary contribution of this model was that it demonstrated the dominating effect of trapped
resonant electrons on the triggered emission instability.

4.1.1   Particle Methods

Particle-in-cell (PIC) methods solve the Vlasov equation by using a large number of "super-particles"
and are used extensively in space plasma physics. In PIC methods, the initial particle distribution
function is randomly sampled with N super-particles while the initial electric ($\mathbf{E}$) and magnetic ($\mathbf{B}$)
fields are specified on a fixed spatial grid. The particle trajectories, or equivalently the characteristic
curves of the Vlasov equation, are then tracked continuously through time. At each time step, the
current ($\mathbf{J}$) and charge distribution (ρ) are calculated on the fixed grid by giving each super-particle
a shape and size (square, triangle, bell, etc.). Once, the currents and charges are computed, the
fields are updated using Maxwell's Equations and the algorithm continues in the same manner.
The specific Maxwell solvers and particle pushers used may vary from author to author, however,
the aforementioned outline serves as the foundation for all PIC simulations. PIC simulations have
been successfully used to model rising tone triggered emissions as well as discrete chorus emissions
[53, 54, 77, 44, 45].

Hybrid Particle Models

In hybrid particle models, the hot plasma electrons are tracked with super-particles, however, the
cold plasma is treated as a background fluid instead of individual particles. This allows for the wave
propagation to be determined by the cold fluid while the wave growth is directed by the hot plasma
super-particles. In [53] a hybrid-particle code was utilized and it was found that triggering of a
rising tone occurs at the back end of the input signal close to the magnetic equator and the resonant
current formation by untrapped electrons plays an important role in the triggering process. Using
the same simulation procedure, Omura et al [77] showed that chorus elements with rising tones are
generated close to the magnetic equator and undergo further nonlinear growth while propagating
away while the wave frequency remains essentially unchanged.

Full Particle Models

In full particle methods, both the energetic radiation belt electrons as well as the cold plasma electrons are tracked with particles in the PIC framework. More recently, a full particle code with no approximations to Maxwell's Equations was used to simulate rising tone emissions [44]. A monochromatic signal injected at the magnetic equator was shown to trigger a rising emission. The triggering signal created a depletion of electrons at the resonant velocity while the electrons exiting the wave trap generated a new wave rising in frequency. Although PIC simulations have been extremely successful at modeling wave-particle interactions in the radiation belts, the primary concern is including enough particles to accurately sample phase-space such that all the physically relevant particles are taken into account (i.e. electrons close to resonance). Since the noise in PIC simulations decreases as $O(\frac{1}{\sqrt{N}})$ [24], this often requires spending computational resources on a large number of particles that may not contribute significantly to wave growth.

4.1.2   Eulerian Methods

Eulerian methods have also been used to model the coherent wave instability by solving the Vlasov equation directly on a grid in phase space [23]. Several techniques have been proposed for solving the Vlasov equation, however, most applications include a coupling to Poisson's equation as a simplification to Maxwell's Equations [23, 67, 94]. There are many different methodologies that can be employed, the most common of which include: semi-Lagrangian methods, finite volume methods, finite difference methods, finite element methods, spectral methods and various combinations and modifications of each. We briefly describe the prominent numerical methods which have been utilized for investigating the whistler mode coherent wave instability.

Semi-Lagrangian

Semi-Lagrangian (SL) methods make use of Liouville's theorem to reconstruct the distribution function at each time step. The method works by first constructing a grid in phase-space and then tracing the particle trajectories from these grid points. Since the distribution function is conserved along particle trajectories (Liouville's theorem), it then reconstructed at the original grid points by interpolating from the particle locations. Since the scheme uses both an Eulerian frame (fixed phase-space grid) and traces particles (Lagrangian frame), it is termed the "semi-Lagragnian" method. Several modifications of the SL scheme have been proposed in the literature [85, 21, 23]. For instance, [29] also used a Vlasov hybrid technique to simulate nonlinear growth using a backward semi-lagrangian procedure such that the particle trajectories were restarted at each time step. The model was able to produce nonlinear growth as well as saturation of the wave amplitude; however, the scheme is quite sensitive to the phase-space grid spacings, and it can be difficult to isolate physical effects from numerical concerns.

VHS code

The VHS code, as described in [70], has been successfully used to model the dynamic spectra of VLF triggered emissions. In this technique, single particle trajectories are traced continuously through time while the distribution function is obtained by interpolating onto a phase-space grid at each time step. Once the distribution function is known, the resonant currents are calculated (with no approximations) and used to determine the wave fields. The VHS code has the advantage of having a dynamic number of simulation particles and hence does not suffer from the large number of particles required in PIC methods. The VHS code has been used to model rising, falling as well as hook like emissions [71], however, rising emissions are most commonly observed in the simulations [74]. The code has been employed in several studies over the past few decades. Nunn [76] simulated whistler-triggered emissions using the VHS code and demonstrated both rising and falling tones triggered in good agreement with observations. Nunn et al. [75] considered a parametric study of the VHS code over a range of simulation parameters. It was found that low input amplitudes generated fallers, intermediate amplitudes generated risers while large amplitudes generated fallers, hooks or oscillating tones. The frequency sweep rate was shown to be most sensitive to the cold plasma density with lower densities giving higher sweep rates. Nunna and Omura [73] modified the VHS code by restricting the interaction region to be only upstream of the equator where the inhomogeneity is positive. With the modification, the VHS code produced stable falling tones with the resonant particle trap showing an enhanced distribution function (hill) in contrast to a depletion caused by a rising emission. The component of the resonant current parallel to wave magnetic field was shown to be positive for falling tones while it is negative for rising tones. Although the VHS code has been used to simulate various aspects of triggered emissions, phenomena such as saturation and multi-wave interactions are difficult to reproduce with this model. Additionally, the artificial filtering required to keep the simulation stable may unintentionally eliminate physical effects.

The Eulerian methods described so far are compatible with nonuniform phase space grids, which is a particularly useful feature since the resonance velocity varies significantly along the geomagnetic field line. The reason is that, although the distribution is determined in phase-space, the schemes are still characteristic based. The disadvantage is that one must be careful with interpolation to preserve higher order accuracy of the scheme.

4.1.3 Finite Differencing

As mentioned in the earlier sections, self-consistently addressing wave amplification in the radiation belts requires solving the Vlasov-Maxwell system of equations. The primary difficult lies in time integrating the Vlasov equation accurately since it requires solving a partial differential equation (PDE) over a four dimensional phase-space (1 position, 3 velocities). The focus of this section will be to present and utilize a finite difference scheme and subsequently obtain a numerical approximation to the Vlasov equation. Before presenting the numerical scheme used in our model, a general

discussion of finite differencing serves as an appropriate starting point.

In simple terms, partial differential equations are mathematical equations that relate a function and its partial derivatives. For instance, the Vlasov equation is a PDE that contains only first derivatives with respect to all the phase-space coordinates. The idea behind most numerical schemes for solving PDEs is to the obtain a discretized approximation to the problem that was originally on a continuous domain.

The basic principle behind using finite differencing to solve differential equations is quite straightforward, differential operators are replaced by difference operators. For instance, the time derivative of some function f given by $\frac{\partial f}{\partial t}$ can be approximated as $\frac{\partial f}{\partial t} \approx \frac{f(t + \Delta t) - f(t)}{\Delta t}$ which is referred to as the forward finite difference (FD) approximation (where Δt is the discretized time step). The forward difference operator is only one finite difference approximation out of an infinite selection and is said to be "first order accurate". The order of accuracy of a FD scheme dictates how fast the error between the actual derivative and the FD approximation goes to zero. This can be seen by expanding the forward difference approximation in a taylor series to obtain $\frac{f(t + \Delta t) - f(t)}{\Delta t} = \frac{\partial f}{\partial t} + O(\Delta t)$. Here, the term $O(\Delta t)$ gives the leading order "truncation error" and is first order accurate because the error term contains the first power of Δt. FD approximations can be made higher order accurate by appropriately constructing the difference. For instance, the central difference approximation is given by $\frac{f(t + \Delta t) - f(t - \Delta t)}{2\Delta t} = \frac{\partial f}{\partial t} + O(\Delta t^2)$ and is thus second order accurate. At first glance, it may seem that central differencing is always a better choice than forward difference because of the inherently higher order of accuracy. However, only the approximations to lone-standing derivatives have been discussed so far. When dealing with differential equations, selecting the appropriate FD approximation for each derivative is crucial for algorithm stability and is a subject of research in its own right. Since a comprehensive overview of FD schemes for arbitrary differential equations is out of the scope of this dissertation, we will focus on the model advection equation due it's similar mathematical structure to the Vlasov equation. Once the model advection equation has been discussed, a FD upwind scheme will be presented and subsequently utilized to solve the Vlasov equation.

4.1.4 Model Advection equation

Before addressing the Vlasov equation, it is useful exercise to first consider the so called 'linear advection' (LA) equation,

$$\frac{\partial f(t, z)}{\partial t} + v_a \frac{\partial f(t, z)}{\partial z} = 0 \tag{4.1}$$

Here, $f(t, z)$ is the quantity being advected and v_a is the advection velocity (a constant) in the z-direction. The linear advection equation has an analytical solution and is given by $f(t, z) = f_0(z - v_a t)$, where $f_0 = f(t = 0, z)$. In words, the LA equation simply states that any initial profile f_0 at $t = 0$ will "advect" or slide in the $+z$ direction at velocity v_a. A visual description of the
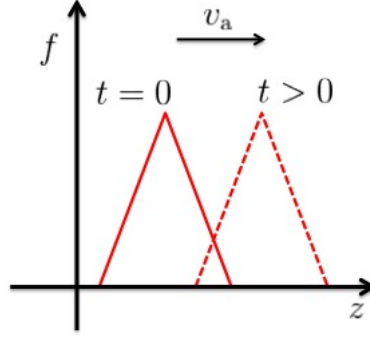
Figure 4.1: The advection of a triangular pulse at speed v_a based on the advection Equation (4.1).

solution to the LA advection equation is shown in Figure 4.1.

Although the LA equation has an analytical solution for a known initial spatial profile it is still fruitful to consider numerical approximations. The idea is that, anywhere on a phase-space grid, the Vlasov equation locally resembles the linear advection equation (and is multi-dimensional). Therefore a numerical method that can be used on the LA equation can be accordingly applied to the Vlasov equation as well. There are several techniques that can be utilized for the LA equation; however, the numerical scheme employed here is referred to as the first order "upwind scheme" and is detailed in the next section.

4.1.5   Upwind Finite Difference Model

To solve the Vlasov-Maxwell system, we employ a first order accurate linear upwind difference scheme which is diffusive but still provides a physically reasonable solution for a monochromatic input. The scheme works by appropriately discretizing the derivatives using forward or backward finite differencing depending on the direction in phase-space that particles stream from. Before using this scheme to solve the Vlasov equation, it is useful to first demonstrate how it works on the linear advection equation (since it is known to be stable for the LA equation). Specifically, the first order upwind scheme applied to (4.1) gives

$$f(t + \Delta t, z) = f(t, z) + \frac{v_a^+ \Delta t}{\Delta z}[f(t, z) - f(t, z - \Delta z)] + \frac{v_a^- \Delta t}{\Delta z}[f(t, z + \Delta z) - f(t, z)] \qquad (4.2)$$

where $v_a^+ = \max(v_a, 0)$ and $v_a^- = \min(v_a, 0)$. In simpler terms, the upwind scheme uses backward differencing, $\frac{\partial f}{\partial z} \approx f(z) - f(z - \Delta z)$, if $v_a > 0$ and uses forward differencing $\frac{\partial f}{\partial z} \approx f(z + \Delta z) - f(z)$ if $v_a < 0$. In other words, the finite difference approximation is taken in the direction that signal is coming from. Thus if v_a^+ is nonzero then v_a^- will be identically zero and vice-versa. It can

be shown that if the derivative is taken in the opposite direction, the algorithm will necessarily become unstable. The upwind scheme scheme is stable and works for the LA equation. The primary bottleneck of this scheme is that it is constrained by the Courant-Friedrichs-Lewy (CFL) condition, which states that signal can traverse at most one grid cell in one time step. This enforces that the numerical domain of dependence contains the analytical domain of dependence and is a necessary condition for numerical stability. Specifically, for the case of the LA equation, the CFL condition is given by $\Delta z < v_a \Delta t$.

In order to apply this algorithm to the Vlasov equation, the upwind scheme must updated to multiple dimensions. Additionally, the advection "speeds" are now more abstract as they represent speeds through phase-space. For instance, the "speed" through velocity-space is actually an acceleration in physical-space. Additionally, the advection speeds also vary as a function of the phase-space coordinates and can change from negative to positive depend on which direction in phase space a particle moves.

As mentioned before, the Vlasov equation (or equivalently Liouville's theorem) is given by $\frac{\partial f}{\partial t} + \sum_{i=1}^{n} \frac{dx_i}{dt} \frac{\partial f}{\partial x_i} = 0$ where x_i represents each component of the position and velocity of a particle. The terms $\frac{dx_i}{dt}$ then specify the advection speeds. After generalizing to multiple dimensions, the upwind scheme applied to the Vlasov equation can be compactly written as

$$f(t + \Delta t) = f(t) - \Delta t \left(\sum_{i=1}^{n} \frac{dx_i^+}{dt} D_i^- f + \frac{dx_i^-}{dt} D_i^+ f \right) \tag{4.3}$$

where $\frac{dx_i^+}{dt} = \max(\frac{dx_i}{dt}, 0)$ and $\frac{dx_i^-}{dt} = \min(\frac{dx_i}{dt}, 0)$. The quantities $D_i^- f$ and $D_i^+ f$ denote the backward and forward finite difference operators respectively. For the case of the Vlasov equation, the CFL condition is modified and is given by $\Delta t < C_{max}(\sum_{i=1}^{n} \frac{\frac{dx_i}{dt}}{\Delta x_i})^{-1}$, where Δx_i represent the phase-space grid spacings and C_{max} is generally a number less than 1. For the investigations described herein, C_{max} is set to 0.8 which is a conservative value. The time step is then selected using $\Delta t = C_{max}(\sum_{i=1}^{n} \frac{\frac{dx_i}{dt}}{\Delta x_i})^{-1}$. Since this quantity can change with every iteration, the time step is forced to change dynamically.

Since the waves in this simulation are coherent, the Vlasov equation can be coupled to the narrowband wave equations that also take the background cold plasma into account [68]. The Narrowband equations are shown in Equations (4.4) and (4.5) and are derived in Appendix A.

$$\frac{\partial B_w}{\partial t} - v_g \frac{\partial B_w}{\partial z} = -\frac{\mu_0 v_g}{2} J_E \tag{4.4}$$

$$\frac{\partial \phi_w}{\partial t} - v_g \frac{\partial \phi_w}{\partial z} = -\frac{\mu_0 v_g}{2} \frac{J_B}{B_w} \tag{4.5}$$
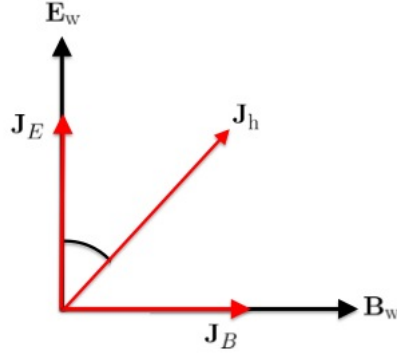
Figure 4.2: The components of the resonant current in the direction of the electric field (J_E) and magnetic field (J_B).

The quantities B_w and ϕ_w are the wave amplitude and phase of the modulating wave packet propagating in the $-z$ direction at the group velocity, v_{g}. J_E and J_B are components of the resonant current in the direction of the wave electric and magnetic fields, respectively. Since the single particle equations of motion require knowing the wave frequency and wavenumber at each time step, the wavenumber is updated using $k = k_0 + \dfrac{\partial \phi_w}{\partial z}$ and the wave frequency can be updated using $\omega = \omega_0 + \dfrac{\partial \phi_w}{\partial t}$. The time derivative can be removed with the help of Equation (4.5) to give $\omega = \omega_0 - \dfrac{\mu_0 v_{\text{g}}}{2} \dfrac{J_B}{B_w} + v_{\text{g}} \dfrac{\partial \phi_w}{\partial z}$. Here ω_0 and k_0 are the initial wave frequency and wavenumber and are given by the cold plasma dispersion relation.

The advantage of using the narrowband wave equations is that, for a coherent wave, both B_w and ϕ_w will be slowly varying functions of position (i.e $\dfrac{\partial}{\partial z} \ll k$) even if the quantity $B_w e^{i\phi_w}$ may be varying rapidly. Therefore, the number of spatial grid points can be much fewer than if the wave equations were solved in vector form. The disadvantage is that the phase evolution equation (Equation (4.5)) can become unstable for small wave amplitudes due to the B_w term in the denominator. However, for a zero order distribution function that is conducive to growth, the wave amplitude in our simulations was not observed to become small enough to be a concern for the simulations. For simulations with an arbitrary input signal (not monochromatic), solving the vectorized version of the wave equations along with more spatial grid points would be advantageous. Additionally, the narrowband equations provide useful physical intuition behind growth and frequency change. Specifically, wave growth or damping is only governed by the component of the current in the direction of the wave electric field, J_E. On the other hand, phase advance (or equivalently frequency change) can only take place if there is a component of the current in the direction of the wave magnetic field. Thus, these equations have the advantage of somewhat separating the effect of the wave growth and frequency change. The geometry of the currents with respect to the wave fields is shown in Figure 4.2.

Since the narrowband wave equations are also advective equations (with a source), they can also be solved with the same finite difference scheme used for the Vlasov equation. The wave equations are also constrained by a CFL condition and the time step that is the more restrictive (either for particles or wave) is selected for the simulations. It is also worth noting that no artificial filtering is required for stability of the algorithm. The primary difference between the upwind FD scheme and the numerical methods described previously (PIC, Semi-Lagrangian, VHS, etc.) is that the upwind scheme is not characteristic based; the Vlasov equation, in differential form, is discretized in the Eulerian frame.

4.2 Relativistic Coordinate Transformation

Finite difference (FD) schemes have the advantage of being easy to implement with the expense of requiring a uniform grid. For this reason, FD schemes have previously not been a method of choice for solving the Vlasov equation in an inhomogenous magnetic field. In this study, using a procedure similar to [69, 70], we present the transformation of the Vlasov equation into a resonance-subtracted coordinate system (including relativistic corrections) such that a uniform grid can be used in the new coordinate space. We leverage the coordinate transformation to complete the first successful numerical simulations of nonlinear amplitude growth of the coherent wave instability using the aforementioned upwind FD scheme.

The full six dimensional $(\mathbf{r}, \mathbf{v})$ Vlasov equation is computationally intensive, thus, several authors have used the reduced four dimensional Vlasov equation $(z, \mathbf{v})$ with the background inhomogeneity incorporated as a gradient term in the equations of motion as discussed in Chapter 2. Additionally, we make the assumption of parallel propagating waves which is a good approximation for ducted VLF signals [35]. For an injected VLF signal propagating in one direction along the field line, significant energy exchange occurs when particles at the local gyroresonance velocity v_{res}.

The problem in using a uniform phase space grid in parallel velocity is that the local resonance velocity changes significantly along the magnetic field line forcing coverage of a large range of parallel velocities. However, the scale at which resonant particles change in $v_\parallel$ is on the order of the trapping velocity, $v_{\mathrm{tr}} = (\dfrac{4qB_{\mathrm{w}}v_\perp}{mk})^{\frac{1}{2}}$, which is effectively the size of the trap in $v_\parallel$-space. Therefore, to resolve the fine scale features, $\Delta v_\parallel \sim v_{\mathrm{tr}}/10$ at the very least, where $\Delta v_\parallel$ is the grid spacing in the $v_\parallel$ coordinate. For a numerical interaction region of ± 5000 km at $L = 4$ and conservative background parameters, a uniform grid can require hundreds to thousands of points in parallel velocity with a large fraction of the grid not contributing to the simulated physics at any given point in space and time. This multi-scale nature of the problem is illustrated in Figure 4.3.

However, if the initial wave frequency of the injected signal is known, the resonance velocity (or equivalently resonant momentum) is a known function of z and $p_\perp$. The following simple coordinate transformation $\hat{p} = p_\parallel - p_{\mathrm{res}}(z, p_\perp)$ forces the local resonance condition to occur at $\hat{p} = 0$ where p_{res}
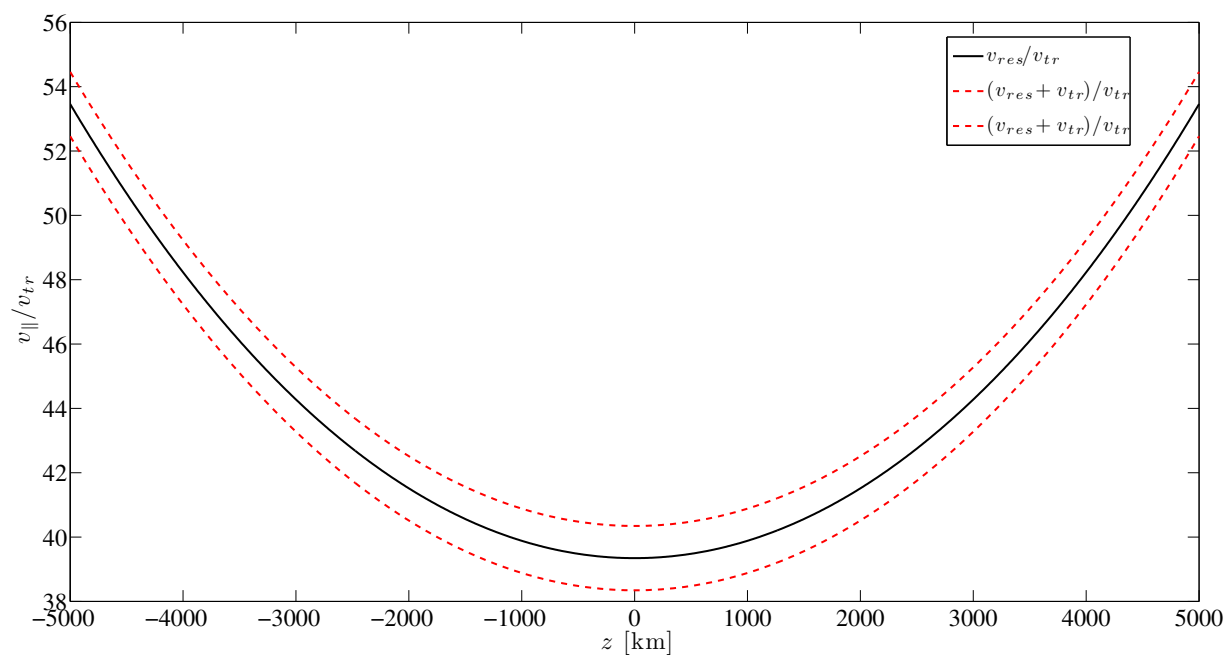
Figure 4.3: Resonance velocity curve along with bounds representing one trapping distance away from resonance. The multi-scale nature of the problem is shown with the full range of resonance velocities exceeding several trapping distances.

is the resonant momentum ($p_{\text{res}} = \gamma m v_{\text{res}}$). Here, $\gamma = (1 + \dfrac{p_\perp^2 + p_\parallel^2}{(mc)^2})$ is evaluated at $p_\parallel = p_{\text{res}}$ to give a quadratic equation $A p_{\text{res}}^2 + B p_{\text{res}} + C = 0$. The coefficients A,B and C are given in Equations $(4.6)-(4.8)$.

$$A = (\frac{k}{m\omega})^2 - (\frac{1}{mc})^2 \tag{4.6}$$

$$B = -\frac{2k\omega_{\text{c}}}{m\omega^2} \tag{4.7}$$

$$C = (\frac{\omega_{\text{c}}}{\omega})^2 - (\frac{p_\perp}{mc})^2 - 1 \tag{4.8}$$

The root that gives the non-relativistic resonance velocity in the limit $\gamma \sim 1$ is selected for the coordinate transformation. A visual description of the change in coordinates is shown in Figure 4.4. In canonical coordinates the Vlasov equation is given by,

$$\frac{\partial f}{\partial t} + \sum_{i=1}^{n} \frac{dx_i}{dt} \frac{\partial f}{\partial x_i} = 0 \tag{4.9}$$

The terms $\dfrac{dx_i}{dt}$ are governed by the single particle equations of motion (Lorentz force). The Vlasov equation can be readily transformed from one coordinate system to another ($x_i \rightarrow y_j$) using $\dfrac{dy_j}{dt} = \displaystyle\sum_{i=1}^{n} \dfrac{\partial y_j}{\partial x_i} \dfrac{dx_i}{dt}$ and substituting ($x_i \rightarrow y_j$) in Equation (4.9).

A significant amount of previous research has used a cylindrical coordinate system ($v_\parallel, v_\perp, \phi, z$) for the equations of motion [50, 22]. The new coordinates simply replace $p_\parallel$ with $\hat{p}$ to give ($\hat{p}, p_\perp, \phi, z$). Since p_{res} is only a function of z and $p_\perp$, the equation of motion becomes $\dfrac{d\hat{p}}{dt} = \dfrac{dp_\parallel}{dt} - \dfrac{dp_\perp}{dt} \dfrac{\partial p_{\text{res}}}{\partial p_\perp}$ $- v_\parallel \dfrac{\partial p_{\text{res}}}{\partial z}$. The terms $\dfrac{\partial p_{\text{res}}}{\partial p_\perp}$ and $\dfrac{\partial p_{\text{res}}}{\partial z}$ can be evaluated analytically or numerically. The Vlasov equation in the new coordinate system is then given by

$$\frac{\partial f}{\partial t} + (\frac{dz}{dt})\frac{\partial f}{\partial z} + (\frac{dp_\perp}{dt})\frac{\partial f}{\partial p_\perp} + (\frac{d\phi}{dt})\frac{\partial f}{\partial \phi} + (\frac{d\hat{p}}{dt})\frac{\partial f}{\partial \hat{p}} = 0 \tag{4.10}$$

4.3   Phase-Space Grid

Properly constructing the phase-space grid is vital for accurately simulating wave growth. Only particles within a few trapping velocities (v_{tr}) are relevant to wave growth. For a growing wave, however, the size of the trap changes as a function of position along the field line since v_{tr} is proportional to the square root of the wave amplitude. This poses a difficulty since the grid must be fine enough to resolve the smallest trap and large enough to include the largest trap. This tradeoff cannot be overcome without an adaptive grid, thus as a compromise, the average amplitude based on the linear theory prediction is used to determine the maximum size of the grid in velocity space
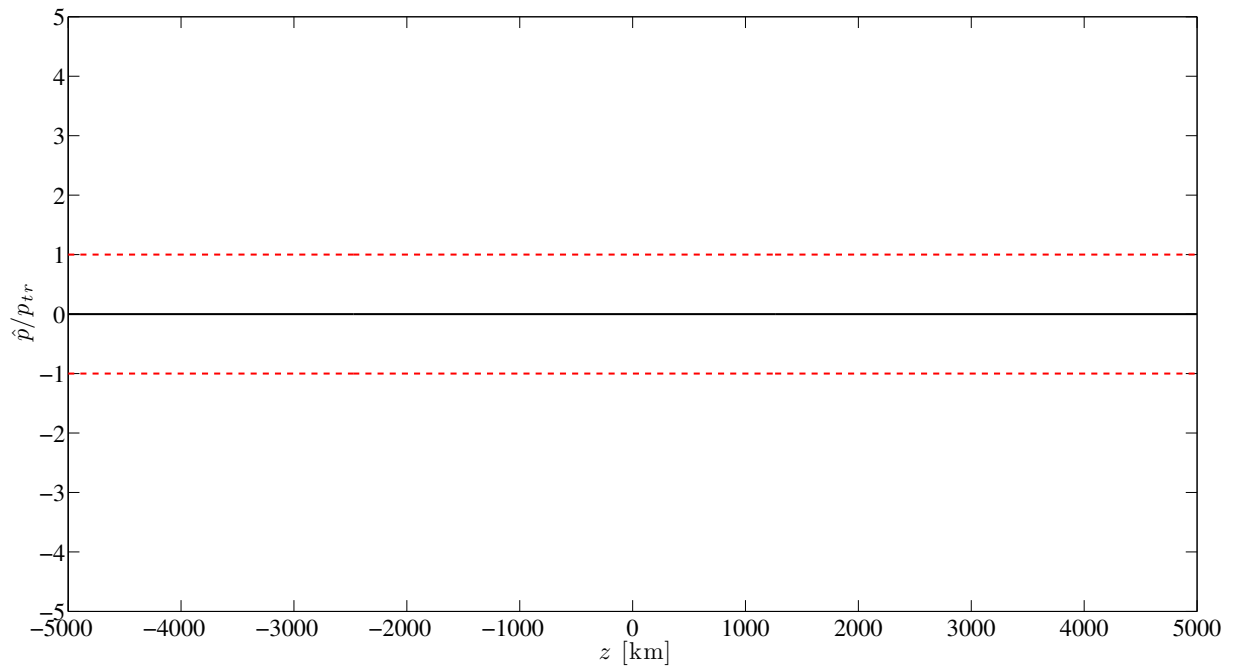
Figure 4.4: Representative gridlines after the relativistic coordinate transformation. Note the grid lines correspond to the same grid lines in Figure 4.3 and have been "flattened" out which gets around the multi-scale concern.

as well as the grid point spacing required to properly resolve the trap. Regions along the field line where the growth is purely linear (closer to the entrance boundary) do not have a trap which is why the average value, and not the smallest amplitude, is used to determine the number of grid points. The maximum amplitude predicted by linear theory is not used because, for extremely large linear growth rates, the nonlinear growth will in fact be much less than linear growth in order for amplitude saturation to occur. That is, linear theory imposes no bound on the maximum attainable growth even though the signal should saturate according to the full nonlinear model. Thus, using the prediction of linear theory would generate an extremely large grid in velocity space even when it is not necessary. For this reason, using approximately 100 grid points in velocity-space to resolve the "average amplitude trap" has been empirically determined to be a reasonable number for the simulations that will be described in this study.

The grid in $\hat{p}$ space ranges ± 5 trapping velocities around $\hat{p} = 0$ where the trapping velocity is evaluated at the average perpendicular momentum and at the average wave amplitude predicted by linear theory. This grid is large enough to accommodate approximately a ± 300 Hz change in the wave frequency and still contain the resonance velocity in the simulation space. A full grid is used in $p_\perp$ such that range of pitch angles in the simulations is between 20 and 80 degrees. Higher pitch angles complicate the simulation since the resonance velocity (with relativistic corrections) will be forced to decrease dramatically to ensure that the particle is not faster than the speed of light. Lower pitch angle particles (close to the loss cone) are not considered since they generally have low perpendicular velocities and hence do not contribute significantly to the resonant current.

Additionally, we use $N_{\hat{p}} \times N_{p_\perp} \times N_\phi \times N_z = 101 \times 24 \times 32 \times 400$ for a total of 31 million grid points. Increasing the number of grid points will provide a more accurate solution but at a large cost to computation due to the restrictive CFL condition.

4.4   Initial Particle Distribution

The hot plasma distribution function considered in the following simulations is a Bi-Maxwellian. This type of distribution was discussed briefly in the VL model section and has been used by other authors in the past [45]. For a distribution function of this form, the anisotropy is given by $A = \dfrac{T_\perp}{T_\parallel} - 1$, an expression which readily conveys the concept of anisotropy or directional dependence of the distribution. For a bi-Maxwellian, if the perpendicular and parallel temperatures are equal, the anisotropy is identically zero. Thus, waves are unstable to the plasma if the electron temperature is higher in the direction perpendicular to the magnetic field than parallel to it. For this reason, the term "temperature anisotropy" is used since it provides simple physical intuition behind why the waves are unstable.

4.5   Modeling Results

Since the objective of this study is to model wave amplification of injected coherent signals, we use parameters associated with the Siple Station wave injection experiment [39]. The input wave amplitude used in the simulation is $B_w = 100$ fT (-20 dB-pT). The initial amplitude filling the simulation space cannot be set to zero due to the B_w term in the denominator of Equation (4.5) and is initialized to 120 dB below the input wave amplitude. To examine the transition from linear to nonlinear growth, we consider three simulations conditions.

The first two simulations use the following background parameters: $L = 4$, $N_{\text{cold}} = 250$ el/cm^3, $f_0 = 1.5$ kHz. The hot plasma densities are $N_{\text{h}} = 0.02$ and 0.1 el/cm^3, respectively. The case with the lower hot plasma density results in purely linear growth while the higher density case results in nonlinear growth as will be detailed in following sections. For the third simulation we consider a hot plasma density of $N_{\text{h}} = 0.96$ el/cm^3 but, the L-shell is changed to $L = 4.2$. This case produces a large growth rate and also results in nonlinear growth, however, the majority of the growth takes place before the wave reaches the equator. All simulations use an input pulse duration of 0.5 seconds. The results of the simulations, along with a comparison to linear theory is described in detail in the following subsections.

4.5.1   Simulated Linear Growth

Linear growth is the prediction we expect from the solution to the linearized Vlasov-Maxwell system. Although the term "linear" is used, the growth is actually exponential in space, or equivalently linear on a log scale. As discussed in Chapter 2, linear theory is generally valid at lower wave amplitudes, however, since the growth is exponential, it may grow to large amplitudes and thereby violate the linearization assumption. Therefore, in order to compare the simulation results to linear theory, the hot plasma density is kept relatively low $N_{\text{h}} = .02$ el/cm^3 so that the growth rate will not be sufficient to bring the wave amplitude into the nonlinear regime.

Due to the inhomogeneity of the medium, the linear growth rate does change as a function of position (and drops off rapidly far away from the equator); however, the size of the simulation space is small enough that the change is negligible and the equatorial linear growth rate is used as a proxy. With this assumption, the linear theory prediction will indeed be a line when displayed on a log scale.

The comparison between linear theory and the simulation result is shown in Figure 4.5. Each of the six panels displays a snapshot of the wave amplitude spatial profile along with the prediction from linear theory. As shown in panels (a)−(c), the front end of the pulse traces the linear theory curve as it propagates along the field line. Since the pulse is 0.5 seconds in duration, the back end is not observed until panel (d) and up until this point, the wave profile is indistinguishable from a key-down (CW) signal. Once the back end of the pulse enters through the right hand boundary, the

Figure 4.5: Each subplot shows single snapshot in time of the wave amplitude spatial profile as it propagates through the simulation space. The wave amplitude, B_w from the simulation is shown by the blue solid curves. The prediction from linear theory is shown by the red dashed curve while the black dashed curve represents the minimum amplitude for phase trapping. In this simulation case, the growth rate is low and the wave amplitude never crosses the minimum amplitude for trapping resonant electrons. The growth is therefore in good agreement with linear theory and serves as validation for the model.

wave packet simply propagates through the simulation space in accordance with linear theory until it exits through the left boundary.

This simulation case is particularly important as it serves as a "test" condition to validate against a known analytical estimate to the Vlasov-Maxwell system given by linear theory. This particular result is of course repeatable as long as the wave amplitude is not large enough to exceed the trapping the threshold for a "significant" amount of time. As discussed previously, linear theory cannot explain several aspects of experimental data. In the following subsections, we consider cases where the growth rates are larger and consequently induce nonlinear wave amplification.

4.5.2 Simulation of Nonlinear Growth

To examine the growth of wave in the nonlinear regime, we consider hot plasma densities that are high enough to bring the wave amplitude up to the threshold for the trapping of resonant electrons. The simulations are discussed in detail in the following subsections.

Nonlinear Growth I

We first consider a hot plasma density, $N_h = 0.1$ el/cm^3 which is five times larger than the previous (linear growth) case. The simulation result is shown in Figure 4.6 along with the comparison to linear theory. As shown in panel (a) , the wave profile essentially follows that of linear theory when it first enters the simulation space and is far below the minimum amplitude for trapping. However, by $t = 0.42$ seconds, shown in panel (c), the wave amplitude has passed the threshold value required for phase-trapping resonant electrons and begins to deviate significantly from the linear theory prediction. The change in growth rate from linear to nonlinear growth is quite apparent. Although the front end of the waves grows relatively smoothly, oscillations in the wave amplitude start to develop close to the equator as seen in panel (d) and propagate away toward the exit as shown in (e). From the perspective of an observer at the output (i.e on the surface of the Earth), the wave is observed to exhibit a short duration of nonlinear growth followed by saturation. This is in agreement with observations from the Siple Station Experiment. Once the wave amplitude saturated at the output, the wiggles in the amplitude are then received (similar to the oscillations often seen after saturation in data). By $t = 1.24$ seconds, shown in panel (f), the back end of the wave is also received at the exit of the interaction region.

In this particular simulation, the front end of the wave grows quickly and stays high enough above the trapping threshold that the distribution inside the trap reaches a steady state leading to saturation of the wave amplitude. Closer to the equator, however, the wave amplitude stays very close to the trapping threshold. Since the amplitude is so close the threshold, several particles can be released from the trap as they counter-stream through the wave. The manner in which the particles are released depends strongly on their initial pitch angles, phase angles, and locations where they were initially trapped. The effect of de-trapping particles manifests itself in this case as oscillations
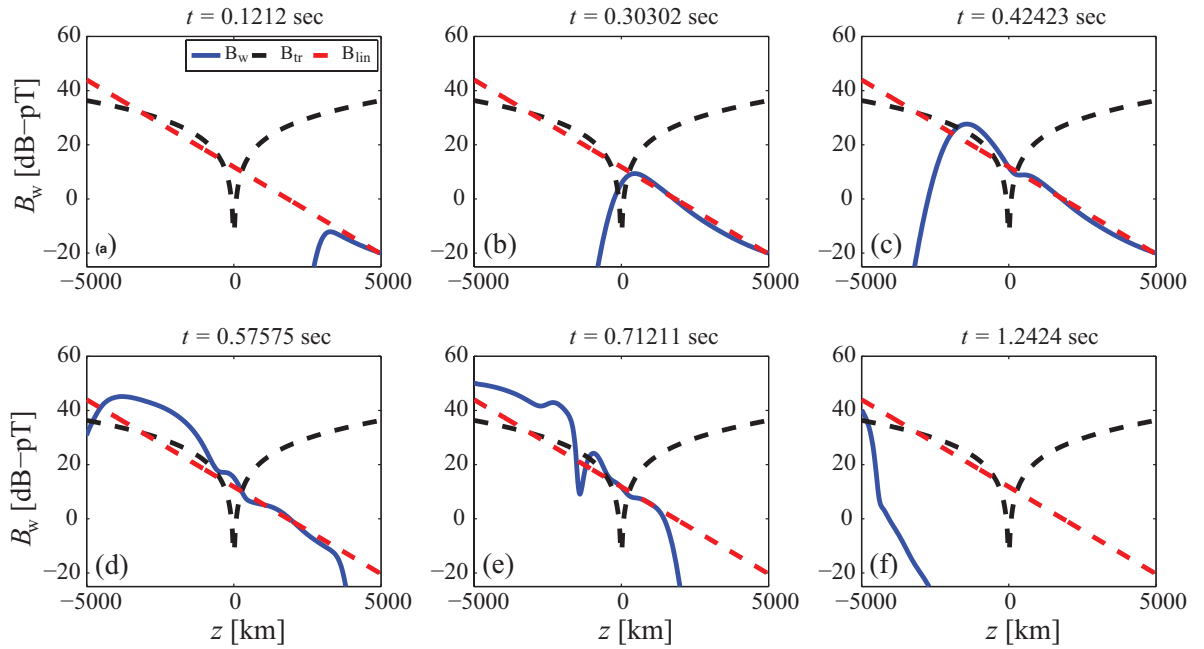
Figure 4.6: Result of a simulation with $N_h = 0.1$ el/cm^3. Each subplot shows single snapshot in time of the wave amplitude spatial profile as it propagates through the simulation space. In this case, the wave amplitude first follows the linear theory prediction as it propagates along the field line as shown in (a) and (b) . Once it crosses the trapping threshold close to the equator, the wave subsequently undergoes nonlinear growth with oscillations that propagate toward the receiver.

that propagate to the receiver side and are observed after saturation. Since the oscillations are likely due to de-trapping of resonant electrons in this "weakly" growing wave, the next simulation considers a much higher growth rate where the wave amplitude stays significantly above the trapping threshold.

Nonlinear Growth II

In this case, we consider a much larger hot plasma density, $N_{\mathrm{h}} = 0.96$ el/cm^3 which results in a significantly higher linear growth rate. The simulation result is shown in Figure 4.7 along with the comparison to linear theory. Once again, as shown in panel (a) , the wave amplitude first follows the linear theory prediction when it enters the simulation domain from the right hand boundary. As can be seen, the growth rate is much higher than the previous simulations and the linear theory prediction crosses the trapping threshold much before the equator (at approximately $z = 2000$ km). At $t = 0.27$ sec, shown in panel (b), the amplitude begins to pass the trapping threshold. Shown in panel (c) the wave amplitude demonstrates a clear initial transition from linear to nonlinear growth. Since the growth rate in this simulation is so high, the wave amplitude stay several dB above the trapping threshold. This results in smooth, nonlinear growth with none of the particles being de-trapped. As shown in panel (d), by $t = 0.56$ seconds the wave amplitude continues to undergo nonlinear growth and remain significantly above the threshold; the growth quickly saturates quickly. That is, at any particular point within the pulse, a stationary observer would no longer observe the wave to be growing. However, the wave still continues to grow spatially, but with nonlinear growth rate. As shown in panel (e), the back end of the pulse of the pulse has passed the point where any linear growth and the wave amplitude remains saturated at every other point in space.

  This is particularly interesting because this simulation essentially shows two mechanisms of spatial growth. The first is realized by linear growth as mentioned previously, while the second mechanism is through large nonlinear growth. This is an important distinction to make since linear growth is often interchanged with spatial growth in the literature when it may not indeed be the case. At the receiver, no temporal growth is observed since all the temporal growth took place deeper within the simulation domain. Even though temporal growth is not observed at the output, the growth is still considered nonlinear since the particle trajectories are far from adiabatic.

4.5.3   Nonlinear Frequency Change

Although the focus of this chapter is on wave amplification, frequency change is a well documented characteristic of the triggered emission phenomena and examining it within the framework of the simulations is a useful task. For this reason, we once again examine three simulations with three different hot plasma densities $N_{\mathrm{h}} = 0.02$, 0.1, and 0.5 el/cm^3. However, for these cases we also show the wave-frequency profile and resonant currents at a particular snapshot in time. The corresponding equatorial linear growth rates are 25, 125, and 625 dB/sec. Once again we use the following
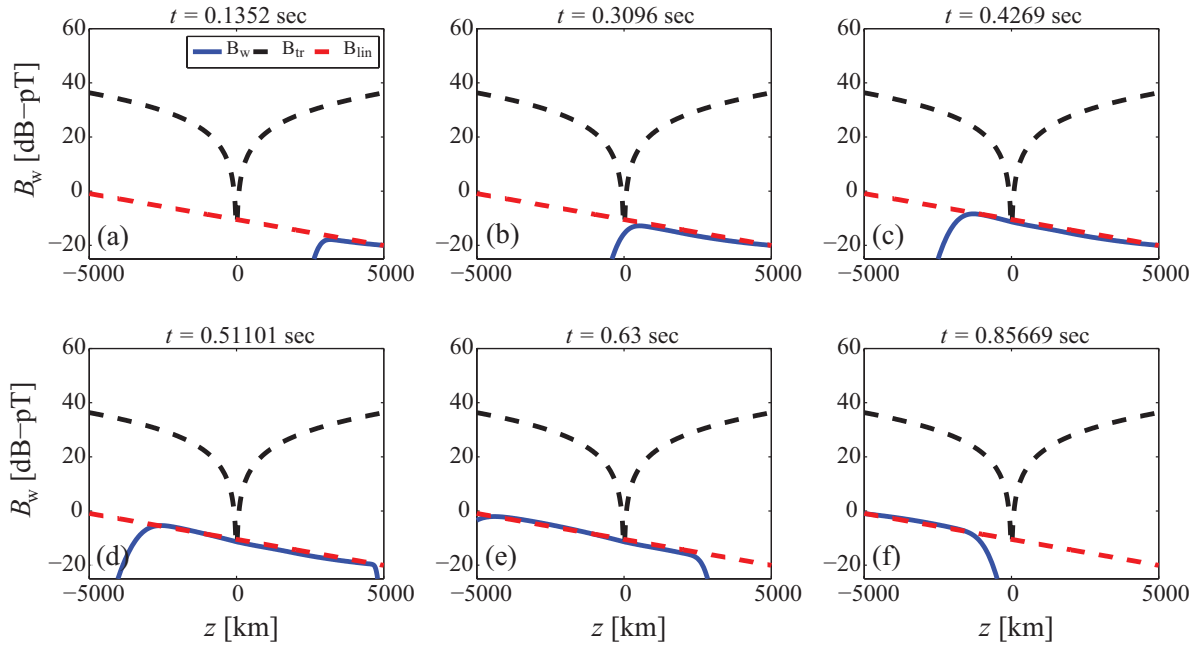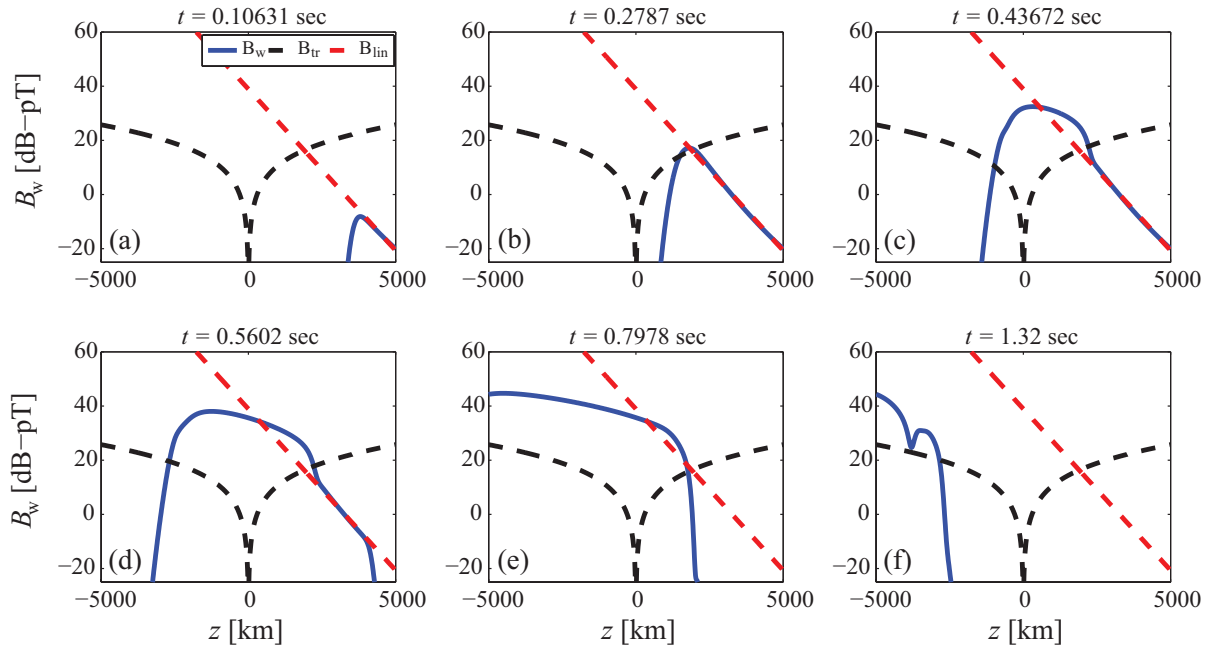
Figure 4.7: Result of a simulation $N_h = 0.96$ el/cm^3. Each subplot shows single snapshot in time of the wave amplitude spatial profile as it propagates through the simulation space. The wave amplitude first follows the linear theory prediction as shown in (a) and (b). Once it crosses the the minimum amplitude for trapping, it undergoes nonlinear growth but quickly reaches temporal saturation. The result is spatial nonlinear growth as shown in (e) until the back end propagates out of the simulation space.

background parameters: $L = 4$, $N_{\text{cold}} = 250$ el/cm^3, $f_0 = 1.5$ kHz.

The simulation results are shown in Figure 4.8, with each row corresponding to one simulation. The first column shows the wave amplitude as a function of position, the second column shows the wave frequency while the third column shows the corresponding resonant currents (J_E and J_B). Figure 4.8 (a), (b) and (c) show the wave and current profiles at $t = 0.75$ sec for $N_{\text{h}} = 0.02$ el/cm^3. As shown, this case has the lowest hot plasma density, the wave amplitude does not cross the trapping threshold (shown by the dashed black curve) and the growth is well described by linear theory. In this linear regime, the frequency does not change from the injected value of 1500 Hz. This is because the component of the current in the direction of the wave magnetic field (J_B) is responsible for frequency change and should be identically zero according to linear plasma theory. As shown in panel (c), J_B is approximately an order of magnitude less than J_E and linear theory is thus accurate in this case. Figure 4.8 (d), (e) and (f) show the wave and current profiles for $N_{\text{h}} = 0.1$ el/cm^3. In this case, the linear growth was high enough to make the wave amplitude exceed the trapping threshold. As can be seen, the amplitude crosses the threshold very close to the equator which is similar to the case in Figure 4.9. Panel (e) shows the frequency profile which has not deviated significantly from the original 1500 Hz even where the wave growth is nonlinear. The current profiles in panel (f) are largest for $z < 0$ where the wave amplitude is above the trapping threshold and hence nonlinear. The last case, with $N_{\text{h}} = 0.5$ el/cm^3 is shown in panel (g), (e) and (f). In this case, the wave amplitude crosses the trapping threshold significantly before the wave passes the equator. The wave subsequently undergoes significant nonlinear growth and reaches values of approximately 100 dB-pT at the exit of the simulation space. Note that the back end of the pulse does not look like it has traveled as far as the cases with the lower hot plasma densities (panels (a) and (d)). This occurs because particles that leave the back end of the pulse are forced to fall out of the trap and radiate additional wave energy in the process. This extends the pulse length as well as changes the wave frequency which is shown in panel (h). The frequency deviation is continuous but not at a constant sweep rate. This is consistent with [75] where hooks and oscillating tones were found for cases with the largest wave amplitudes. In this simulation, the frequency change (triggering) occurs close to where the wave crosses the trapping threshold and essentially propagates away from that location. This result suggests that the transition from trapping to de-trapping of resonant particles plays an important role in the triggering free running emissions.

4.5.4   Phase-space Hole

So far, we have shown that the model demonstrates nonlinear growth due to the phase-trapping of resonant electrons. This was shown by inspecting the deviation of the simulation from the linear theory prediction once the amplitude crossed the minimum value required for trapping. Although we have confirmed that nonlinear growth initiates once the wave begins to trap particles, examining the particle distribution function can provide a deeper understanding of the underlying phase-space
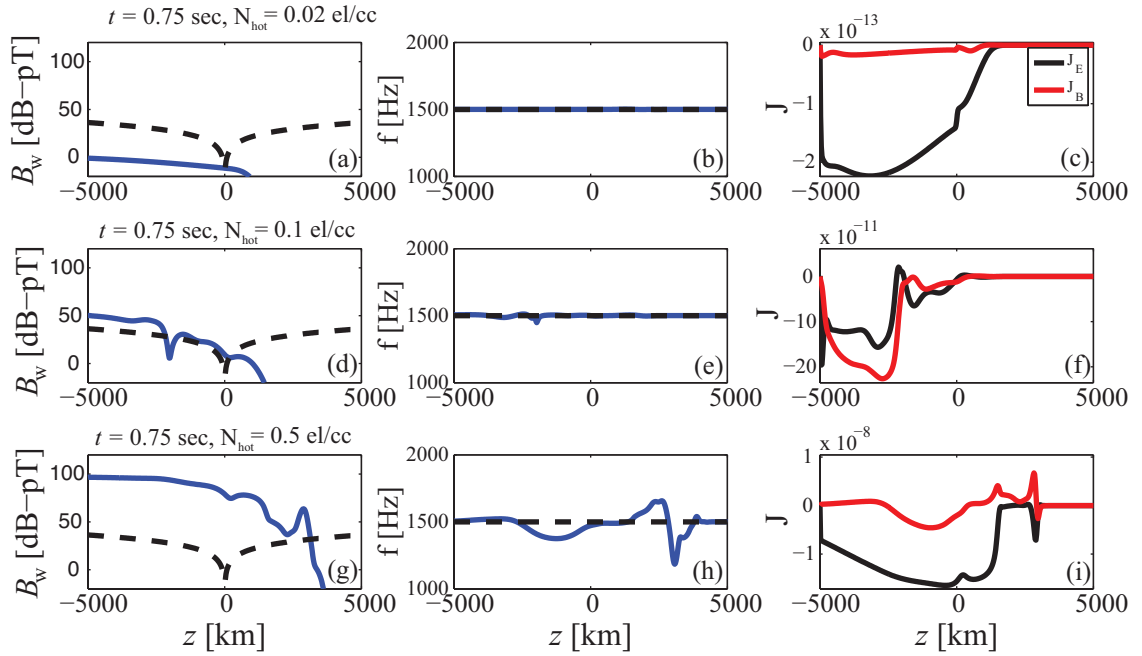
Figure 4.8: Panels (a), (b) and (c) show the wave amplitude, wave frequency and currents respectively for $N_h = 0.02$ el/cm^3. The wave growth is purely linear in this case and there is no frequency change since the amplitude does not cross the trapping threshold. Panels (d), (e) and (f) show the amplitude, frequency and resonant current profiles for $N_h = 0.1$ el/cm^3. The wave growth crosses the trapping threshold in this case which occurs primarily for $z < 0$. Although the wave amplitude is large enough to be nonlinear the frequency change is still small as shown in panel (e). Panels (g), (h) and (i) show the amplitude, frequency and currents for $N_h = 0.5$ el/cm^3. The linear growth rate is extremely high in this case (625 dB/sec) and crosses the trapping threshold much before the wave crosses the equator. The wave growth is subsequently nonlinear with a nonzero frequency change that resembles a triggered emission.

structure that leads to nonlinear growth and saturation. In order to clearly show the difference in the distribution between the linear and nonlinear regimes we consider another simulation that shows both types of growth within the simulation domain at the same time. In particular, Figure 4.9 shows the results of a simulation with a 4.5 kHz initial frequency and $N_h = 0.5$el/cm^3. Figure 4.9 (a) and (b) show the wave amplitude and phase profiles respectively at three different snapshots in time. As shown in panel (b), the wave phase profiles only change significantly after sustained crossing of the trapping threshold (shown by the dashed curves), which occurs after the wave has passed the equator, i.e. for $z < 0$. Figure 4.9 (c) and (e) shows the amplitude profile after the wave has filled the simulation space ($t = 0.8$ sec). As can be seen, the wave amplitude grows according to linear theory before crossing the equator ($z > 0$). The perturbation to the phase-space distribution in $(\hat{p}, \phi)$ space (integrated over $p_\perp$) is shown in panels (d) and (f) at two positions $z = +3325$ km and $z = -1525$ km, respectively. The distribution functions shown are first subtracted from the unperturbed distribution and then normalized to the maximum value. The distribution in panel (d) corresponds to the linear regime. Close to the equator, the wave amplitude starts to deviate from the prediction of linear theory. The reason nonlinear growth occurs primarily for ($z < 0$) is because linear growth brings the wave amplitude up to trapping threshold only very close to magnetic equator. If the linear growth rate or the injected wave amplitude were higher, the trapping threshold would be crossed sooner and nonlinear growth would initiate before the wave reaches the equator.

The phase-space distribution well into the nonlinear regime is shown in Figure 4.9 (f) and a strong depletion in phase-space density inside the phase trap, resulting in a "phase-space hole" [95, 78, 43], is clearly visible. The hole is created since particles trapped downstream (of the wave) stay trapped at resonance for several trapping periods and, by Liouville's theorem, will drag the value of the phase-space density from the region downstream where they were first trapped. Since the resonance velocity increases with distance away from the equator, the phase-space density will be lower inside the trap than outside and is thus referred to as a "hole" [79]. The theoretical idea of the phase space hole has been proposed by several authors and our model serves as useful validation of this concept. The well defined boundaries and shape of the phase-space hole in 4.9 (d) can be contrasted with the result shown in Figure 7 of [43] that was obtained using a full electromagnetic-PIC simulation. The ability to clearly resolve details in phase-space is one of the primary advantages of using an Eulerian Vlasov solver.

4.5.5 Saturation

The depth of the hole in general varies as a function of time and depends on the trapping history of particles and can even be negative (hill instead of a hole) on the upstream side if the wave amplitude is above the trapping threshold. In particular, the simulations demonstrate that the density of the hole eventually reaches a steady state at which point the wave amplitude reaches a temporal saturation. The reason for this is that as the wave grows in time the size of the trap increases with it, which
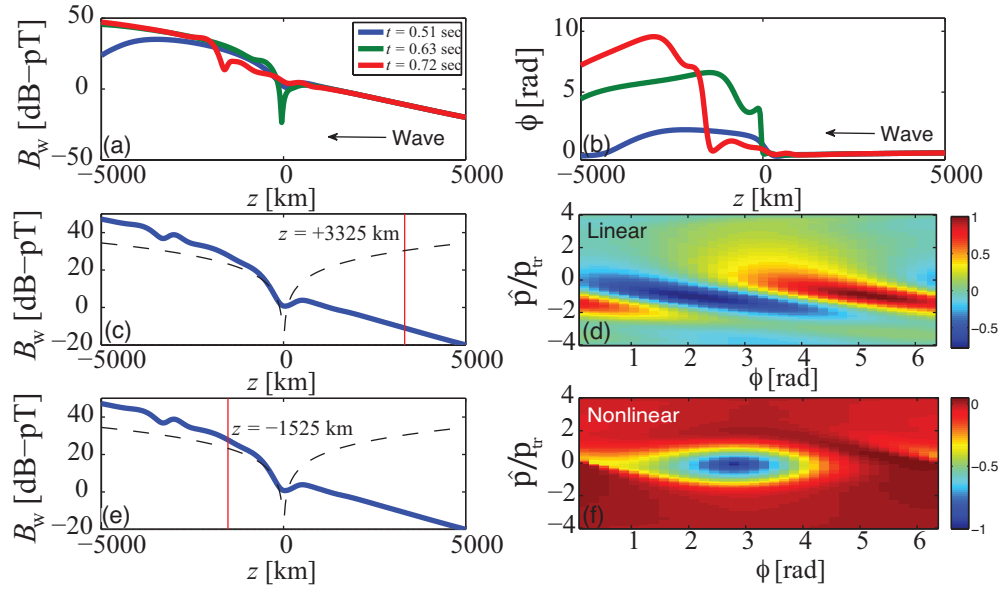
Figure 4.9: Panels (a) and (b) show the wave amplitude and phase respectively at three different time samples ($f_0 = 4.5$ kHz). The wave amplitude grows according to linear theory for $z > 0$ and becomes nonlinear for $z < 0$ after crossing the trapping threshold. As shown in panel (b), a non-zero phase shift occurs only for $z < 0$ (nonlinear region) and is responsible for the changing frequency of a triggered emission. Panel (c) shows the wave amplitude profile once the wave has filled the simulation space ($t = 0.8$ sec) while (d) is the phase-space distribution (integrated over $p_\perp$) in the linear growth regime ($z = 3325$ km). Panels (e) and (f) show the wave profile as well as the phase space distribution in the nonlinear regime ($z = -1525$ km). In the nonlinear regime, there is a clear depletion in phase space within the trap resulting in a stable "phase-space hole". The dashed black curves in panels (c) and (e) represent the minimum amplitude required for phase-trapping.

reinforces the temporal growth. However, as time progress, the particles that are within the trap at any particular point in space will eventually arrive from locations furthest down the field line where the system is essentially unperturbed. At every subsequent time step, the value inside the trap will then be approximately the same as the particles that can arrive are governed by Liouville's theorem. In other words, for a finite interaction length there is a maximum depth that the phase-space hole can achieve. At this time, even though the density in the trap will remain steady in time the trap will still contribute a nonzero resonant current. The nonzero current ensures that the growth, once temporal saturation occurs, does not cease to exist but is rather purely spatial. The exact saturation value depends on the input amplitude and the linear growth rate since the time at which trapping (and hence nonlinear growth) begins depends specifically on these two variables in addition to the background cold plasma parameters.

To examine how the saturation amplitude changes as a function of input amplitude and linear growth rate we consider simulations over a range of input wave amplitudes 0.0001 pT$< B_{in} <$1 pT and for the three hot plasma densities utilized previously (N_{h} = 0.02, 0.1, and 0.5 el/cm^3). The simulation results are shown in Figure 4.10. The top panel of Figure 4.10 shows the saturation amplitude as a function of input wave amplitude for the three different hot plasma densities. The bottom panel shows the total gain in decibels as a function of input amplitude.

First consider the case with the lowest hot plasma density N_{h} = 0.02 el/cm^3 as is shown by the blue curves in Figure 4.10. As demonstrated previously, for an input amplitude of -20 dB-pT, the growth is purely linear. As expected, the saturation amplitude increases linearly with the input amplitude as indicative of linear theory. Equivalently, the gain as shown in the bottom panel, is approximately flat as a function of input amplitude. Once the hot plasma density is increased to N_{h} = 0.1 el/cm^3, the simulations no longer match linear theory and the saturation amplitude is a nonlinear function of the input amplitude. As shown, the saturation amplitude continues to increase with input amplitude and begins to level off at larger input amplitudes. This behavior continues into the cases with the highest hot plasma density N_{h} = 0.5 el/cm^3 and is shown by the black curves. In this case, the saturation amplitude is once again a nonlinear function of the input amplitude, however, certain new features emerge. At approximately -65 dB-pT, the gain (bottom panel) changes from an increasing to a decreasing function of input wave amplitude. This behavior can also be seen on the top panel when the saturation amplitude seems to slow down in growth after approximately -65 dB-pT. This is a particularly interesting feature since this suggests that increasing the input amplitude will eventually be counterproductive if gain efficiency is the priority. Even though a steady phase space trap density seems to be driving temporal saturation in our model, it may not be the only mechanism of saturation. Power loss from the duct, coupling to other wave modes or alternative mechanisms may also play a role in the saturation of coherent VLF signals.
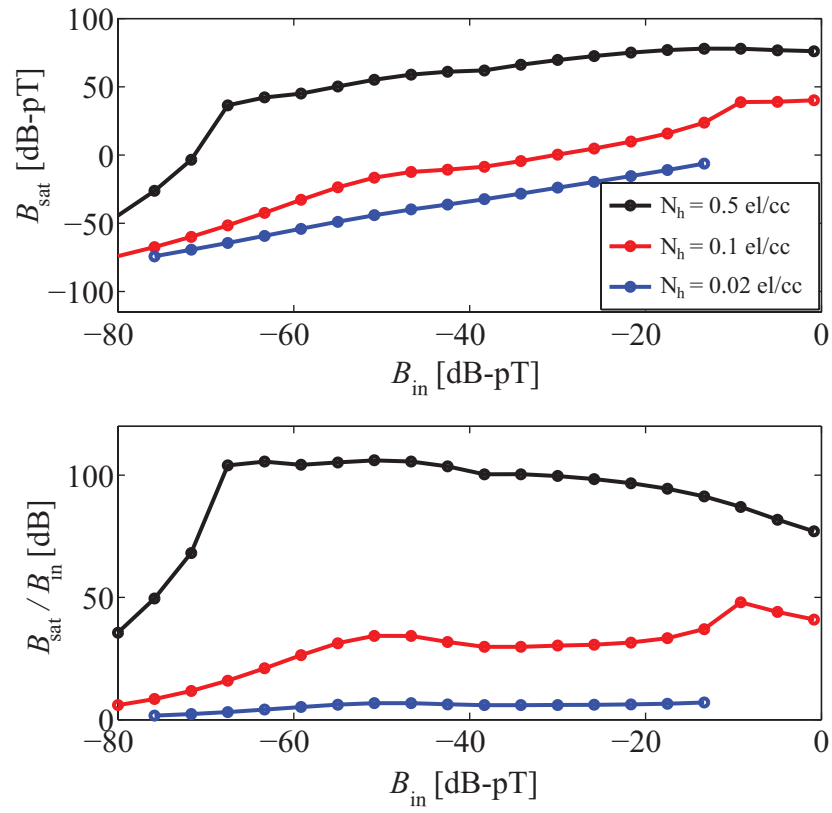
Figure 4.10: Model saturation amplitudes and gain as a function of input amplitude for three different hot plasma densities.

4.6   Model Assumptions and Limitations

In this chapter, we have so far demonstrated that the upwind finite difference method applied to the narrowband Vlasov-Maxwell system can reproduce nonlinear growth, amplitude saturation and frequency change of injected pulses. In this section, we discuss some of the inherent physical assumptions and numerical limitations of the model.

4.6.1   Physical Assumptions

In developing the model, several physical assumptions were made for computational feasibility and to simplify analysis. Below, we describe some of the more prominent concerns.

Spatial Dimensions

As discussed, the physical model uses all three velocity coordinates but only one spatial coordinate. Apart from simply reducing the dimensionality of the problem, this simplification is useful for additional reasons. The first reason is that the electron's guiding center can be taken to follow the field line which is a good approximation as long as the magnetic field changes on a scale much smaller than the gyro radius. This allows the model to neglect transverse variations in the electron's position which makes calculating the currents easier while still taking physical effects such as particle mirroring into account. Additionally, this simplification also allows the use of the plane wave assumption on the whistler mode waves and eliminates the need to integrate the field equations in the geomagnetic field geometry.

   The disadvantage of the 1D assumption is that certain physical features are neglected. Specifically, electron drift due to the curvature of the Earth's magnetic field is explicitly removed when constructing the equations of motion. This may cause issues for simulations over longer time scales; however, for the simulations presented in this thesis it is not much of a concern since electron drifts occur on timescales of several seconds. Additionally, any traverse effects on the fields due to propagation inside a magnetospheric duct (such as frequency cutoffs from ducting modes), can not be taken into account with the 1D geometry.

Parallel Propagation

Closely related to the 1D simplification is the assumption of parallel propagation. The parallel propagation assumption comes from the more fundamental postulate of ducted propagation. The duct essentially acts like a waveguide and forces the wavenormal vector to remain essentially parallel to the geomagnetic field and wave electric and magnetic field perpendicular to the direction of propagation. In general, however, the wave normal angle can deviate away from the magnetic field and can take on a small but nonzero value. In this case, the equations of motion must be updated as described in [58] to include an oblique propagation direction. Physical concepts such as

phase trapping remain qualitatively the same but with some small modifications which may impact the simulation results. So far, however, no self-consistent wave growth models have taken oblique propagation into account. Additionally, if the wave normal angle becomes large enough, it may even leave the duct at which point the wave must be tracked with ray tracing methods while keeping track of nonlinear growth which is a difficult task. We suggest this addition as a step for future work.

Narrowband Assumption

The most useful and possibly most limiting assumption of the presented model is the narrowband assumption. As mentioned previously, the narrowband condition is incorporated by assuming that the bandwidth of the waves does not change significantly from the transmitted frequency. This can also be thought of as a "slowly varying" assumption which allows the model to keep track of a slowly varying amplitude and phase. The slowly varying aspect permits the use of a relatively course grid as long the waves remain narrowband. Additionally, the cold plasma fluid equation simply represents itself as the group velocity in the narrowband equations and does not need to be solved explicitly. The primary concern is the inclusion of multiple discrete waves. There have been many observed cases of wave-wave interactions [42] that can not be described by a narrowband model. Additionally, broadband wave structures such as whistlers or incoherent hiss may not accurately be captured by the model. Future iterations of the model should be upgraded to allow multiple waves or solve Maxwell's Equations without approximation.

Unidirectional Waves

The model also assumes that waves only propagate in one direction. This allows the model to avoid any complications with backward traveling waves. This is particularly useful since the phase-space velocity grid only needs to be centered around the resonance velocity for the forward going wave. Otherwise, the grid would need to be extended down to negative velocities where resonance for the backward going wave takes place. Alternatively, a second phase-space grid could be used if the backward and forward going waves are assumed to be decoupled at the expense of doubling the computation. Including the backward going wave is not necessary in the case of ground based injected waves especially since data does not show backward going waves apart from the echoes that reflect at the ionosphere. The disadvantage of not including the backward waves is that naturally occurring waves often travel in both directions. Waves such as magnetospheric chorus are believed to be generated close to the equator and propagated away towards both hemisphere. The model would thus not be able to accurately capture the physics of waves generated at the equator and propagating away in both direction. Once again, utilizing Maxwell's Equations without approximation would eliminate this problem but at the expense of computational concerns.

4.6.2   Numerical Discussion

We have so far discussed the key physical assumptions of the model, however, numerical effects are equally important to consider when interpreting the results.

Numerical Diffusion

It is worth noting that the first order upwind scheme utilized in the model is known to be dissipative when large gradients are formed or equivalently if the grid is too course. This can be seen in a few different ways. Here, we demonstrate this by computing the truncation error associated with the first order upwind scheme. As mentioned before, finite difference schemes solve the original differential equations but with an added error that indicates the order of accuracy. In particular, let us consider the model advection equation approximated by the first order upwind FD scheme. Again, the model advection equation is given by $\frac{\partial f}{\partial t} + v_a \frac{\partial f}{\partial z} = 0$ where we assume v_a is a positive constant for simplicity and the CFL number, $C_{max} = \frac{v_a \Delta t}{\Delta z}$, is a positive constant less than 1. Once the FD scheme is applied and is subject to Taylor series analysis, it can be shown that the upwind scheme solves the following differential equation exactly:

$$\frac{\partial f}{\partial t} + v_a \frac{\partial f}{\partial z} + \frac{v_a \Delta z}{2}(C_{max} - 1)\frac{\partial^2 f}{\partial z^2} + O(\Delta z^2) = 0 \tag{4.11}$$

As shown, the leading order error term is given by $\frac{v_a \Delta z}{2}(C_{max} - 1)\frac{\partial^2 f}{\partial z^2}$ since it contains the first power of Δz. In other words, the FD upwind scheme solves the model advection equation with first order accuracy. However, the upwind scheme can also be thought of as solving the following equation $\frac{\partial f}{\partial t} + v_a \frac{\partial f}{\partial z} + \frac{v_a \Delta z}{2}(C_{max} - 1)\frac{\partial^2 f}{\partial z^2} = 0$ with second order accuracy as shown in Equation (4.11). The new equation is known as the convection-diffusion equation since both phenomena are present in the same equation (advection and convection are used interchangeable in this discussion). Specifically, the diffusion term $\frac{v_a \Delta z}{2}(C_{max} - 1)\frac{\partial^2 f}{\partial z^2}$ has a diffusion coefficient given by $D = \frac{v_a \Delta z}{2}(C_{max} - 1)$. Therefore, a larger spatial grid spacing will result in a larger diffusion coefficient which will manifest itself as a signal that damps and spreads out (i.e diffuses). This type of artificial diffusion cannot be overcome without making the grid extremely fine, however, at the same time, a very fine spatial mesh decreases the time step due to the CFL stability condition. This results in an unavoidable tradeoff between unwanted numerical diffusion and the number of time steps required to run the simulation. Incorporating a higher order finite difference scheme can overcome some of these concerns but at the cost of computational complexity. Increasing the order of accuracy and controlling the diffusion in the Vlasov-Maxwell solver is a subject of future work.

Positivity Preserving

Even though the upwind scheme suffers from artificial diffusion it has the particularly useful feature of being positivity preserving. That is, if the initial function is positive everywhere, then it will remain positive through the entirety of the simulation. Since the particle density is the quantity being tracked in the Vlasov solver and negative particle density has no physical meaning, the positivity preserving property is essential. Additionally, when simultaneously applying this scheme to the narrowband wave equations, the wave amplitude also remains positive during the simulations. Although this is physically necessary, it is not readily apparent to be true numerically in presence of resonant currents. The wave equations have currents that act as forcing terms and can be negative or positive depending on the particle distribution in gyro phase. Even so, none of the simulations considered in this report produced a negative wave amplitude when employing the first order upwind scheme.

Phase-Space Grid Selection

Although the construction of the phase-space grid has been discussed earlier in this chapter there are some additional aspects that warrant discussion. As mentioned, the size of the grid in $\hat{p}$-space (or equivalently $v_{\parallel}$-space) is selected by first determining the size of the trap (v_{tr}) based on the average amplitude predicted by linear theory and then creating the grid to go $\pm 5 v_{\text{tr}}$ (the size of 5 traps) around resonance. The first concern is if nonlinear growth is extremely large, either the smallest trap will not be resolved or the largest trap will not be contained in the grid. However, there is no way to circumvent this problem without using an unstructured or nonuniform grid. Using an unstructured grid will of course defeat the purpose of using a finite difference scheme. Additionally, if the wave grows significantly (thereby creating a large trap) and the wave frequency also changes dramatically, then the trap can slide out of the simulation space. One method of resolving the trap across the domain properly is by transforming to a new coordinate that is normalized by the local size of the trap at each time step and re-centers the resonance velocity depending on the updated wave frequency. This method, however, requires computing a time dependent Jacobian at each time step which includes derivatives of the wave amplitude and frequency and may be difficult to perform accurately. Future iterations of the model can explore the use of such an approach or consider adaptive mesh techniques.

Boundary Conditions

The boundary conditions used in updating the particle distribution function simply enforce the unperturbed conditions at the boundary of every phase space coordinate except for gyro-phase (which uses periodic boundary conditions). This type of boundary condition seems to suit the problem well and does not lead to any numerical instabilities in the system. The boundary conditions

can be changed to adopt inflow or outflow rules for future simulations. These conditions can be enforced in the cases of loss due to precipitation, interactions with an injected electron beam or other related applications. Additionally, the boundary conditions for the wave equations simply enforce the injected signal profile at the entrance grid point. The wave boundary conditions can also be taken into account by enforcing the appropriate currents at the boundary, however, directly enforcing the wave amplitude and phase seems to work well in the simulations.

Wave Phase Update

As mentioned previously, the narrowband wave equations are solved in amplitude and phase form to take advantage of the slowly varying nature of these variables. The primary concern is that the phase update equation, shown in Equation (4.5), contains the wave amplitude in the denominator of the forcing term (right hand side term). This can cause an artificial instability in the wave phase if the wave amplitude drops too low. In all the simulation cases we have presented thus far, the initial particle distribution is unstable to waves and the growing amplitude will never be small enough to be a concern. However, when distributions with low degrees of anisotropy are considered, the waves will damp and the phase update equation eventually becomes numerically unstable when the wave amplitude becomes extremely small. This concern can be eliminated by solving the wave equations in vector form instead of tracking an amplitude and phase and we suggest this as an addition for future iterations of the model.

4.7 Summary

We have shown that coherent wave amplification in the Earth's radiation belts can be modeled using a finite difference scheme on a uniform grid after transforming to a resonance subtracted coordinate system. We used a first order upwind scheme which is the simplest stable scheme, but is diffusive. With this scheme, the model demonstrates both linear as well as nonlinear growth, with the formation of a stable and well defined phase-space hole during the nonlinear growth process. The point at which the transition from linear to nonlinear takes place depends on the linear growth rate such that linear growth can raise the wave amplitude above the trapping threshold. For low growth rates, the amplification is purely linear since the trapping threshold is never exceeded. For the case with a large linear growth rate, the trapping threshold is crossed quickly and a continuous change in frequency takes place close to where the wave first crosses the threshold and propagates away from there. This suggests that particles leaving the back end of the wave trap are an important part of the triggering process. Even with the successful simulation cases, there is still much room for improvement. Upgrading to a higher order accurate scheme that can allow for broadband waves or multi-wave interactions would be a useful next step for the model. We leave these additions as tasks for future research.

Chapter 5

Summary and Suggestions for Future Work

5.1 Summary of Contributions

Modeling the interaction between coherent whistler mode waves and radiation belt electrons is an important component of space weather dynamics and also a fundamental theoretical concept in plasma physics. In this dissertation, two aspects of wave-particle interactions have been addressed: the amplification of coherent VLF waves by an unstable radiation belt electron distribution as well as the precipitation of these particles induced by the waves. To evaluate precipitation induced by large amplitude whistler mode waves, a backward trajectory integration technique was utilized as part of the Vlasov-Liouville (VL) model. Since the loss cone is well defined, the backward integration method captures the precipitated flux without the complications of under sampling in forward scattering models. The VL model demonstrated that linear scattering theory is a good estimate for precipitation at low amplitudes as expected, however, the range of amplitudes over which it remains accurate depends strongly on the initial hot plasma distribution. The VL model also revealed that for large amplitude signals, the induced precipitated flux is dominated by phase-trapped resonant electrons. Finally, the precipitation model demonstrated the complex time signature of the precipitated flux induced by short duration whistler mode signals. To model wave growth, a self consistent finite difference upwind scheme that has not previously been employed for this problem was utilized. For low hot plasma densities, the FD model demonstrated wave growth that is consistent with the analytical solution of the linearized Vlasov-Maxwell system. When the plasma density is increased, the model showed that the wave first grows according to linear theory until the minimum amplitude for trapping particles was crossed at which point the amplitude immediately deviates from the linear theory prediction and grows nonlinearly. During the nonlinear growth phase, the model revealed a

depletion in the region of phase-space where a wave-induced trap is theorized to exist with much greater detail than previously attempted computer simulations. The model also predicts the saturation of signals once the particle density in the phase-space trap reaches a quasi-steady state. Additionally, the simulations demonstrated that dynamic frequency change can occur at the back end of an injected pulse when the hot plasma density (or equivalently growth rate) is large enough.

5.2 Suggestions for Future Work

Although the models described in this work provides useful contributions to the science of wave-particle interactions in the Earth's radiation belts, there are certain physical aspects that are not captured by the present simulations. The FD wave growth model described in this dissertation relies on several physical assumptions to reduce the computational cost. The most important of which is the narrowband wave assumption. This assumptions allows the use of a coarser spatial grid, enforces unidirectional wave propagation and incorporates the effects of the cold plasma. The concern, however, is that these equations may restrict the bandwidth of the signal and accordingly limit some of the physics. Specifically, the triggering of fee running emissions inherently involves the creation of new frequency components that deviate from the original transmitted frequency. One possible method of doing this is to modify the wave equations to allow for multiple coherent waves. In this way, a separate mesh can be used for each wave while still keeping the spatial grid step relatively large and without having to solve a separate cold fluid equation. Although we pose a multi-wave narrowband model as a possible option it still throws away certain physical phenomena (such as dispersion), the most general means of approaching the problem is by solving Maxwell's Equations directly in the presence of a cold plasma fluid. Although this has been employed in recent particle-in-cell simulations, it requires an artificial scaling to the background field to keep the spatial domain smaller than the physical problem. Otherwise, solving Maxwell's Equations over a $\approx 10{,}000$ km domain for signals with ~ 10 km wavelength will require tens of thousands of spatial grid points to provide an accurate solution. This would be extremely computationally expensive but is not impossible with modern day parallel computing or supercomputing resources and we provide this as a suggestion for future research.

Although the Vlasov-Liouville model of precipitation is quite accurate for known wave fields, the model is not technically self-consistent. That is, the VL model only determines the precipitated phase-space distribution through backward trajectory integration, however, the particles outside of the loss cone are responsible for amplifying the wave and are not accounted for. One way to get around this concern is to find the self-consistent wave solution from a wave growth model (such as the finite difference upwind model) and then use the output of this simulation as an input to the precipitation model. Combining the two models into one larger model will allow an accurate, self-consistent simulation of wave growth along with particle precipitation and we suggest this as a

subject for future work.

Appendix A

Narrowband Wave equations Derivation

In order to derive the narrowband wave equations we first begin by transforming Maxwell's Equations into the Fourier domain. Specifically, Maxwell's Equations in their current form $(2.1)-(2.4)$ are expressed in terms of the evolution in space-time $(\mathbf{r}, t)$. However, by explicitly applying the spatial-temporal Fourier transform, $\mathbf{E}(\mathbf{r}, t) = \int \int \hat{\mathbf{E}}(\mathbf{k}, \omega) e^{i(\omega t + \mathbf{k} \cdot \mathbf{r})} d\omega d\mathbf{k}$, Maxwell's Equations can be expressed in the $(\mathbf{k}, \omega)$ domain.

The curl equations transform to,

$$i\mathbf{k} \times \hat{\mathbf{E}} = -i\omega \hat{\mathbf{B}} \qquad\qquad i\mathbf{k} \times \hat{\mathbf{B}} = \mu_0 \hat{\mathbf{J}} + i\mu_0 \epsilon_0 \omega \hat{\mathbf{E}} \tag{A.1}$$

where the hat notation refers to the transformed system. Additionally we assume no space-charge $\rho = 0$ so the divergence equations transform to,

$$\mathbf{k} \cdot \hat{\mathbf{E}} = 0 \qquad\qquad \mathbf{k} \cdot \hat{\mathbf{B}} = 0 \tag{A.2}$$

which implies that $\hat{\mathbf{E}}$, $\hat{\mathbf{B}}$, and $\mathbf{k}$ are all orthogonal to each other. These equations can then be combined to give

$$(k^2 - \frac{\omega^2}{c^2})\hat{\mathbf{E}} = -i\mu_0 \omega \hat{\mathbf{J}} \tag{A.3}$$

which is the wave equation in the Fourier-domain. The current term $\hat{\mathbf{J}}$ must be split into a hot and cold component to model the background cold fluid and the hot radiation belt plasma which gives $\hat{\mathbf{J}} = \hat{\mathbf{J}}_c + \hat{\mathbf{J}}_h$.

To model the cold plasma current, we must start with the cold fluid approximation. That is, the background plasma is defined by a fluid velocity $\mathbf{v}$ and is assumed to have no thermal energy.

In the reference frame moving with the fluid, the fluid element will evolve under the Lorentz force, $\frac{d\mathbf{v}}{dt} = \frac{q}{m}(\mathbf{E} + \mathbf{v} \times \mathbf{B})$ where $\frac{d}{dt}$ represents the derivative in the moving frame. Since wave solutions are anticipated, it is assumed that any waves in the system will propagate much faster than the cold fluid velocity. In this case, the operator $\frac{d}{dt}$ can be approximated by the partial derivative $\frac{\partial}{\partial t}$. Furthermore, it assumed that the background magnetic field, $\mathbf{B}_0 = -B_0\hat{\mathbf{z}}$ is much larger than any wave induced perturbations, i.e., $\mathbf{B}_0 \gg \mathbf{B}_w$. Under these assumptions, the cold fluid equation becomes

$$\frac{\partial \mathbf{v}}{\partial t} = -\frac{q}{m}(\mathbf{E}_w + \mathbf{v} \times \mathbf{B}_0) \tag{A.4}$$

and $\mathbf{v} \times \mathbf{B}_0$ can be written as $\hat{\mathbf{C}}\mathbf{v}$ where $\hat{\mathbf{C}} = \begin{pmatrix} 0 & -B_0 \\ B_0 & 0 \end{pmatrix}$ and motion in the z-direction is neglected. By transforming to the Fourier domain, the cold equation becomes.

$$i\omega\hat{\mathbf{v}} = -\frac{q}{m}(\hat{\mathbf{E}}_w + \hat{\mathbf{C}}\mathbf{v}) \tag{A.5}$$

Defining, $\hat{\mathbf{J}}_c = qN_c\hat{\mathbf{v}}$, the fluid equation can be written as

$$\hat{\mathbf{J}}_c = \frac{\omega_p^2 \epsilon_0}{\omega_c^2 - \omega^2} \begin{pmatrix} i\omega & \omega_c \\ -\omega_c & i\omega \end{pmatrix} \hat{\mathbf{E}}_w \tag{A.6}$$

which can then be substituted into (A.3) to give

$$(k^2 - \frac{\omega^2}{c^2})\hat{\mathbf{E}} = -i\mu_0\omega \frac{\omega_p^2 \epsilon_0}{\omega_c^2 - \omega^2} \begin{pmatrix} i\omega & \omega_c \\ -\omega_c & i\omega \end{pmatrix} \hat{\mathbf{E}} - i\mu_0\omega\hat{\mathbf{J}}_h \tag{A.7}$$

where the w subscript has been dropped. Rearranging to combing like terms in $\hat{\mathbf{E}}$ results in

$$\left[(k^2 - \frac{\omega^2}{c^2})\hat{\mathbf{I}} - \mu_0 \frac{\omega_p^2 \epsilon_0}{\omega_c^2 - \omega^2} \begin{pmatrix} \omega^2 & -i\omega\omega_c \\ i\omega\omega_c & \omega^2 \end{pmatrix} \right] \hat{\mathbf{E}} = -i\mu_0\omega\hat{\mathbf{J}}_h \tag{A.8}$$

where $\hat{\mathbf{I}}$ is the identity matrix. We then make the restriction that the waves are right-hand circularly polarized to enforce whistler-mode waves and also assume no transverse dependence, i.e $\mathbf{E}(t, \mathbf{r}) = \mathbf{E}(t, z)$. In particular all quantities are assumed to be polarized as $\hat{\mathbf{E}} = \hat{E}(\hat{\mathbf{x}} + i\hat{\mathbf{y}})$. Then, (A.8) becomes

$$D(k, \omega)\hat{E} = -i\omega\mu_0\hat{J}_h \tag{A.9}$$

where $D(k, \omega) = k^2 - \frac{\omega^2}{c^2} - \frac{\omega_p^2(\omega^2 + \omega\omega_c)}{c^2(\omega_c^2 - \omega^2)}$ and is equivalent to the cold plasma dispersion relation (if set equal to zero). Using Equations (A.1), and defining the quantity $F(k, \omega) = \frac{D(k, \omega)}{k}$, Equation

(A.8) can be written in terms of the Fourier-domain magnetic field instead of the electric field to give:

$$F(k, \omega)\hat{B} = \mu_0 \hat{J}_h \tag{A.10}$$

The analysis done so far has not yet made any assumptions about the narrowband nature of the system and is quite general in that aspect. The narrowband assumption comes in by assuming $\hat{B}$ is only nonzero over a small range of frequencies and wave numbers around the injected signal values (k_0, ω_0). With this assertion, $F(k, \omega)$ can be expanded in a taylor series to first order $F(k, \omega) \approx F(k_0, \omega_0) + \frac{\partial F}{\partial \omega}\Big|_{k_0, \omega_0} (\omega - \omega_0) + \frac{\partial F}{\partial k}\Big|_{k_0, \omega_0} (k - k_0)$. Since (k_0, ω_0) satisfy the cold plasma dispersion relation, $F(k_0, \omega_0) = 0$. Equation (A.10) then becomes:

$$[a_1(\omega - \omega_0) + a_2(k - k_0)] \hat{B} = \mu_0 \hat{J}_h \tag{A.11}$$

where we define $a_1 = \frac{\partial F}{\partial \omega}\Big|_{k_0, \omega_0}$ and $a_2 = \frac{\partial F}{\partial k}\Big|_{k_0, \omega_0}$. By inverse transforming back to the space-time domain, (A.11) becomes

$$\left[a_1(i\frac{\partial}{\partial t} + \omega_0) + a_2(i\frac{\partial}{\partial z} + k_0)\right] \tilde{B} = -\mu_0 \tilde{J}_h \tag{A.12}$$

where $\tilde{B}$ and $\tilde{J}_h$ are the complex wave magnetic field and hot current respectively. Equation (A.13) can be divided by a_1 and rearranged to give

$$i\left[\frac{\partial}{\partial t} + \frac{a_2}{a_1}\frac{\partial}{\partial z}\right] \tilde{B} + (\omega_0 + \frac{a_2}{a_1}k_0)\tilde{B} = -\frac{\mu_0}{a_1}\tilde{J}_h \tag{A.13}$$

We then define,

$$\tilde{B} = \left[B_w e^{i\phi_w}\right] e^{i(\omega_0 t + k_0 z)} \qquad \tilde{J}_h = \left[J_h e^{i\phi_h}\right] e^{i(\omega_0 t + k_0 z)} \tag{A.14}$$

where B_w and J_h are the wave amplitude and hot current magnitude while ϕ_w and ϕ_h represent the wave and current phases respectively. This simply means we are tracking an envelope that is modulating the plane wave (cold plasma) solution.

Plugging (A.14) into (A.13) and defining the total derivative $\frac{D}{Dt} = \frac{\partial}{\partial t} + \frac{a_2}{a_1}\frac{\partial}{\partial z}$ gives,

$$ie^{i(\omega_0 t + k_0 z)}\frac{D}{Dt}\left[B_w e^{i\phi_w}\right] + i\left[B_w e^{i\phi_w}\right]\frac{D}{Dt}e^{i(\omega_0 t + k_0 z)} + (\omega_0 + \frac{a_2}{a_1}k_0)\left[B_w e^{i\phi_w}\right] e^{i(\omega_0 t + k_0 z)} = -\frac{\mu_0}{a_1}\left[J_h e^{i\phi_h}\right] e^{i(\omega_0 t + k_0 z)} \tag{A.15}$$

Once the derivatives are applied to the complex exponential, (A.15) can be simplified to:

$$\frac{D}{Dt}\left[B_w e^{i\phi_w}\right] = i\frac{\mu_0}{a_1}\left[J_h e^{i\phi_h}\right] \tag{A.16}$$

Applying the total derivative to the wave term then results in

$$e^{i\phi_w}\frac{D}{Dt}B_w + (i\frac{D}{Dt}\phi_w)B_w e^{i\phi_w} = i\frac{\mu_0}{a_1}\left[J_h e^{i\phi_h}\right] \tag{A.17}$$

which can then be multiplying by $e^{-i\phi_w}$

$$\frac{D}{Dt}B_w + (i\frac{D}{Dt}\phi_w)B_w = i\frac{\mu_0}{a_1}J_h e^{i\Delta\phi} \tag{A.18}$$

where $\Delta\phi = \phi_h - \phi_w$. At this point, the real and imaginary parts can be separated to give

$$\frac{D}{Dt}B_w = -\frac{\mu_0}{a_1}J_h \sin\Delta\phi \qquad \frac{D}{Dt}\phi_w = \frac{\mu_0}{a_1 B_w}J_h \cos\Delta\phi \tag{A.19}$$

Finally, it can be shown that the quantity $\frac{a_2}{a_1} = v_g$ and $a_1 = \frac{2}{v_g}$ where v_g is negative since the waves are assumed to go in the $-z$ direction. Then, by employing simple geometrical arguments and expanding the total derivative $\frac{D}{Dt}$, the equations in (A.19) become:

$$\frac{\partial B_w}{\partial t} - |v_g|\frac{\partial B_w}{\partial z} = -\frac{\mu_0 |v_g|}{2}J_E \tag{A.20}$$

and,

$$\frac{\partial \phi_w}{\partial t} - |v_g|\frac{\partial \phi_w}{\partial z} = -\frac{\mu_0 |v_g|}{2}\frac{J_B}{B_w} \tag{A.21}$$

where J_E and J_B are the components of the hot current in the direction of the wave electric and magnetic fields respectively.

Equations (A.20) and (A.21) are referred to as the "narrowband wave equations" and describe the evolution of the amplitude and phase of a modulating wave-packet. Note that in this derivation, it was assumed that the system is homogenous. As long as the background variables are slowly varying, these equations still hold and the slowly varying quantities will simply include a spatial dependence (i.e $v_g = v_g(z)$).

Appendix B

Linear Scattering Theory

Linear scattering theory involves expanding the equations of motion around the adiabatic particle trajectories. In particular, the equations of motion can be written as:

$$\frac{d\mathbf{p}}{dt} = \mathbf{F}_{\mathrm{w}} + \mathbf{F}_a \tag{B.1}$$

Where the quantities $\mathbf{p}$, $\mathbf{F}_a$, and $\mathbf{F}_{\mathrm{w}}$ represent the particle state, the "force" due to adiabatic motion, and the "force" due to the wave respectively.

$$\mathbf{p} = \begin{pmatrix} p_\parallel \\ p_\perp \\ \phi \\ z \end{pmatrix}$$

,

$$\mathbf{F}_{\mathrm{w}} = \begin{pmatrix} qB_{\mathrm{w}}v_\perp \sin\phi \\ -qsin\phi(B_{\mathrm{w}}v_\parallel + E_{\mathrm{w}}) \\ 0 \\ 0 \end{pmatrix}$$

,

$$\mathbf{F}_a = \begin{pmatrix} -\frac{p_\perp^2}{2\gamma\omega_{\mathrm{c}}m}\frac{\partial\omega_{\mathrm{c}}}{\partial z} \\ \frac{p_\perp p_\parallel}{2\gamma\omega_{\mathrm{c}}m}\frac{\partial\omega_{\mathrm{c}}}{\partial z} \\ k(v_{\mathrm{res}} - v_\parallel) \\ v_\parallel \end{pmatrix}$$

,

Additionally, the state vector can be written as $\mathbf{p} = \mathbf{p}_a + \Delta\mathbf{p}$, where $\mathbf{p}_a$ is the adiabatic motion of the particle state (when no wave is present), and $\Delta\mathbf{p}$ is the wave induced perturbation to the particle state. So far, the only approximation has been neglecting the additional wave force term

on the phase variation which is very small for magnetospheric parameters. The linearization step is introduced by expanding the forces in a power series around adiabatic motion.

$$\frac{d\mathbf{p}_a}{dt} + \frac{d\Delta\mathbf{p}}{dt} = \mathbf{F}_w(\mathbf{p}_a) + \mathbf{F}_a(\mathbf{p}_a) + \frac{\partial \mathbf{F}_w}{\partial \mathbf{p}_a}(\Delta\mathbf{p}) + \frac{\partial \mathbf{F}_a}{\partial \mathbf{p}_a}(\Delta\mathbf{p}) + O(\Delta p^2) \tag{B.2}$$

where $\dfrac{\partial \mathbf{F}}{\partial \mathbf{p}_a}$ is the 4 x 4 Jacobian matrix evaluated at $\mathbf{p}_a$. Linear scattering theory involves only taking the lowest order terms in $\Delta\mathbf{p}$ which involves only the zero order terms in this case. Additionally, $\dfrac{d\mathbf{p}_a}{dt} = \mathbf{F}_a$ by definition. The perturbation due to linear theory is then given by:

$$\frac{d\Delta\mathbf{p}}{dt} = \mathbf{F}_w(\mathbf{p}_a) \tag{B.3}$$

In component form, linear theory is given by

$$\frac{d\Delta p_\parallel}{dt} = qB_w v_{\perp_a} \sin\phi_a \tag{B.4}$$

$$\frac{d\Delta p_\perp}{dt} = -q(B_w v_{\parallel_a} + E_w)\sin\phi_a \tag{B.5}$$

All terms with the subscript 'a' correspond to adiabatic motion. For the case where a constant amplitude monochromatic wave is filling the entire simulation space (CW signal), the linearized equations of motion can be parameterized by position instead of time. In this case, linear theory is given by:

$$\frac{d\Delta p_\parallel}{dz} = \frac{qB_w v_{\perp_a} \sin\phi_a}{v_{\parallel_a}} \tag{B.6}$$

$$\frac{d\Delta p_\perp}{dz} = \frac{-qB_w(v_{\parallel_a} + v_p)\sin\phi_a}{v_{\parallel_a}} \tag{B.7}$$

These equations can be integrated to obtain $\Delta p_\perp$ and $\Delta p_\parallel$ as a function of position along the field line. These can be obtained numerically or in some cases analytically [48]. However, in the spirit of the VL model, the scattering can be calculated for one pass through the interaction region. For 'final' coordinates at the exit $(+z_L)$ of the interaction region, the 'initial' perturbations at the entrance $(-z_L)$ are given by

$$\Delta p_\parallel(-z_L) = \Delta p_\parallel(z_L) - \int_{-z_L}^{z_L} \frac{qB_w v_{\perp_a} \sin\phi_a}{v_{\parallel_a}} dz \tag{B.8}$$

$$\Delta p_\perp(-z_L) = \Delta p_\perp(z_L) - \int_{-z_L}^{z_L} \frac{-qB_w(v_{\parallel_a} + v_p)\sin\phi_a}{v_{\parallel_a}} dz \tag{B.9}$$

To specify the boundary conditions, we choose $\mathbf{p}(z_L) = \mathbf{p}_a(z_L) + \Delta\mathbf{p}(z_L) = \mathbf{p}_a(z_L)$ so that $\Delta\mathbf{p} = 0$. Note this is not an approximation, since there are two free parameters $(\mathbf{p}_a(z_L)$ and $\Delta\mathbf{p}(z_L))$ it is simply a convenient choice that states that perturbations are chosen relative to the

final particle coordinates. Nonzero values of $\Delta\mathbf{p}(z_L)$ will be reflected as a different value of $\mathbf{p}_a(z_L)$. Therefore, the scattering of one pass through the interaction region predicted by linear theory for a constant amplitude monochromatic wave is given by:

$$\Delta p_\parallel(-z_L) = -B_{\mathrm{w}} \int_{-z_L}^{z_L} \frac{q v_{\perp_a} \sin\phi_a}{v_{\parallel_a}} dz \tag{B.10}$$

$$\Delta p_\perp(-z_L) = B_{\mathrm{w}} \int_{-z_L}^{z_L} \frac{q(v_{\parallel_a} + v_p)\sin\phi_a}{v_{\parallel_a}} dz \tag{B.11}$$

Next, using Liouville's theorem, the distribution function at the exit can be computed in terms of the initial distribution function at the entrance,

$$f(p_\parallel(z_L), p_\perp(z_L), \phi(z_L), z_L) = f_{-z_L}(p_\parallel(-z_L), p_\perp(-z_L)) \tag{B.12}$$

Here, $\mathbf{p}(-z_L) = \mathbf{p}_a(-z_L) + \Delta\mathbf{p}(-z_L)$. However, for a model that is symmetric around the geomagnetic equator (as used in this study), $\mathbf{p}_a(-z_L) = \mathbf{p}_a(z_L)$. And as stated, earlier, the boundary conditions enforce $\mathbf{p}_a(z_L) = \mathbf{p}(z_L)$. Therefore, Equation (B.12) can be rewritten as

$$f(p_\parallel(z_L), p_\perp(z_L), \phi(z_L), z_L) = f_{-z_L}(p_\parallel(z_L) + \Delta p_\parallel(-z_L), p_\perp(z_L) + \Delta p_\perp(-z_L)) \tag{B.13}$$

Dropping all the (z_L) terms (since it is implied) and explicitly including the perturbations gives:

$$f(p_\parallel, p_\perp, \phi, z_L) = f_0(p_\parallel - B_{\mathrm{w}} \int_{-z_L}^{z_L} \frac{q v_{\perp_a} \sin\phi_a}{v_{\parallel_a}} dz, p_\perp + B_{\mathrm{w}} \int_{-z_L}^{z_L} \frac{q(v_{\parallel_a} + v_p)\sin\phi_a}{v_{\parallel_a}} dz) \tag{B.14}$$

The subscript '$-z_L$' has been replaced by the subscript '0' to indicate an initially unperturbed distribution. Once the distribution is computed, the precipitated flux can then be calculated by integrating over phase-space as shown in Equations $(3.5)-(3.6)$.

...

Bibliography

[1] B. Abel and R. M. Thorne. Electron scattering loss in earth's inner magnetosphere 1. dominant physical processes. *Journal of Geophysical Research*, 103:2385–2396, February 1998.

[2] J. M. Albert. Quasi-linear pitch angle diffusion coefficients: Retaining high harmonics. *Journal of Geophysical Research: Space Physics*, 99(A12):23741–23745, 1994.

[3] J. M. Albert. Analysis of quasi-linear diffusion coefficients. *Journal of Geophysical Research: Space Physics*, 104(A2):2429–2441, 1999.

[4] J. M. Albert. Comparison of pitch angle diffusion by turbulent and monochromatic whistler waves. *Journal of Geophysical Research: Space Physics*, 106(A5):8477–8482, 2001.

[5] J. M. Albert. Nonlinear interaction of outer zone electrons with vlf waves. *Geophysical research letters*, 29(8):1275, 2002.

[6] J. M. Albert. Evaluation of quasi-linear diffusion coefficients for emic waves in a multispecies plasma. *Journal of Geophysical Research*, 108, June 2003.

[7] J. M. Albert, X. Tao, and J. Bortnik. Aspects of nonlinear wave-particle interactions. *Geophysical Monograph Series*, 199:255–264, 2012.

[8] J. J. Angerami. Whistler duct properties deduced from vlf observations made with the ogo 3 satellite near the magnetic equator. *Journal of Geophysical Research*, 75(31):6115–6135, 1970.

[9] T. F. Bell. The nonlinear gyroresonance interaction between energetic electrons and coherent vlf waves propagating at an arbitrary angle with respect to the earth's magnetic field. *Journal of Geophysical Research: Space Physics*, 89(A2):905–918, 1984.

[10] T. F. Bell and O. Buneman. Plasma instability in the whistler mode caused by a gyrating electron stream. *Phys. Rev.*, 133:A1300–A1302, Mar 1964.

[11] J. Bortnik, R. M. Thorne, and U. S. Inan. Nonlinear interaction of energetic electrons with large amplitude chorus. *Geophysical Research Letters*, 35:21102, November 2008.

[12] W. J. Burtis and R. A. Helliwell. Magnetospheric chorus: Occurrence patterns and normalized frequency. *Planetary and Space Science*, 24:1007–1007, November 1976.

[13] R. K. Burton and R. E. Holzer. The Origin and Propagation of Chorus in the Outer Magneto-sphere. *Journal of Geophysical Research*, 79:1014–1023, 1974.

[14] C. R. Carlson, R. A. Helliwell, and U. S. Inan. Space-time evolution of whistler mode wave growth in the magnetosphere. *Journal of Geophysical Research: Space Physics*, 95(A9):15073–15089, 1990.

[15] D. L. Carpenter. Whistler evidence of a 'knee' in the magnetospheric ionization density profile. *Journal of Geophysical Research*, 68(6):1675–1682, 1963.

[16] D. L. Carpenter and R. R. Anderson. An ISEE/Whistler model of equatorial electron density in the magnetosphere. *Journal of Geophysical Research*, 97:1097–1108, February 1992.

[17] D. L. Carpenter and R. R. Anderson. Whistler model of equatorial electron density in the magnetosphere. *Journal of Geophysical Research: Space Physics*, 97(A2):1097–1108, 1992.

[18] D. L. Carpenter and Z. T. Bao. Occurrence properties of ducted whistler-mode signals from the new vlf transmitter at siple station, antarctica. *Journal of Geophysical Research: Space Physics*, 88(A9):7051–7057, 1983.

[19] D. L. Carpenter and R. L. Smith. Whistler measurements of electron density in the magneto-sphere. *Reviews of Geophysics*, 2(3):415–441, 1964.

[20] H. C. Chang, U. S. Inan, and T. F. Bell. Energetic electron precipitation due to gyroresonant interactions in the magnetosphere involving coherent VLF waves with slowly varying frequency. *Journal of Geophysical Research*, 88:7037–7050, sep 1983.

[21] N. Crouseilles, M. Mehrenberger, and E. Sonnendrücker. Conservative semi-lagrangian schemes for vlasov equations. *Journal of Computational Physics*, 229(6):1927–1953, 2010.

[22] K. B. Dysthe. Some studies of triggered whistler emissions. *Journal of Geophysical Research*, 76(28):6915–6931, 1971.

[23] F. Filbet and E. Sonnendrücker. Comparison of eulerian vlasov solvers. *Computer Physics Communications*, 150(3):247–266, 2003.

[24] F. R. Foust. *Discontinuous Galerkin Modeling of Wave Propagation, Scattering, and Nonlinear Growth in Inhomogeneous Plasmas*. PhD thesis, Stanford University, 08/2012 2012.

[25] N. Furuya, Y. Omura, and D. Summers. Relativistic turning acceleration of radiation belt electrons by whistler mode chorus. *Journal of Geophysical Research: Space Physics*, 113(A4), 2008.

[26] E. S. Gemelos. *Global Assessment of Precipitation of Radiation Belt Electrons by Electromagnetic Waves from Lightning.* PhD thesis, Stanford University, 07/2011 2011.

[27] R. Gendrin. General relationships between wave amplification and particle diffusion in a magnetoplasma. *Reviews of Geophysics*, 19(1):171–184, 1981.

[28] A. R. Gibby. *Saturation Effects in VLF Triggered Emissions.* PhD thesis, Stanford University, 05/2008 2008.

[29] A. R. Gibby, U. S. Inan, and T. F. Bell. Saturation effects in the vlf-triggered emission process. *Journal of Geophysical Research: Space Physics*, 113(A11), 2008.

[30] S. A. Glauert and R. B. Horne. Calculation of pitch angle and energy diffusion coefficients with the padie code. *Journal of Geophysical Research: Space Physics (1978–2012)*, 110(A4), 2005.

[31] M. Gołkowski, M. B. Cohen, D. L. Carpenter, and U. S. Inan. On the occurrence of ground observations of elf/vlf magnetospheric amplification induced by the haarp facility. *Journal of Geophysical Research: Space Physics (1978–2012)*, 116(A4), 2011.

[32] M. Gołkowski, U. S. Inan, M. B. Cohen, and A. R. Gibby. Amplitude and phase of nonlinear magnetospheric wave growth excited by the haarp hf heater. *Journal of Geophysical Research: Space Physics*, 115(A2), 2010.

[33] M. Gołkowski, U. S. Inan, A. R. Gibby, and M. B. Cohen. Magnetospheric amplification and emission triggering by elf/vlf waves injected by the 3.6 mw haarp ionospheric heater. *Journal of Geophysical Research: Space Physics*, 113(A10), 2008.

[34] D. A. Gurnett and A. Bhattacharjee. *Introduction to plasma physics: with space and laboratory applications.* Cambridge university press, 2005.

[35] N. Haque, U. S. Inan, T. F. Bell, J. S. Pickett, J. G. Trotignon, and G. Facskó. Cluster observations of whistler mode ducts and banded chorus. *Geophysical Research Letters*, 38(18), 2011.

[36] V. Harid, M. Gołkowski, T. Bell, and U. S. Inan. Theoretical and numerical analysis of radiation belt electron precipitation by coherent whistler mode waves. *Journal of Geophysical Research: Space Physics*, 119(6):4370–4388, 2014.

[37] R. A. Helliwell. A theory of discrete vlf emissions from the magnetosphere. *Journal of Geophysical Research*, 72(19):4773–4790, 1967.

[38] R. A. Helliwell. Controlled vlf wave injection experiments in the magnetosphere. *Space Science Reviews*, 15(6):781–802, 1974.

[39] R. A. Helliwell. Controlled stimulation of vlf emissions from siple station, antarctica. *Radio science*, 18(6):801–814, 1983.

[40] R. A. Helliwell. Vlf wave stimulation experiments in the magnetosphere from siple station, antarctica. *Reviews of Geophysics*, 26(3):551–578, 1988.

[41] R. A. Helliwell and T. L. Crystal. A feedback model of cyclotron interaction between whistler-mode waves and energetic electrons in the magnetosphere. *Journal of Geophysical Research*, 78(31):7357–7371, 1973.

[42] R. A. Helliwell and J. P. Katsufrakis. Vlf wave injection into the magnetosphere from siple station, antarctica. *Journal of Geophysical Research*, 79(16):2511–2518, 1974.

[43] M. Hikishima and Y. Omura. Particle simulations of whistler-mode rising-tone emissions triggered by waves with different amplitudes. *Journal of Geophysical Research: Space Physics (1978–2012)*, 117(A4), 2012.

[44] M. Hikishima, Y. Omura, and D. Summers. Self-consistent particle simulation of whistler mode triggered emissions. *Journal of Geophysical Research: Space Physics*, 115(A12), 2010.

[45] M. Hikishima, S. Yagitani, Y. Omura, and I. Nagano. Full particle simulation of whistler-mode rising chorus emissions in the magnetosphere. *Journal of Geophysical Research: Space Physics (1978–2012)*, 114(A1), 2009.

[46] R. B. Horne, S. A. Glauert, and R. M. Thorne. Resonant diffusion of radiation belt electrons by whistler-mode chorus. *Geophysical Research Letters*, 30(9):090000–1, May 2003.

[47] U. S. Inan. *Non-linear Gyroresonant Interactions of Energetic Particles and Coherent VLF Waves in the Magnetosphere*. PhD thesis, Stanford University, 08/1977 1977.

[48] U. S. Inan. Gyroresonant pitch angle scattering by coherent and incoherent whistler mode waves in the magnetosphere. *Journal of Geophysical Research: Space Physics*, 92(A1):127–142, 1987.

[49] U. S. Inan, T. F. Bell, and H. C. Chang. Particle precipitation induced by short-duration vlf waves in themagnetosphere. *Journal of Geophysical Research*, 87:6243–6264, aug 1982.

[50] U. S. Inan, T. F. Bell, and R. A. Helliwell. Nonlinear pitch angle scattering of energetic electrons by coherent vlf waves in the magnetosphere. *Journal of Geophysical Research: Space Physics*, 83(A7):3235–3253, 1978.

[51] U. S Inan and M. Gołkowski. *Principles of plasma physics for engineers and scientists*. Cambridge University Press, 2010.

[52] U. S. Inan, N. G. Lehtinen, R. C. Moore, K. Hurley, S. Boggs, D. M. Smith, and G. J. Fishman. Massive disturbance of the daytime lower ionosphere by the giant g-ray flare from magnetar SGR 1806–20. *Geophysical Research Letters*, 34:L08103, 2007.

[53] Y. Katoh and Y. Omura. A study of generation mechanism of vlf triggered emission by self-consistent particle code. *Journal of Geophysical Research: Space Physics*, 111(A12), 2006.

[54] Yuto Katoh and Yoshiharu Omura. Computer simulation of chorus wave generation in the earth's inner magnetosphere. *Geophysical Research Letters*, 34(3), 2007.

[55] C. F. Kennel and F. Engelmann. Velocity space diffusion from weak plasma turbulence in a magnetic field. *Physics of Fluids (1958-1988)*, 9(12):2377–2388, 1966.

[56] C. F. Kennel and H. E. Petschek. Limit on stably trapped particle fluxes. *Journal of Geophysical Research*, 71:1–28, 1966.

[57] I. Kimura. Effects of ions on whistler mode ray tracing. *Radio Sci.*, 1(3):269–283, 1966.

[58] D. S. Lauben, U. S. Inan, and T. F. Bell. Precipitation of radiation belt electrons induced by obliquely propagating lightning-generated whistlers. *Journal of Geophysical Research: Space Physics (1978–2012)*, 106(A12):29745–29770, 2001.

[59] J. D. Li, V. Harid, M. Spasojevic, M. Gołkowski, and U. S. Inan. Preferential amplification of rising versus falling frequency whistler mode signals. *Geophysical Research Letters*, 2015.

[60] J. D. Li, M. Spasojevic, V. Harid, M. B. Cohen, M. Gołkowski, and U. Inan. Analysis of magnetospheric elf/vlf wave amplification from the siple transmitter experiment. *Journal of Geophysical Research: Space Physics*, 119:1837 – 1850, 03/2014 2014.

[61] W. Li, J. Bortnik, R. M. Thorne, and V. Angelopoulos. Global distribution of wave amplitudes and wave normal angles of chorus waves using themis wave observations. *Journal of Geophysical Research: Space Physics (1978–2012)*, 116(A12), 2011.

[62] K. R. Lorentzen, J. B. Blake, U. S. Inan, and J. Bortnik. Observations of relativistic electron microbursts in association with VLF chorus. *Journal of Geophysical Research*, 106:6017–6028, April 2001.

[63] L. R. Lyons. Pitch angle and energy diffusion coefficients from resonant interactions with ion-cyclotron and whistler waves. *Journal of Plasma Physics*, 12:417–432, 12 1974.

[64] L. R. Lyons and R. M. Thorne. Equilibrium Structure of Radiation Belt Electrons. *J. Geophys. Res.*, 78:2142–2149, 1973.

[65] Lawrence R. Lyons, Richard Mansergh Thorne, and Charles F. Kennel. Pitch-angle diffusion of radiation belt electrons within the plasmasphere. *Journal of Geophysical Research*, 77(19):3455–3474, 1972.

[66] H. Matsumoto and Y. Omura. Cluster and channel effect phase bunchings by whistler waves in the nonuniform geomagnetic field. *Journal of Geophysical Research: Space Physics*, 86(A2):779–791, 1981.

[67] T. Nakamura and T. Yabe. Cubic interpolated propagation scheme for solving the hyper-dimensional vlasov—poisson equation in phase space. *Computer Physics Communications*, 120(2):122–154, 1999.

[68] D. Nunn. A self-consistent theory of triggered VLF emissions. *Planetary and Space Science*, 22:349–378, March 1974.

[69] D. Nunn. The numerical simulation of {VLF} nonlinear wave-particle interactions in collision-free plasmas using the vlasov hybrid simulation technique. *Computer Physics Communications*, 60(1):1 – 25, 1990.

[70] D. Nunn. A novel technique for the numerical simulation of hot collision-free plasma; vlasov hybrid simulation. *Journal of Computational Physics*, 108(1):180 – 196, 1993.

[71] D. Nunn, A. Demekhov, V. Trakhtengerts, and M. J. Rycroft. Vlf emission triggering by a highly anisotropic energetic electron plasma. In *Annales Geophysicae*, volume 21, pages 481–492. Copernicus GmbH, 2003.

[72] D. Nunn and Y. Omura. The theory and numerical modelling of non linear wave particle interactions in oblique whistlers. In *General Assembly and Scientific Symposium, 2011 XXXth URSI*, pages 1–1, 2011.

[73] D. Nunn and Y. Omura. A computational and theoretical analysis of falling frequency vlf emissions. *Journal of Geophysical Research: Space Physics*, 117(A8), 2012.

[74] D. Nunn, Y. Omura, H. Matsumoto, I. Nagano, and S. Yagitani. The numerical simulation of vlf chorus and discrete emissions observed on the geotail satellite using a vlasov code. *Journal of Geophysical Research: Space Physics*, 102(A12):27083–27097, 1997.

[75] D. Nunn, M. Rycroft, and V. Trakhtengerts. A parametric study of the numerical simulations of triggered vlf emissions. In *Annales Geophysicae*, volume 23, pages 3655–3666. Copernicus GmbH, 2005.

[76] D. Nunn and A. J. Smith. Numerical simulation of whistler-triggered vlf emissions observed in antarctica. *Journal of Geophysical Research: Space Physics*, 101(A3):5261–5277, 1996.

[77] Y. Omura, Y. Katoh, and D. Summers. Theory and simulation of the generation of whistler-mode chorus. *Journal of Geophysical Research: Space Physics*, 113(A4), 2008.

[78] Y. Omura, H. Matsumoto, D. Nunn, and M. J. Rycroft. A review of observational, theoretical and numerical studies of VLF triggered emissions. *Journal of Atmospheric and Terrestrial Physics*, 53:351–368, May 1991.

[79] Y. Omura and D. Nunn. Triggering process of whistler mode chorus emissions in the magnetosphere. *Journal of Geophysical Research: Space Physics*, 116(A5), 2011.

[80] C. G. Park. Generation of whistler-mode sidebands in the magnetosphere. *Journal of Geophysical Research: Space Physics*, 86(A4):2286–2294, 1981.

[81] A. Roux and R. Pellat. A theory of triggered emissions. *Journal of Geophysical Research: Space Physics*, 83(A4):1433–1441, 1978.

[82] S. S. Sazhin and M. Hayakawa. Magnetospheric chorus emissions: A review. *Planetary and Space Science*, 40(5):681–697, 1992.

[83] R. S. Selesnick, J. B. Blake, and R. A. Mewaldt. Atmospheric losses of radiation belt electrons. *Journal of Geophysical Research: Space Physics*, 108:1468, December 2003.

[84] Y. Y. Shprits, R. M. Thorne, R. B. Horne, and D. Summers. Bounce-averaged diffusion coefficients for field-aligned chorus waves. *Journal of Geophysical Research: Space Physics*, 111(A10), 2006.

[85] E. Sonnendrücker, J. Roche, P. Bertrand, and A. Ghizzo. The semi-lagrangian method for the numerical resolution of the vlasov equation. *Journal of computational physics*, 149(2):201–220, 1999.

[86] T. W. Speiser. Particle trajectories in a model current sheet, based on the open model of the magnetosphere, with applications to auroral particles. *Journal of Geophysical Research*, 70(7):1717–1728, 1965.

[87] J. Steinacker and J. A. Miller. Stochastic gyroresonant electron acceleration in a low-beta plasma. i-interaction with parallel transverse cold plasma waves. *The Astrophysical Journal*, 393:764–781, 1992.

[88] T. H. Stix. The theory of plasma waves. *The Theory of Plasma Waves, New York: McGraw-Hill, 1962*, 1, 1962.

[89] R. N. Sudan and E. Ott. Theory of triggered vlf emissions. *Journal of Geophysical Research*, 76(19):4463–4476, 1971.

[90] D. Summers. Quasi-linear diffusion coefficients for field-aligned electromagnetic waves with applications to the magnetosphere. *Journal of Geophysical Research: Space Physics*, 110(A8), 2005.

[91] X. Tao, J. Bortnik, J. M. Albert, and R. M. Thorne. Comparison of bounce-averaged quasi-linear diffusion coefficients for parallel propagating whistler mode waves with test particle simulations. *Journal of Geophysical Research: Space Physics*, 117(A10), 2012.

[92] X. Tao, J. Bortnik, J. M. Albert, R. M. Thorne, and W. Li. The importance of amplitude modulation in nonlinear interactions between electrons and large amplitude whistler waves. *Journal of Atmospheric and Solar-Terrestrial Physics*, 99(0):67 – 72, 2013. Dynamics of the Complex Geospace System.

[93] R. M. Thorne, E. J. Smith, K. J. Fiske, and S. R. Church. Intensity Variation of Elf Hiss and Chorus during Isolated Substorms. *Geophysical Research Letters*, 1:193–196, 1974.

[94] F. Valentini, P. Veltri, and A. Mangeney. A numerical scheme for the integration of the vlasov–poisson system of equations, in the magnetized case. *Journal of Computational Physics*, 210(2):730–751, 2005.

[95] J. L. Vomvoridis and J. Denavit. Test particle correlation by a whistler wave in a nonuniform magnetic field. *Physics of Fluids (1958-1988)*, 22(2):367–377, 1979.

[96] M. Walt. *Introduction to Geomagnetically Trapped Radiation*, volume 1. Cambridge University Press, 2005.